UNIVERSITY OF CALIFORNIA

Santa Barbara

Theoretical and Experimental Studies of III-Nitride Devices

A dissertation submitted in partial satisfaction of the

Requirements for the degree Doctor of Philosophy in Materials

By

Kai Shek (Clayton) Qwah

Committee in charge:

Professor James S. Speck, Chair

Professor Claude Weisbuch

Professor Steven P. Denbaars

Professor Yuh-Renn Wu

September 2022

The dissertation of Kai Shek Qwah is approved.

_____

Yuh-Renn Wu

_____

Claude Weisbuch

_____

Steven P. DenBaars

_____

James S. Speck, Committee Chair

September 2022

Acknowledgements

I would first like to thank the members my advisor, Professor James S. Speck, for his guidance over the course of my PhD and giving me the opportunity to pursue research in my field of interest. I would also like to thank Professor Claude Weisbuch and Professor Steven P. Denbaars for their input and advise during my time here. I would like to thank Professor Yuh-Renn Wu for his guidance in the field of device simulation as well as allowing the usage of his servers and his 3-D Drift-Diffusion Charge Control (3D-DDCC) solver.

Secondly, I would like to thank Kurt Olsson and John English, for all their guidance and their help in maintaining the Nitride 930 MBE machine. Apart from that, I would like to thank all the staff I have worked with over the years at UCSB, including Dr Tom Mates, Dr. Mark Cornish, Dr. Claire Chisholm, Dr Aidan Taylor and all of the staff at UCSB Nanofabrication facility.

I would also like to thank my sponsors from CREST for funding my PhD here at UCSB. I would like to thank Jaffri Ibrahim for his leadership of the company and making my PhD scholarship possible. I would like to thank Hoo Kooi Lim for helping us transition from Malaysia to the US and being our spokesperson to our Malaysian sponsors.

I would like to thank the postdocs and PhD students I have worked with over the years: Dr. Dr. Micha Fireman, Dr. Jianfeng Wang, Dr. Christian Robertson, Dr. Kelsey Jorgensen, Dr. Richard Cramer, Dr. Yuewei Zhang, Dr. Morteza Monavarian, Dr. Christian Wurm, Zachary Biegler, Ashley Wissel, Tsung-Yin Tsai and Dr. Esmat Farzana. They have all been a vital part of my success here at UCSB and teaching me how to conduct research in a proper systematic manner.

Thank you to all the people in SSLEEC for all the useful intellectual discussions they have been providing me. I would like to thank all the friends I have made throughout the years here at UCSB for distracting me from the stresses of my research and for the great company they have given me over the years. Special thanks to Chow Yi Chao and Wan Ying Ho, my fellow Malaysian PhD students. It is great to have comrades of similar backgrounds and culture to be part of a challenging journey.

Finally, I would like to thank the people I love. I would like to thank my girlfriend Rachel Wu, who has been a wonderful part of my journey here and who has been a great pillar of support. I would like to thank my sibling, Aaron and Jasmine, who have supported me over the years. I would like to thank my dad, Qwah Say Hoh and my mother, Lim Ruby, for not only birthing me and providing me everything I needed over the course of my life, but also instilling my passion for science and cultivating my curiosity.

Vita of Kai Shek (Clayton) Qwah

August 2022

Education

University of California, Santa Barbara (2016- 2022) PhD in Materials Engineering

- Currently attached to the Solid-State Lighting and Energy Electronics Center (SSLEEC), spearheaded by Professor Shuji Nakamura (2014 Physics Nobel Laureate), Professor Steven P. Denbaars and Professor James S. Speck.

Imperial College London (2011-2015) MSci in Physics with Theoretical Physics

- Grade: Second Class (Upper Division)
- Modules Covered : Computational Physics, Foundation of Quantum Mechanics, Complexity and Networks, Solid-State Physics, Atomic and Molecular Physics, Optical Communication Physics, Quantum Field Theory, General Relativity

Experiences

Secretary of the Board of Directors at Santa Barbara Student Housing Cooperative (October 2016 - June 2017)

- One of the board of directors at the Santa Barbara Housing Co-operative with responsibilities in the following:
  - Reviewing the budget and financial statements
  - Conducting member reviews
  - Deciding on co-op wide policy changes
- Responsibilities as Secretary:
  - Keep on file in the Corporation office copies of the Articles of Incorporation and Bylaws
  - Provide communications on behalf of the Board
  - Give notice on annual, regular and special meetings of the membership and the Board
  - Serve on the Steering Committee of the Santa Barbara Student Housing Cooperative
  - Signing off official Documents

Software Architect at Wooppy Sdn. Bhd. (January 2016 – July 2016)

- Wooppy was a startup with the goal of designing an artificially intelligent virtual shopping assistant, aiding in shopping purchase decisions by giving the best recommendations tailored to specific individuals.
- Part of the founding team in charge of researching on and constructing a natural language processor and knowledge base for the purpose of developing the chatbot for the virtual assistant.
- Contributed to the development of the business model of the company as well as identifying key demographics.

Publications

- **K. S. Qwah**, M. Monavarian, G. Lheureux, J. Wang, Y.-R. Wu, and J. S. Speck, *Theoretical and Experimental Investigations of Vertical Hole Transport through Unipolar AlGaN Structures: Impacts of Random Alloy Disorder*, Appl. Phys. Lett. **117**, 022107 (2020).
- **K. S. Qwah**, M. Monavarian, W. Y. Ho, Y.-R. Wu, and J. S. Speck, *Vertical Hole Transport through Unipolar InGaN Quantum Wells and Double Heterostructures*, Phys. Rev. Materials **6**, 044602 (2022).
- **K. S. Qwah**, C. A. Robertson, Y.-R. Wu, and J. S. Speck, *Modeling Dislocation-Related Reverse Bias Leakage in GaN p–n Diodes*, Semicond. Sci. Technol. **36**, 075001 (2021).
- **K. S. Qwah**, E. Farzana, A. Wissel, M. Monavarian, T. Mates, and J. S. Speck, *Indium as a Surfactant: Effects on Growth Morphology and Background Impurity in GaN Films Grown by Ammonia-Assisted Molecular Beam Epitaxy*, APL Materials **10**, 081107 (2022).
- C. A. Robertson, **K. S. Qwah**, Y.-R. Wu, and J. S. Speck, *Modeling Dislocation-Related Leakage Currents in GaN p-n Diodes*, Journal of Applied Physics **126**, 245705 (2019).
- M. Monavarian, J. Xu, M. N. Fireman, N. Nookala, F. Wu, B. Bonef, **K. S. Qwah**, E. C. Young, M. A. Belkin, and J. S. Speck, *Structural and Optical Properties of Nonpolar M- and a-Plane GaN/AlGaN Heterostructures for Narrow-Linewidth Mid-Infrared Intersubband Transitions*, Appl. Phys. Lett. **116**, 201103 (2020).
- E. Farzana, J. Wang, M. Monavarian, T. Itoh, **K. S. Qwah**, Z. J. Biegler, K. F. Jorgensen, and J. S. Speck, *Over 1 KV Vertical GaN-on-GaN p-n Diodes With Low On-Resistance Using Ammonia Molecular Beam Epitaxy*, IEEE Electron Device Letters **41**, 1806 (2020).
- J. Wang, K. F. Jorgensen, E. Farzana, **K. S. Qwah**, M. Monavarian, Z. J. Biegler, T. Mates, and J. S. Speck, *Impact of Growth Parameters on the Background Doping of GaN Films Grown by Ammonia and Plasma-Assisted Molecular Beam Epitaxy for High-Voltage Vertical Power Switches*, APL Materials **9**, 081118 (2021).
- P. Li, H. Li, Y. Yao, H. Zhang, C. Lynsky, **K. S. Qwah**, J. S. Speck, S. Nakamura, and S. P. DenBaars, *Demonstration of High Efficiency Cascaded Blue and Green Micro-Light-Emitting Diodes with Independent Junction Control*, Appl. Phys. Lett. **118**, 261104 (2021).
- P. Li, H. Li, Y. Yao, H. Zhang, C. Lynsky, **K. S. Qwah**, J. S. Speck, S. Nakamura, and S. P. DenBaars, *Fully Transparent Metal Organic Chemical Vapor Deposition-Grown Cascaded InGaN Micro-Light-Emitting Diodes with Independent Junction Control*, Opt. Express, OE **29**, 22001 (2021).
- C. Lynsky, G. Lheureux, B. Bonef, **K. S. Qwah**, R. C. White, S. P. DenBaars, S. Nakamura, Y.-R. Wu, C. Weisbuch, and J. S. Speck, *Improved Vertical Carrier Transport for Green III-Nitride LEDs Using InGaN Alloy Quantum Barriers*, Phys. Rev. Applied **17**, 054048 (2022).

Scholarships

CREST Scholarship for the GaN-on-GaN project

- One of three Malaysian PhD students to receive a full scholarship from CREST, a Malaysian-based company that collaborates with industry and academia in research, design and development activities to enable Malaysia to become a high income nation.

Awards

Outstanding Graduate Student Research Achievement Award

- Awarded by the Solid-State Lighting Energy and Electronics Center (SSLEEC) to students who have performed excellent and impactful research in the field of III-nitride materials

Abstract

Theoretical and Experimental Studies of III-Nitride Devices

by

Kai Shek (Clayton) Qwah

In the field of semiconductor devices, the III-nitride material system, which is mainly made up of Indium Nitride (InN), Gallium Nitride (GaN) and Aluminum Nitride (AlN), has seen a great deal of attention over the past decade. Despite the maturity of this field of research, the growth mechanics and physics that govern the behavior of these devices is still poorly understood.

For all the devices mentioned, there exist regions called heterojunctions, which can be defined as the interface between two materials of different band gaps. In the case of LEDs, these heterojunctions are typically at the interface of alloy regions, which are the Quantum Well (QWs) layer and the Electron-Blocking Layer (EBL). These regions have compositional fluctuations due to the random distribution of the atomic constituent in the alloy. This phenomenon, known as alloy disorder, has largely been insignificant in the studies of other III-V semiconductors. However, due to the higher effective mass and larger band gaps of the nitrides, disorder plays a significant role in understanding the carrier transport behavior within nitride devices.

My research involves examining each of these layers and studying the hole transport behavior within these two types of heterostructures to better understand their electrical behavior. However, typical studies use LEDs as test structures, which are bipolar devices and are subject to recombination mechanisms. By using unipolar heterostructures, we can focus solely on the carrier transport within these structures without recombination complicating the analysis of the system, making them ideal test vehicles for theoretical models. My study involves simulating a three-dimensional unipolar *p*-type heterostructure that incorporates the fluctuations of the alloy composition within the alloy region. This would normally require solving for the wavefunctions of the system via Schrödinger's equation. However, solving this equation in 3D is a computationally expensive task and could take months to obtain results. By using a mathematical theory called the Localization Landscape theory, we can simplify Schrödinger's equation and converge to a solution three orders of magnitude faster than current simulation techniques. This allows us to viably give LEDs the full 3-dimensional treatment and obtain band structure information as well as current-voltage characteristics. These simulations were then compared to experimental realizations of these structures, which were grown by ammonia-assisted molecular beam epitaxy (NH_3-MBE) and fabricated into devices for electrical measurements. The simulation results are verified by experiments using unipolar vertical hole transport structures enabled by n-to-p tunnel junctions (TJs) grown by ammonia molecular-beam epitaxy (NH3-MBE). The experimental results show that even a thin UID $Al_xGa_{1-x}N$ (x = 14%, 13 nm) introduces an asymmetric barrier to the hole transport; A nearly 100% increase in drop voltages induced by a thin UID AlGaN at 50 A/cm^2 in reverse direction is compared to only 25% corresponding increase in the forward direction. Furthermore, p-type doping of the AlGaN layer results in a drastic drop in the potential barrier to hole transport in

both directions. Following that, a similar study was conducted for InGaN double heteostructures and quantum wells. The results indicate that increasing the UID $In_{0.1}Ga_{0.9}N$ layer thickness from 15 nm to 30 nm increases the forward bias voltage drop (~2 V at 500 A/cm^2) more than the reverse bias voltage drop (~ 0.2 V at 500A/cm^2). For the QW structures, increasing the number of QWs from 1 to 3 increases the voltage penalty similarly in forward and reverse directions (~ 0.25 V per QW at 500 A/cm^2).

Since the demonstration of III-nitride based transistors and diodes, their progress has also been limited by different challenges, one of which includes the presence of extended defects such as high densities of threading dislocations in the material grown on lattice-mismatched foreign substrates, which results in the degradation of device performance. This is demonstrated for GaN *p-n* diodes, in which threading dislocations behave as leakage pathways under both forward and reverse biases. In addition to this, high-voltage power switches require thick drift regions (on the order of 10 μm) with low background doping levels (on the order of $10^{15} – 10^{16}$ cm^{-3}) to realize high blocking voltages. Hence, there is also a need for growth methods and optimized conditions to enhance the growth rate, maintaining the low background doping.

We conducted a study to investigate the effects of threading dislocation density on the transport properties of vertical GaN p-n junctions. Vertical GaN p-n diodes grown by NH_3-MBE have been shown to be severely affected by threading dislocation density in terms of leakage currents. To study the effect of threading dislocations, finite element simulations were conducted to compare GaN p-n diodes with and without a dislocation. At zero bias, the

depletion width and the maximum electric field were significantly reduced near the dislocation line. The reduction in the diffusion barrier for electrons and holes was asymmetric due to the asymmetric nature of the dislocation induced band bending related to the doping and trap parameters. This reduction in diffusion barrier facilitated the diffusion of electrons and holes in forward bias. Finally, this diffusion barrier reduction carrier resulted in an additional leakage mechanism via Shockley-Read-Hall non-radiative recombination mediated by a high np-product and trap state density near the intersection of the dislocation with the junction. In the reverse bias case, it was found that the defects coalesced by the dislocation strain field will mediate electron-hole pair generation by a trap-assisted tunneling mechanism occurring at a peak electric field in the junction near the dislocation. These electron-hole pairs are then swept away from the junction by the strong, reverse bias electric field thereby resulting in a reverse bias leakage current mediated by the dislocation trap states.

To improve the surface morphology in epitaxial growth, surfactants are commonly employed. For the case of group III nitrides, indium has been shown to be a highly effective surfactant. Typically, surfactants alter the surface morphology by modifying the surface energy and/or the adatom mobility. I investigated the effects of indium as a surfactant and other growth conditions on the surface morphology during NH3-MBE growth of unintentionally-doped (UID) GaN under fast growth rates (1 μm/hour). The surface morphology was characterized using atomic probe tomography and the impurity concentration within the UID GaN was obtained using secondary ion mass spectroscopy (SIMS). It was found that, through a series of optimizations, indium was able to improve the surface morphology during high flux growth. Moreover, it was also observed that indium suppresses the background Si impurity

concentration in the film. The improvements in the surface morphology while maintaining low background impurity levels for fast growth rates would provide a path toward high-quality thick drift regions growths with smooth morphologies for regrowth-free high-voltage vertical devices for power switching applications.

List of Figures and Tables

Table of Contents

Chapter 1 : III-Nitrides by MBE

1.1 III-Nitride Fundamentals

The III-Nitride material system have been the subject of much research interest over the past decade. This is because they have unique capabilities that make them very attractive for various device applications. These include their abilities to withstand large electrical breakdown voltages (on the order of $1.2 – 1.8 \times 10^6$ V cm^{-1}), making them ideal materials for high-frequency and high-power electronic device applications. Apart from that, by constructing alloys of the different nitride semiconductors, it is possible to tune the bandgap to span from the infrared, which corresponds to a bandgap of 0.65eV for InN, to the deep ultraviolet wavelengths of light, which corresponds to a bandgap of 6.0 eV for AlN. This large range of energies make them versatile for the optoelectronic applications such as LEDs and laser diodes. Moreover, the material has high thermal stability[1] as well as resistance to chemically corrosive conditions[2] and irradiation efects[3].

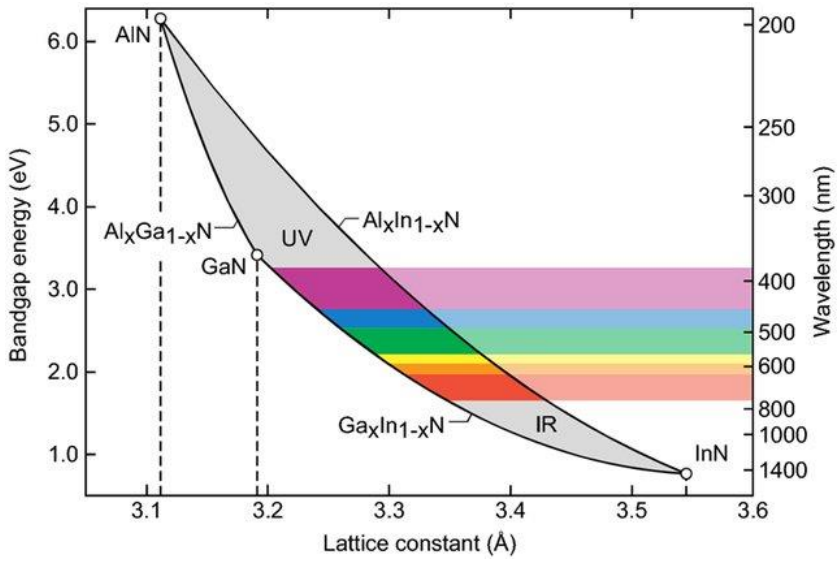

Figure 4. The bandgap energy (and corresponding wavelength) vs lattice constant for the different III-nitride compounds. [4]

The III-nitride material system also exhibits two main types of crystal structures: cubic zinc blende and hexagonal wurtzite, with the latter being the most thermodynamically stable crystal structure[5]. In wurtzite structures, the bonds along the c-axis are different in length when compared to the bonds perpendicular to the axis as shown in Figure 5.

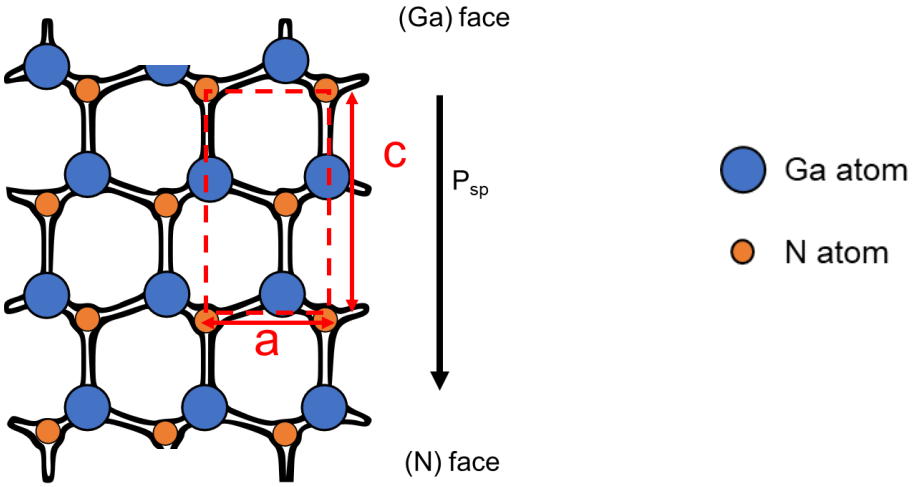

Figure 5 : Crystal structure of GaN with the unit cell denoted within the dashed line along with the direction of spontaneous polarization and the lattice.

Material	GaN	AlN	InN
c/a	1.626	1.602	1.611

Table 3: The ratio between the c parameter and a parameter for GaN, AlN, and InN

For an ideal hexagonal closed packed crystal with all nearest-neighbor bond lengths are equal, the ratio of the lattice parameters c_0 and a_0:

$$\frac{c_0}{a_0} = 1.63299$$

Any deviation from this ratio, coupled with the polar bond due to the large difference in electronegativities between group III elements and nitrogen, results in a net dipole oriented along

the [0001] direction. This in turn produces a bound sheet charge on the (0001) and $(000\bar{1})$ surface of the nitride crystal as well as at heterojunction interfaces. This is what is known as spontaneous polarization, P_{SP}.

Besides that, when crystals are subjected to compression or strain, the shifting of the crystal structure also results in the change in the c/a ratio, bringing it either further or closer to the ideal *c/a* ratio. This phenomenon, which is known as piezoelectric polarization, P_{PE}, also produces a surface charge at heterointerfaces as well as on the pure crystal surface. When evaluating polarization fields in nitrides, it is important to consider the changes to the ratio due to strain from the lattice constant mismatch with the underlying layer. Biaxial compressive stress causes a decrease in the in-plane lattice parameter, *a* and increases the vertical lattice parameter, *c*. This increases the *c/a*, bringing it closer to the ideal ratio. This results in a P_{PE} that opposes the spontaneous polarization, bringing the overall polarization in the crystal down. However, applying tensile stress to the film lowers the *c/a* ratio

In general, the total polarization, **P** is calculated via the equation:

$$-\rho = \nabla . \boldsymbol{P}$$

where $\nabla . \boldsymbol{P}$ is the divergence of the field **P** through a surface containing the bound charge density, ρ. However, if there is an interface between two materials of different polarizations, by taking a Gaussian pillbox integral at the interface, one obtains an interfacial polarization charge density. In the case of heterojunction, this sheet charge density, σ is then given as:

$$\sigma = P_{layer\ A} - P_{layer\ B}$$

$$P = P_{SP} + P_{PE}$$

In the case of P_{PE}, the relevant equation to calculate the field in nitrides is given as:

$$P_{PE} = 2\frac{a - a_0}{a_0}(e_{31} - e_{33}\frac{C_{13}}{C_{33}})$$

Where C_{13} and C_{31} are elastic constants, e_{31} and e_{33} are the piezoelectric coefficients, and a and a_0 are the lattice constants for the strained and relaxed crystals respectively. The magnitudes of each of these parameters are given in Table 4. The sense of polarization for each type of heterojunction interface is also given in Figure 6.

Material	P_{SP} (C/m^2)	e_{31} (C/m^2)	e_{33} (C/m^2)	C_{13} (GPa)	C_{33} (GPa)
GaN	-0.029	-0.49	0.73	103	405
InN	-0.032	-0.49	0.73	92	224
AlN	-0.081	-0.58	1.55	108	373

Table 4: Table of parameters used to calculate polarization in III-nitrides

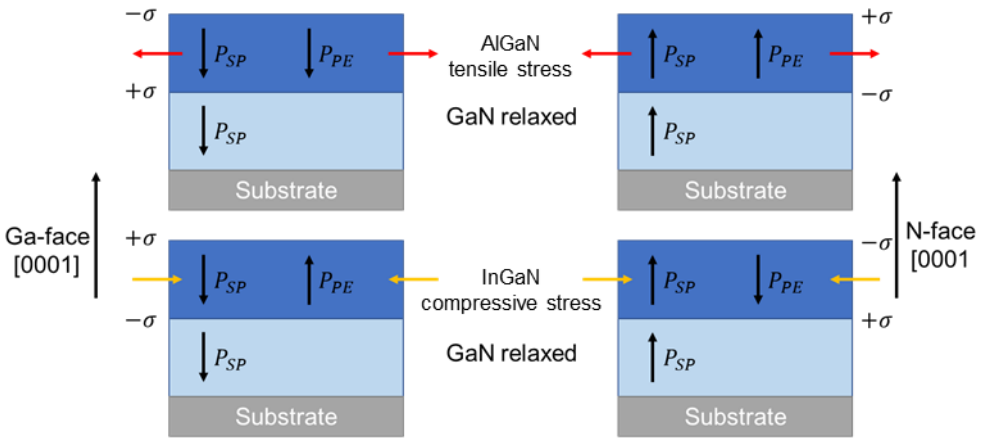

Figure 6 : Schematic outlining the sense of polarization for different nitride heterostructures.

This polarization field also happens to be dependent on the growth orientation of these structures. It is known that the polarization in the c-plane orientation has the largest magnitude whilst m-plane and a-plane, commonly referred to as nonpolar planes, exhibit no polarization.

Since most nitride devices are grown on c-plane substrates, it is important to study the effects of polarization, which can be significant.

1.2 Ammonia-Assisted (NH_3) Molecular Beam Epitaxy growth of III-Nitrides

Molecular Beam Epitaxy (MBE) is a method of crystal growth that has been widely used to grow high quality semiconductor crystals. The technique, initially developed for the growth of conventional III-V semiconductor structures, remains the ideal method for prototyping test structures for fundamental material studies due to the ability to produce sharp interfaces as well as low impurity concentrations. The technique involves the deposition of material in an ultra-high vacuum (UHV) environment using atomic fluxes of the constituent species as shown in Figure 7. For III-nitrides systems, the two methods of supplying the nitrogen include using nitrogen plasma or using ammonia, the latter being the method of choice for my studies. The group III element is provided through traditional dual filament effusion cells.

The samples are first cleaned through a standard acetone, methanol and isopropanol dip. Following that, they are loaded into refractory molybdenum blocks and then baked twice: once in the loading chamber at 120 ^{o}C for an hour and a half, and once in the buffer chamber at 400 °C for two hours. This is to remove moisture as well as organic compounds present on the sample. Finally, they are transferred into the main MBE chamber and onto a Continuous Azimuthal Rotation (CAR) holder. The samples are then heated using a resistive heater on the back of the CAR, with the temperature being controlled using a proportional–integral–derivative (PID) controller. This temperature control system is also present in the effusion cells that supply the elemental constituent atoms during crystal growth. To monitor the temperature of the sample throughout growth, a pyrometer was used. The emissivity of the samples are then calibrated against the backside metal

found on the back of the sample. The backside is coated with 5 nm of Ti followed by 500 nm of Pd and another 100 nm of Ti. Pd was chosen as it is very stable and inert to reactions with the ammonia in the system. However, Pd does not adhere very well to the backside, so a thin layer of Ti was used as an adhesion layer. Another problem with Pd is that it is highly reflective and required more power to heat up. Thus, a final layer of Ti was needed to help facilitate the transfer of heat to the substrate.

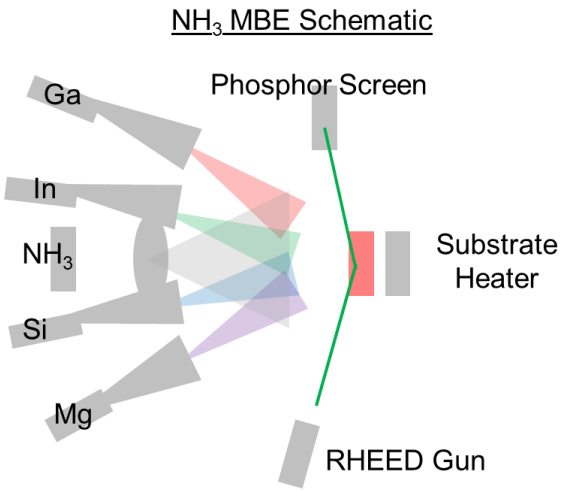

***Figure 7**: Schematic of MBE configuration.*

Due to the large presence of ammonia in the chamber, the film is grown in a N-rich environment, with the growth occuring through the pyrolysis of ammonia and reacting to the group III element through the following chemical equation:

$$Group\ III\ (s) + NH_3\ (g) \leftrightarrow\ III - N(s) + \frac{3}{2}H_2(g)$$

During growth, a balance needs to be struck by depositing enough material at sufficiently low temperatures to prevent desorption of reactants from the surface but high enough to ensure

sufficient kinetic mobility of the adatoms on the surface to properly incorporate into the crystal lattice, filling any kinks and vacancies.

One advantage of NH_3-MBE is the lack of metal decorated dislocation cores, which happens during plasma-assisted MBE (PAMBE) growth due to the optimal growth regime being metal-rich. These metal-rich defects act as current-leakage pathways, which are not ideal for electrical devices. Thus, NH_3-MBE is the preferred growth technique for vertical device epitaxial growth. However, due to the inefficient thermal cracking of ammonia[6], the lower limit on growth in the NH_3-MBE system is placed at approximately 550 °C

References

[1] H. Ishikawa, K. Yamamoto, T. Egawa, T. Soga, T. Jimbo, and M. Umeno, Journal of Crystal Growth **189–190**, 178 (1998).
[2] U. Kamachi Mudali, in *Materials Under Extreme Conditions*, edited by A.K. Tyagi and S. Banerjee (Elsevier, Amsterdam, 2017), pp. 91–128.
[3] Y.J. Yoon, J.S. Lee, J.K. Suk, I.M. Kang, J.H. Lee, E.J. Lee, and D.S. Kim, Micromachines **12**, 864 (2021).
[4] E.F. Schubert, *Light-Emitting Diodes* (Cambridge University Press, 2006).
[5] K.M. Kelchner, S.P. DenBaars, and J.S. Speck, in *Semiconductors and Semimetals*, edited by J.J. Coleman, A.C. Bryce, and C. Jagadish (Elsevier, 2012), pp. 149–182.
[6] M. Mesrine, N. Grandjean, and J. Massies , Appl. Phys. Lett. **72**, 350-352 (1998)

Chapter 2 : Vertical Transport through unipolar p-type Nitride Heterostructures

2.1 Vertical transport through p-type AlGaN Heterostructures

I. Introduction

III-nitrides have attracted a great deal of attention over the past few decades due to their applications in various areas within optoelectronics and power electronics[1,2]. AlGaN alloys are typically used in numerous III-nitride-based devices to serve as quantum barriers (QBs) to electrons and/or holes. In power electronics, AlGaN heterostructures have been the basis for many designs, including high-electron mobility transistors (HEMTs), resonant-tunneling diodes (RTDs)[3,4], hot-electron transistors[5,6] and current-aperture vertical electron transistors (CAVETs)[7,8]. In optoelectronics, AlGaN alloys have been used in visible light-emitting diodes (LEDs) as well as lasers[9] for structures such as electron-blocking layers (EBL), which are typically placed right behind the active region to mitigate the carrier overflow and to enhance the carrier confinement within quantum well (QW) active regions[10]. There has been a growing interest in using AlGaN system as the basis for ultraviolet LEDs (UV-LEDs)[11,12] and intersubband structures for mid-infrared (MIR) and terahertz applications[13,14]. Even more recently, the potentially high breakdown field of AlGaN has motivated its use as an ultrawide bandgap semiconductor for vertical power electronic devices. Hence, heterostructures related to the AlGaN material have been a central segment for many III-nitride-based applications.

Despite the maturity of the III-nitride field of research and the use of AlGaN and GaN/AlGaN heterostructures in various areas, the physics of vertical transport through AlGaN structures is still poorly understood. One possible reason is the presence of natural random alloy disorder, providing a percolated pathway within the barrier, thus affecting the carrier transport through the alloy layer. Due to the complex nature of alloy disorder, the regular Schrödinger -Poisson quantum mechanical

calculation requires an impractical time to solve for the eigenstates in alloy systems. Localization Landscape theory has recently been proposed to solve for random potentials, weak localization and Anderson localization[15,16], which has been applied to semiconductor-related problems, including carrier transport and recombination in LEDs[17,18]. This theory suggests a reduction in the computation time by nearly three orders of magnitude reduction for a random potential compared to a conventional Schrödinger -Poisson solver[17].

In the past, unipolar *n*-type AlGaN heterostructures have been proposed as standard test structures to experimentally investigate the electron transport in AlGaN alloy systems[19]. An isotype structure would eliminate the recombination process from analysis, which considerably simplifies the picture and helps in understanding the carrier transport mechanisms in the AlGaN structures. Nath *et. al.*[20] studied *n*-type GaN/AlGaN/GaN heterostructures grown by plasma-assisted molecular beam epitaxy (PAMBE). It was found that even a 30 nm-thick AlGaN layer with 37% composition of Al does not provide a barrier to the electron transport, and that the electrical current is unaffected by threading dislocation density and temperature[20]. Browne *et. al.*[19] conducted a similar study for structures grown by ammonia MBE (NH_3-MBE) and metalorganic chemical vapor deposition (MOCVD). The study showed that AlGaN fails to provide an effective barrier to electron transport, which is in contrary to the one-dimensional (1D) band diagram calculations, under different compositions and threading dislocation density. In addition, the percolative transport mechanism due to random alloy fluctuations within the AlGaN region is shown as the main cause of carrier leakage through the disordered AlGaN[19]. Nevertheless, the aforementioned studies were focused on electron transport mechanism and disregarding the transport mechanisms of holes, which is extremely important for optoelectronic and electronic

applications. The transport behaviors of electrons and holes are expected to be different due to the difference in their effective masses.

In this work, we theoretically and experimentally investigate hole transport through disordered AlGaN barrier in *p*-type unipolar GaN/AlGaN heterostructures. Both 1D and 3D drift-diffusion models based on Localization Landscape theory were considered to simulate the hole transport, with the latter incorporating random alloy fluctuations within the AlGaN layer. The vertical hole transport structures were then grown by NH_3-MBE using *n*-to-*p* tunnel junctions (TJs) to minimize the hole spreading resistance. The TJ structure is utilized in our transport structure design for a number of reasons. First, for a structure without a TJ, the high resistivity of *p*-GaN would hinder the current spreading in the structure, causing the current to pass through the sidewalls instead of the heterostructure (and also there would be a large voltage drop within the *p*-GaN base of the structure). In addition, the ion damage inflicted on the *p*-type GaN[21] damage the *p*-layer, causing N-vacancies (N_V) to form, which act as shallow donors[22]. Both theoretical and experimental results show that unintentionally doped (UID) AlGaN provides a barrier to hole transport in both reverse and forward directions, while the *p*-type doping of the AlGaN layer results in little to no barrier to hole transport in both directions.

II. Simulation Procedure

The band diagrams and current density-voltage (*J*-*V*) characteristics of the structures were simulated using a Poisson-Drift-Diffusion solver developed earlier incorporating the Localization Landscape theory[17]. The software uses the Gummel iteration method, a standard algorithm typically used to solve for the band diagrams and *J*-*V* characteristics[23]. Instead of solving the time-independent Schrodinger eigenvalue equation:

$$\widehat{H}\psi = E\psi \quad (1)$$

The Localization Landscape solver solves the landscape equation which is of the form:

$$\widehat{H}u = 1 \quad (2)$$

where $\widehat{H}$ is the Hamiltonian, ψ is the eigenfunction, E is the energy eigenvalue, and u is the landscape function. Figure 1(a) shows the flow chart for the Gummel method incorporating Localization Landscape theory. The landscape function can then be used to obtain an effective potential, dubbed the landscape potential, W, where $W = 1/u$. W as well as the landscape function are deeply connected to the Schrödinger equation, as the original eigenfunction ψ may be recovered using an auxiliary function, described in detail in ref. 24.

The simulation solves the Poisson, drift-diffusion equations, and Localization Landscape equations (as Eq(1)) self consistently. The quasi-Fermi levels in Eq(3) and (4) will be obtained by solving drift-diffusion equations. Our model uses the modified Boltzmann transport equation (which is Fickian and classical) to calculate the current for holes and electrons. Other anomalous diffusion phenomenon, such as non-Fickian diffusion will be explored in the future. Since W has similar barrier heights to those of the valence band edge for holes, the Localization Landscape method can accurately capture the barriers to the hole transport. More details of the Localization Landscape method and the boundary conditions can be found in the supplementary material.

Based on atom-probe tomography data measured on similar AlGaN structures[19], a random Al composition map with a desired average composition (~ 14%) (Figure 1(b)) was used as an input to the Poisson's equation. In contrast to the random composition map used for 3D simulations, a constant composition map with the same average composition (~ 14%) was used for 1D simulations. The conduction band (E_c) and valence band (E_v) energies (Figure 1 (c)) calculated by

solving the Poisson's equation were then fed into the landscape equation to obtain electron and hole carrier densities using the equations:

$$n = \int_{E_c}^{\infty} \sqrt{|E - E_c|} \frac{\sqrt{2} m^{*\frac{3}{2}}}{\pi^2 \hbar^3} f_n(E) dE \qquad (3)$$

$$p = \int_{-\infty}^{E_v} \sqrt{|E_v - E|} \frac{\sqrt{2} m^{*\frac{3}{2}}}{\pi^2 \hbar^3} f_p(E) dE \qquad (4)$$

where m^* is the effective mass of electron or hole and f_n, f_p are the Fermi-Dirac distribution functions for electrons and holes, respectively. The effect of electrons is neglected in this calculation, as electrons are minority carriers in a *p*-type semiconductor ($n \ll p$), resulting in no generation and/or recombination in the structures. Band diagrams and *J-V* characteristics were then obtained for different barrier conditions, demonstrated in Figure 2(a).

The Localization Landscape theory allows for a faster solution for carrier dynamics compared to the standard Schrödinger equation, especially when accounting for quantum effects. In solving the equation, we can either use the Neumann boundary condition (fixed derivatives at the boundary), Dirichlet boundary condition (fixed values at the boundary) or the periodic boundary condition. Localization Landscape theory is then used to solve for the whole device, not just the active region. For the top and bottom contact, we avoid using the Dirichlet boundary condition, which will lead *u* to become zero and *1/u* to become infinite. Therefore, in the z-direction, the Neumann boundary condition is used (where the derivative is fixed to be zero) whereas in the lateral direction, the periodic boundary condition is used.

The landscape approach decreases the height of the barrier by smoothening the potential. However, this is not a classical potential, as there exists a link to the eigenfunctions of the Schrödinger equation via a transformation of the equation. This is done by first solving $Hu = 1$ to

obtain the landscape function, u and then introducing an auxiliary function[1], ϕ where $\psi = u\phi$ to modify the Schrödinger into a new form:

$$-\frac{\hbar^2}{2m}\left[\frac{1}{u^2}div(u^2\nabla\phi)\right] + W\phi = E\phi \ , \qquad (1)$$

where $W = 1/u$ and serves as the effective potential in the Eigenvalue equation above where the eigenvalue E is the same for the modified wave equation above and the Schrödinger equation. Solving for ϕ therefore allows us to recover the original eigenfunction, $\psi = u\phi$. Thus, u and the effective potential $W = 1/u$ are more deeply connected to the Schrödinger equation and its solutions than would first appear from the Landscape equation $Hu = 1$.

As for the accounting of the density of states, according to Filoche *et al.*[2], one calculates the local carrier density by obtaining the local density of states via the equation:

$$LDOS(E,\vec{r}) = \frac{1}{2\pi^2}\left(\frac{2m_e^*}{\hbar^2}\right)^{\frac{3}{2}}\sqrt{E - W(\vec{r})} \ , \qquad (2)$$

which is identical to the classical expression to the classical expression for the local density of states.

Three square potential barriers (1.0 eV, 1.5 eV, and 2.0 eV) were tested, solving them for two different effective masses, plotting both the potential barriers as well as the corresponding landscape potential, W. The first treatment used an effective mass value of 0.2 m_0, which represents the barriers to electrons in the conduction band, as plotted in Figure SM1(a). Note that for the low effective mass here 0.2 m_0, the Landscape potential barrier $1/u_c$ is narrower and lower

than the potential E_c. A second simulation, plotted in Figure SM1(b) was made using an effective mass of 1.8 m_0 (the commonly used hole effective mass) which is representative of the barriers seen by holes in the valence band. Here, the high carrier effective mass yields an effective Landscape potential, $1/u$ to be very similar to the potential E_c, showing that using the landscape potential accurately captures the barriers for hole transport.

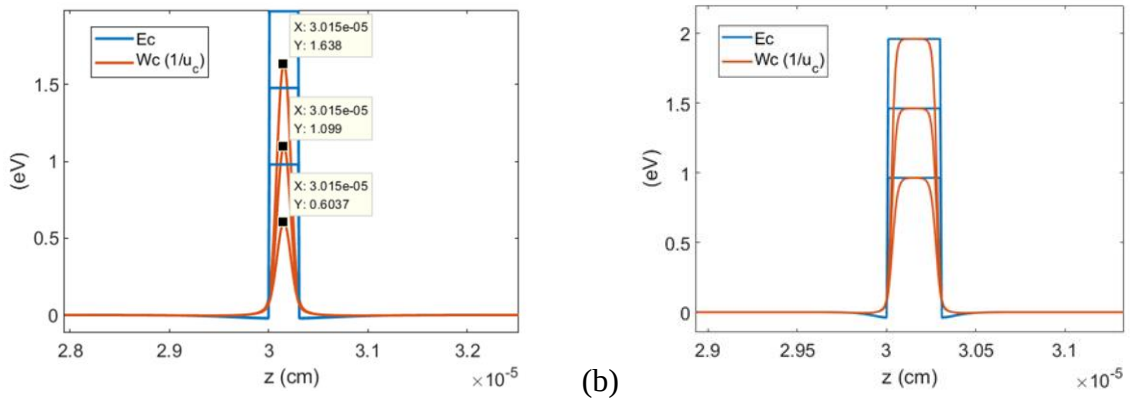

Figure 8. The solved self-consistent Poisson and Landscape potential E_c and W_c ($1/u_c$) for the effective mass of (a) 0.2 m_0 and (b) 1.8 m_0. Note that this is the typical effective mass for holes in GaN. Plots of the hole barrier would just be flipped from above.

In this work, the simulation is only used to explain the experimental observations. The Landscape model helps us consider some possible quantum effects that are involved in the transport of holes. However, there are a few other missing mechanisms that disallows us from fully matching the data, which is expected since there many non-ideal conditions in experiments such as the real activation ratio of dopants, hopping transport, defect related scattering or trapping, *etc*. The Localization Landscape model here is an additional tool to help us include more physical mechanisms that are present in the system.

The structures are modeled as barrier layers sandwiched between two *p*-type GaN layers with a doping density of 5×10^{19} cm^{-3}. Table I. summarizes the electrical parameters used in the simulation.

Layer	***p*-GaN**	***p*-AlGaN**	**UID-GaN**	**UID-AlGaN**
Hole Mobility (cm^2/Vs)	5	5	10	10
Doping Density (cm^{-3})	5×10^{19}	5×10^{19}	1×10^{16}	1×10^{16}
Activation Energy (meV)	180	220	34	34

Table 5: Electrical parameters used for UID and *p*-type GaN/AlGaN in the simulations

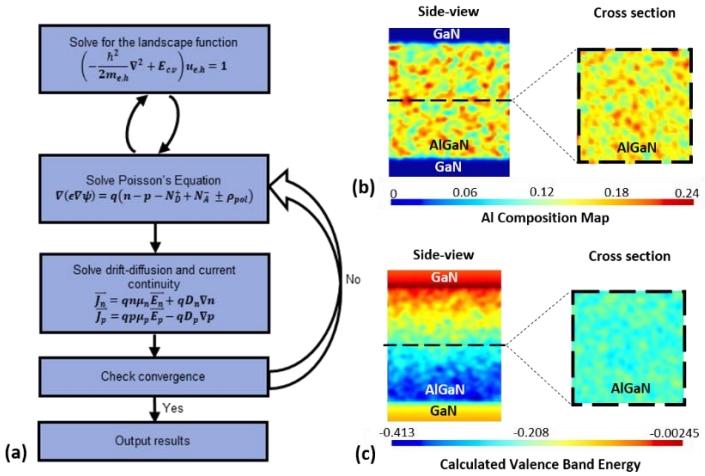

Figure 9: (Color Online) (a) Flow chart for the Gummel method incorporating Localization Landscape theory used in the Poisson-Drift-Diffusion solver in this study. Example of (b) Al composition map and (c) calculated valence band energy for a 40 nm-thick disordered AlGaN with ~ 14% average composition.

The structures are modeled as barrier layers sandwiched between two *p*-type GaN layers with a doping density of 5×10^{19} cm^{-3} (Figure 9 (a)). Figure 9 (b) and Figure 9(c) respectively show the simulated full (E_c and E_v) and valence (E_v) band diagrams of all the structures shown in Figure 9

(a). The electrical parameters used in the simulation can be found in the supplementary material. Currently, simulation models in the literature are still unable to fully simulate the TJ behavior, as tunneling remains a difficult phenomenon to simulate, especially inter-band tunneling. Theoretical studies on TJs, existing today mainly rely on the Wentzel–Kramers–Brillouin (WKB) approximation[25], which approximate the tunneling behavior, although it remains an incomplete treatment. In addition, such tunneling calculations are limited to reverse bias simulations only, since a proper forward bias modeling has to account for the tail states (dominant in the forward bias), which further complicates the model. To date, most models analyzing TJs in the weak forward bias regime have been mainly developed for narrow-bandgap semiconductors (*e.g.* Si[26] and GaAs[27] systems in multi-junction solar cells). A more comprehensive analysis of the TJ characteristics for GaN is currently under investigation and will be published elsewhere[28]. Hence, our structures forgo inclusion of TJs in the calculation by simulating only the *p*-type doped regions, focusing solely on the heterojunction region.

III. Simulation Results and Discussion

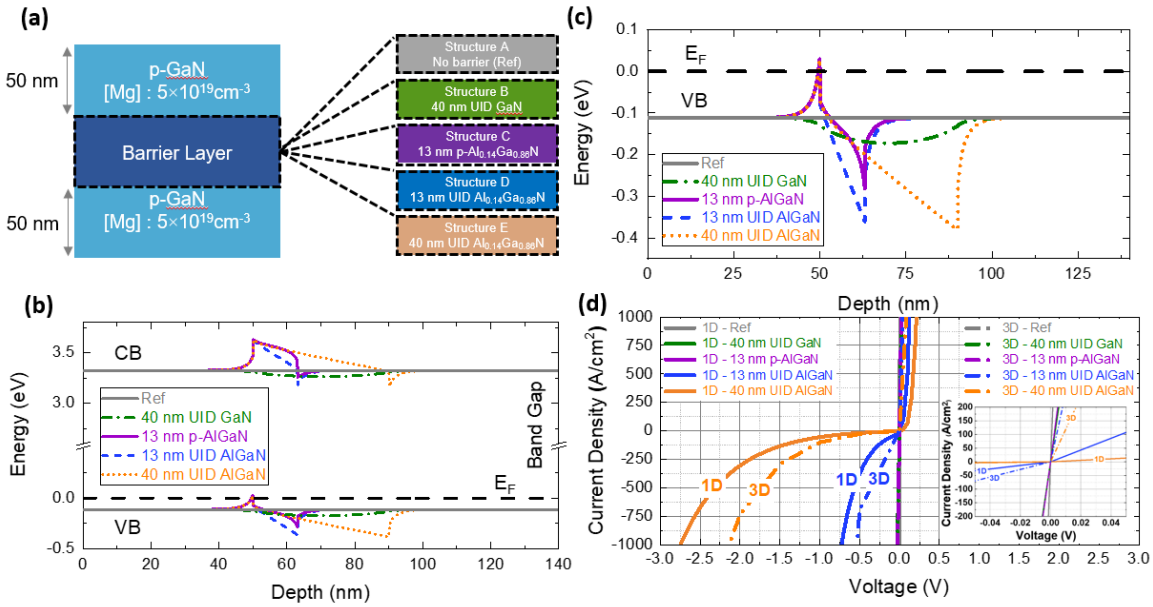

Figure 10: (Color Online) Schematics of the 5 different structures used in the simulations. The reference structures (structure A) represents a p-GaN with no barrier layer incorporated. Simulated (b) full and (c) valence band diagrams for the structures shown in (a). A drastic reduction of barrier height is observed by doping the AlGaN barrier. (d) Simulated J-V characteristics of different structures shown in (a) for 1D (solid lines) and 3D (dash-dot lines) models. Inset of (d) shows the simulated J-V curves for small voltages near zero bias, indicating a linear ohmic behavior for the reference, UID GaN, and p-AlGaN samples (Samples A to C).

Due to the larger barrier in bottom GaN/AlGaN interface compared to the top interface, hole transport sees a lower potential in one direction compared to the other (Figure 10(c)). Also, the addition of the UID GaN in between the *p*-GaN layer does not provide a significant barrier to hole transport. As there is an increase in both spontaneous and piezoelectric polarization values going from GaN to AlN, this leads to an overall increase in polarization in the structure. This, coupled with the band offset due to AlGaN having a larger bandgap, causes a large barrier to form. In contrast, the UID GaN/*p*-GaN interface would have neither of those properties to facilitate large barrier formation. Instead, a small barrier might form due to the difference in doping, generating

a weak electric field. Moreover, doping the AlGaN layer drastically reduces the barrier to hole transport (Figure 10(c)). The 1D and 3D *J*-*V* characteristics simulation results are shown in Figure 10 d). As expected, the reference structure with no barrier (sample A) shows a straight line, with no Schottky behavior, indicative of linear ohmic behavior (as indicated in the inset of Figure 10(d)). The thickness of the UID AlGaN layer correlates with the voltage drop in both forward and reverse direction for a given *J*. The voltage drops in the reverse direction are much larger than those in the forward direction, which is attributed to the asymmetric band diagrams shown in Figure 10(c). A *p*-type doping of the AlGaN results in little to no additional voltage drops in either direction, which is likely due to the reduced barrier height as shown in Figure 10(c). While standard 1D Poisson-drift-diffusion calculations may also yield a similar result on the effects of *p*-type doping of the AlGaN barrier on hole transport, a 3D simulation with Landscape theory will provide a completer and more accurate picture. The 3D model yields slightly larger current values compared to 1D model, as the landscape potential smoothens and lowers the barriers to hole transport (more details can be found in the supplementary material). Also, there is little to no additional voltage drops in the UID GaN layer compared to the reference, due to the insignificant barrier heights in either direction (Figure 10(c)).

IV. Experimental Procedure

To experimentally verify the observed behavior in simulations, 5 structures were grown and processed. Figure 3(a) schematically shows the 5 structures grown and processed in this study. All the samples were epitaxially grown by a Veeco Gen 930 NH_3-MBE system on 1 cm^2 MOCVD-grown GaN/Sapphire templates from Lumilog Saint-Gobain (More growth details can be found in the supplementary material). First, a ~ 200 nm-thick *n*+ GaN contact layer ([Si]: 5×10^{19} cm^{-3}) was grown sandwiched between two layers of 150 nm *n*-GaN ([Si]: 5×10^{18} cm^{-3}) at a substrate

temperature of ~ 820 ºC. Then, an *n*-to-*p* TJ structure, consisting of highly doped *p*++ ([Mg]: 5×10^{20} cm^{-3})- *n*++([Si]: 5×10^{20} cm^{-3}) junction (10 nm/ 10 nm) was grown. The doping of the TJ structures were optimized through separate calibration experiment sets[28]. Intentional growth interruptions were introduced at the interface between the *n*++ and *p*++ of the TJs followed by a 3 min buffered hydrofluoric acid (BHF) treatment and regrowth for all the structures, as the BHF treatment has shown to have a significant impact on the TJ properties[28,29]. The regrown TJ structure was then followed by a 50 nm-thick *p*-GaN growth ([Mg]: 5×10^{19} cm^{-3}) at a substrate temperature of 750 ºC. 5 samples were then grown: Sample A with no barrier layer, Sample B with a 40 nm-thick UID GaN layer, Sample C with a 13 nm-thick *p*-$Al_{0.14}Ga_{0.86}N$ ([Mg]: 5×10^{19} cm^{-3}) as well as Sample D and E with 13 nm and 40 nm UID $Al_{0.14}Ga_{0.86}N$ layers respectively. All the samples were then capped with a 50 nm *p*-GaN ([Mg]: 5×10^{19} cm^{-3}) and a 10 nm-thick *p*++ ([Mg]: 3×10^{20} cm^{-3}) contact layer. The thicknesses and doping levels for each of the layers were calibrated on separate calibration structures using high-resolution X-ray diffraction (HRXRD) (Figure 3(b)) and secondary-ions mass spectroscopy (SIMS) (Figure 3 (c)), respectively. Average Al composition in the AlGaN layers were also calibrated by HRXRD on separate calibration samples (Figure 3(b)).

All the samples were then processed using a standard mesa-isolated device structure design with circular patterns. First, a blanket SiO_2 layer (~ 300 nm) was deposited using a plasma-enhanced chemical vapor deposition (PECVD). Then, the mesas were defined using a self-aligned wet etching of the SiO_2 using BHF followed by 400 nm of dry etching by a reactive-ion etcher (RIE). Another SiO_2 layer was deposited after the mesa formation to passivate the sidewalls to mitigate leakage issues due to sidewall damage by RIE[30,31]. Pd/Au (30 nm/300 nm) and Ti/Au (30 nm/300 nm) metal stacks were then deposited by electron-beam (E-Beam) deposition to serve as *p*- and *n*-contacts, respectively.

V. Experimental Discussion and Results

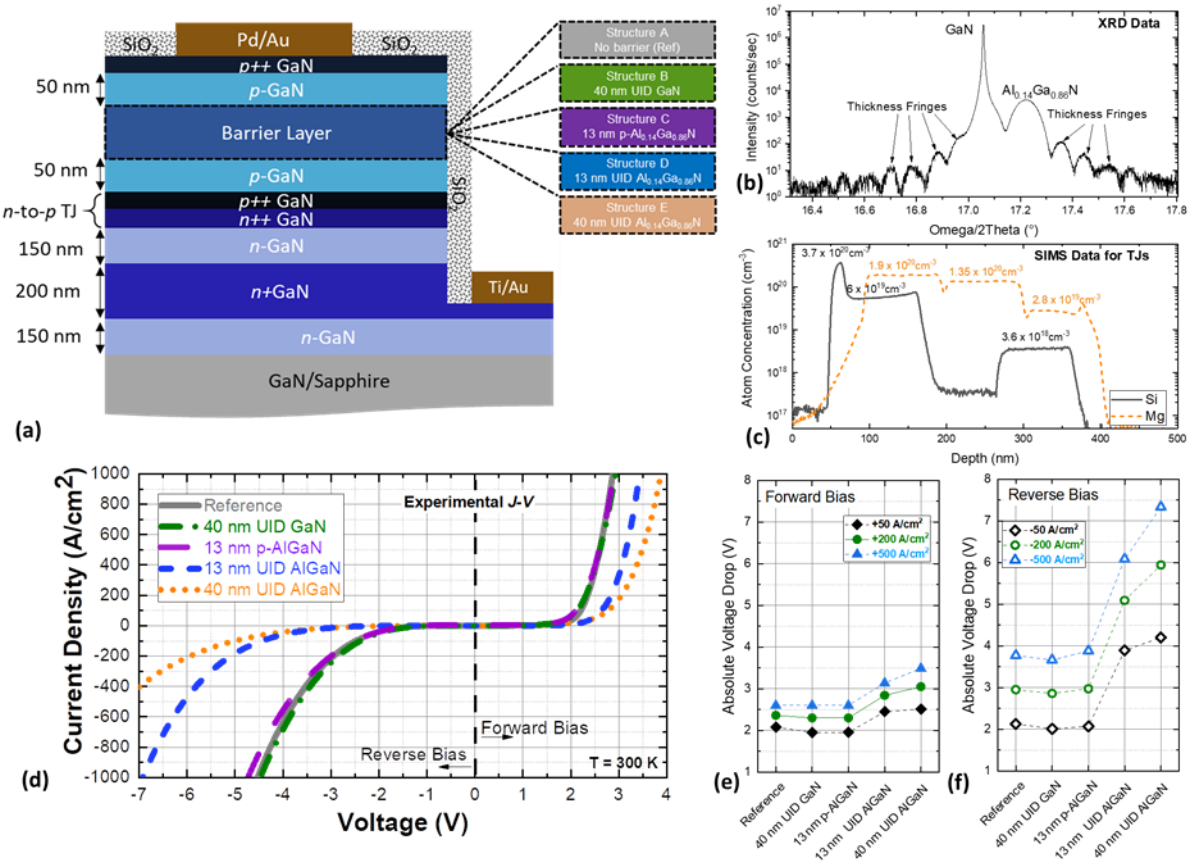

Figure 11: (Color Online) (a) Schematics of all the 5 vertical structures grown and processed for the experimental investigations. All the structures include an n-to-p TJ (10 nm/10 nm). Sample (b) HRXRD and (c) SIMS evaluations of calibration structures for $Al_{0.14}Ga_{0.86}N$ barrier layer and doping levels for the TJ structure, respectively. (d) Experimental J-V plots for all the samples measured at room temperature (T = 300 K). Absolute (e) forward and (f) reverse voltage drops at 50A/cm^2, 200A/cm^2, and 500A/cm^2.

Electrical measurements were conducted using a probe station with tungsten probes connected to a Keithley 4200A-SCS Parameter Analyzer. A fully vertical hole transport is expected in such structures, since the vertical distance in the *p*-region (~ 100 nm) is much smaller than lateral dimension (~ 10 µm) from the edge of the contact to the edge of the mesa. Hence, *J* is calculated by dividing the injected current to the area of the Pd/Au *p*-contact. Figure 11(d) indicates the *J-V* characteristics of all the samples. As predicted by the simulation results, strong correlations between the GaN *vs.* AlGaN, doped vs. UID, and thin *vs.* thick $Al_{0.14}Ga_{0.86}N$ and *J-V* characteristics

were observed. Figure 11 (e) and (f) respectively indicate forward and reverse voltage drops at 50A/cm^2, 200A/cm^2, and 1000A/cm^2, for representative devices among a statistically significant number of devices on each sample. The voltage drops in the reverse direction is larger than those in the forward direction, supporting the simulation results of Figure 10. Similar to the simulation results, the UID GaN and *p*-AlGaN structures show negligible voltage drops compared to the reference structure. On the other hand, the UID AlGaN results in large voltage drops for thin (13 nm) and thick (40 nm) AlGaN structures. Also, the voltage drop is strongly dependent on the thickness of the AlGaN layer (*e.g.* ~ 1.5 V larger reverse voltage drop at 500 A/cm^2 for thick *vs.* thin UID AlGaN) as predicted by the band diagram (Figure 10 (c)) and *J-V* (Figure 10(d)) simulation results.

The voltage drops on all the structures, including the reference structure with no barrier, are larger than those from simulation results (Figure 10(d)), mainly due to the voltage drop across the TJs (<1.5 V at 20 A/cm^2). While the calculated absolute voltage drop values do not perfectly match the experimental values, the simulation results correctly predict the trends observed in experiments. The discrepancy partially arises from the fact that our modeling is unable to simulate *J-V* behaviors of TJs, as mentioned earlier. To better compare the 3D simulation and the experimental results, the *J-V* data of reference TJ was added to the 3D simulation *J-V* characteristics (voltages were added for fixed *J*) for 13 nm and 40 nm UID AlGaN samples. Since no indication of negative differential resistance (NDR) was observed in our TJ reference, we treated the TJs as dynamic resistors past turn-on. Also, as the TJs are far away from the AlGaN heterojunction, we assume negligible electrical interactions between the two. The summation of the TJ *J-V* and the 3D simulation data is expected to improve the accuracy of the simulation by accounting for the drop voltage across the TJs, the contact resistance, and the series resistance in

the semiconductor. Prior to the summation, the calculated voltage drop on reference simulation structure was subtracted from the simulation *J-V*s to avoid double counting of the series resistance. The *p*-type AlGaN and UID GaN samples were excluded from the analysis as their *J-V* characteristics were practically the same as the reference structure. Figure 12 compares the experimental and the corrected 3D simulation results for 13 nm and 40 nm UID AlGaN samples. According to Figure 4, the trends in the voltage drop for the corrected 3D simulation and the experiment are the same. However, the corrected 3D simulation underestimates the drop voltage values. Also, in forward bias, the trend in the drop voltage for thin and thick UID AlGaN is less pronounced in the corrected 3D simulation compared to the experiment. The remaining differences between the experiment and simulation here can be due to slight sample to sample variations and incomplete picture of the modeling. The analysis will be extended to improve the accuracy of the modeling to better match experiments in the future. Finally, compared to the electrons[19], holes show much larger voltage drops in either directions, which is attributed to its larger effective mass, and thus reduced percolation transport through alloy disorder. A more detailed comparison of electron and hole transport through disordered alloys using 1D and 3D simulations is also under investigation and will be published elsewhere.

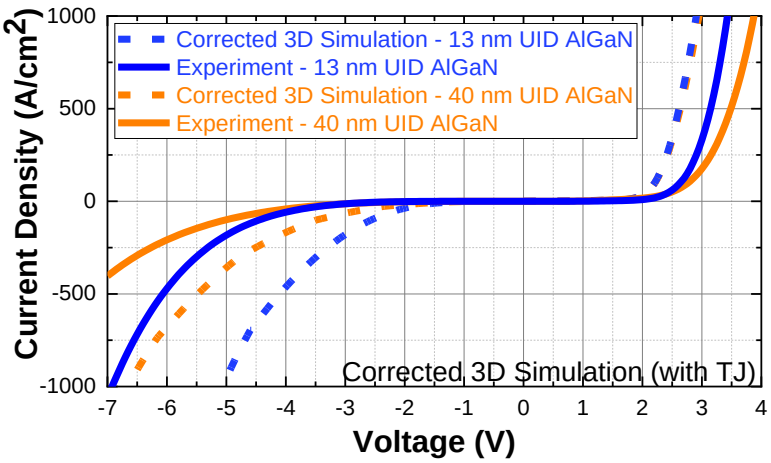

Figure 12. (Color Online) J-V characteristics comparison of the experiment and the corrected 3D simulations (to include J-V characteristics of TJ reference) for 13 nm and 40 nm UID AlGaN structures. The J-V data of the reference TJ is added to the 3D simulation of Figure 10(d) after subtraction of the calculated series resistance to avoid double accounting the series resistance effects.

Our findings have direct implications on GaN-based optoelectronics. For instance, InGaN-based visible LEDs and lasers today use either UID or *p*-type AlGaN EBLs near the *p*-side of the junction to avoid electron overflow and to enhance their external quantum efficiency (EQE)[10,32–34]. However, the UID AlGaN EBLs were thought to impinge a barrier to the hole injection (as also proven in this work), thus lowering the injection efficiency and EQE. On the other hand, the designs incorporating *p*-type doping of AlGaN EBLs were implemented to improve the hole injection into the active region, maintaining the low electron overflow[1,35–37]. However, there is no direct experimental evidence for reduction of the barrier to hole transport through EBLs by *p*-type doping, as a unipolar transport have not been investigated for holes so far. Our results show that a moderate *p*-type doping ([Mg]: 5×10^{19} cm^{-3}) of AlGaN layers (14 nm-thick $Al_{0.14}Ga_{0.86}N$, which is similar to practical EBL designs) significantly reduces the barrier to the hole transport, supporting the need for *p*-type doping of EBLs for high-efficiency LEDs. In addition, we also propose the unipolar hole transport designs incorporating *n*-to-*p* TJs as a test vehicle to

unambiguously determine the real barriers to transport (without the complexities of recombination). Future studies will also include bulk and QW InGaN active regions to investigate the barriers for hole transport.

VI. Conclusion

In summary, we theoretically and experimentally investigate hole transport through disordered AlGaN in *p*-type unipolar structures. Both theoretical and experimental results indicate that no significant barrier was observed when UID GaN was used as a barrier within the *p*-GaN layer. On the other hand, even a thin (13 nm) UID $Al_{0.14}Ga_{0.86}N$ is enough to provide a large barrier to hole transport in both reverse (~100% larger drop voltage compared to the reference at 50 A/cm^2) and forward (~25% larger drop voltage compared to the reference at 50 A/cm^2) directions. However, a *p*-type doping of the $Al_{0.14}Ga_{0.86}N$ layer results in a drastic reduction of the barrier to hole transport in both directions, as proven by the band diagrams and *J*-*V* simulations as well as experimental results. The results are beneficial in understanding the behavior of hole transport through various designs such as EBLs and other potential barriers in LEDs, lasers, HEMTs, intersubband structures, and beyond.

VII. References

[1] D. Feezell and S. Nakamura, Comptes Rendus Phys. **19**, 113 (2018).
[2] H. Morkoç, *Handbook of Nitride Semiconductors and Devices, Materials Properties, Physics and Growth* (John Wiley & Sons, 2009).
[3] C. Bayram, Z. Vashaei, and M. Razeghi, Appl. Phys. Lett. **96**, 42103 (2010).
[4] M. Hermann, E. Monroy, A. Helman, B. Baur, M. Albrecht, B. Daudin, O. Ambacher, M. Stutzmann, and M. Eickhoff, Phys. Status Solidi C **1**, 2210 (2004).
[5] G. Gupta, M. Laurent, J. Lu, S. Keller, and U.K. Mishra, Appl. Phys. Express **7**, 14102 (2013).
[6] A.F.J. Levi and T.H. Chiu, Appl. Phys. Lett. **51**, 984 (1987).
[7] S. Chowdhury, M.H. Wong, B.L. Swenson, and U.K. Mishra, IEEE Electron Device Lett. **33**, 41 (2012).
[8] I. Ben-Yaacov, Y.-K. Seck, U.K. Mishra, and S.P. DenBaars, J. Appl. Phys. **95**, 2073 (2004).
[9] E.F. Schubert, T. Gessmann, and J.K. Kim, in *Kirk-Othmer Encycl. Chem. Technol.* (American Cancer Society, 2005).
[10] Y.-K. Kuo, J.-Y. Chang, and M.-L. Chen, in *Phys. Simul. Optoelectron. Devices XVIII*, edited by B. Witzigmann, F. Henneberger, Y. Arakawa, and M. Osinski (SPIE, 2010), pp. 469–477.
[11] M. Kneissl and J. Rass, editors , *III-Nitride Ultraviolet Emitters: Technology and Applications* (Springer International Publishing, 2016).
[12] T. Nishida, H. Saito, and N. Kobayashi, Appl. Phys. Lett. **79**, 711 (2001).

[13] M. Beeler, E. Trichas, and E. Monroy, Semicond. Sci. Technol. **28**, 074022 (2013).
[14] C. Gmachl, H.M. Ng, and A.Y. Cho, Appl. Phys. Lett. **77**, 334 (2000).
[15] M. Filoche and S. Mayboroda, Proc. Natl. Acad. Sci. **109**, 14761 (2012).
[16] M. Filoche, M. Piccardo, Y.R. Wu, C.K. Li, C. Weisbuch, and S. Mayboroda, Phys. Rev. B **95**, 1 (2017).
[17] C.-K. Li, M. Piccardo, L.-S. Lu, S. Mayboroda, L. Martinelli, J. Peretti, J.S. Speck, C. Weisbuch, M. Filoche, and Y.-R. Wu, Phys. Rev. B **95**, 144206 (2017).
[18] H.-H. Chen, J.S. Speck, C. Weisbuch, and Y.-R. Wu, Appl. Phys. Lett. **113**, 153504 (2018).
[19] D.A. Browne, M.N. Fireman, B. Mazumder, L.Y. Kuritzky, Y.-R. Wu, and J.S. Speck, Semicond. Sci. Technol. **32**, 025010 (2017).
[20] D.N. Nath, Z.C. Yang, C.-Y. Lee, P.S. Park, Y.-R. Wu, and S. Rajan, Appl. Phys. Lett. **103**, 022102 (2013).
[21] X.A. Cao, H. Cho, S.J. Pearton, G.T. Dang, A.P. Zhang, F. Ren, R.J. Shul, L. Zhang, R. Hickman, and J.M. Van Hove, Appl. Phys. Lett. **75**, 232 (1999).
[22] D.W. Jenkins and J.D. Dow, Phys Rev B **39**, 3317 (1989).
[23] H.K. Gummel, IEEE Trans. Electron Devices **11**, 455 (1964).
[24] D.N. Arnold, G. David, D. Jerison, S. Mayboroda, and M. Filoche, Phys Rev Lett **116**, 056602 (2016).
[25] S. Krishnamoorthy, D.N. Nath, F. Akyol, P.S. Park, M. Esposto, and S. Rajan, Appl. Phys. Lett. **97**, 203502 (2010).
[26] N. Moulin, M. Amara, F. Mandorlo, and M. Lemiti, J. Appl. Phys. **126**, 033105 (2019).
[27] M. Hermle, G. Létay, S.P. Philipps, and A.W. Bett, Prog. Photovolt. Res. Appl. **16**, 409 (2008).
[28] M. Monavarian, K.S. Qwah, Y. Zhang, and J.S. Speck, (In Preparation).
[29] S. Lee, C.A. Forman, C. Lee, J. Kearns, E.C. Young, J.T. Leonard, D.A. Cohen, J.S. Speck, S. Nakamura, and S.P. DenBaars, Appl. Phys. Express **11**, 062703 (2018).
[30] M.S. Wong, D. Hwang, A.I. Alhassan, C. Lee, R. Ley, S. Nakamura, and S.P. DenBaars, Opt. Express **26**, 21324 (2018).
[31] M.S. Wong, C. Lee, D.J. Myers, D. Hwang, J.A. Kearns, T. Li, J.S. Speck, S. Nakamura, and S.P. DenBaars, Appl. Phys. Express **12**, 097004 (2019).
[32] S.-H. Han, D.-Y. Lee, S.-J. Lee, C.-Y. Cho, M.-K. Kwon, S.P. Lee, D.Y. Noh, D.-J. Kim, Y.C. Kim, and S.-J. Park, Appl. Phys. Lett. **94**, 231123 (2009).
[33] O. Svensk, P.T. Törmä, S. Suihkonen, M. Ali, H. Lipsanen, M. Sopanen, M.A. Odnoblyudov, and V.E. Bougrov, J. Cryst. Growth **310**, 5154 (2008).
[34] J. Cho, S. Cho, B.J. Kim, S. Chae, C. Sone, O.H. Nam, J.W. Lee, Y. Park, and T.I. Kim, Appl. Phys. Lett. **76**, 1489 (2000).
[35] Y. Ji, Z.-H. Zhang, Z. Kyaw, S. Tiam Tan, Z. Gang Ju, X. Liang Zhang, W. Liu, X. Wei Sun, and H. Volkan Demir, Appl. Phys. Lett. **103**, 053512 (2013).
[36] K. Domen, A. Kuramata, and T. Tanahashi, Appl. Phys. Lett. **72**, 1359 (1998).
[37] K. Domen, R. Soejima, A. Kuramata, K. Horino, S. Kubota, and T. Tanahashi, Appl. Phys. Lett. **73**, 2775 (1998).

2.2 Vertical transport through p-type InGaN Heterostructures

I. Introduction

III-nitride materials have garnered considerable interest over the last few decades for their extensive applications in electronics and optoelectronics, including laser diodes [1] for automotive lighting [2], solid-state lighting [3], and communications [4] and light-emitting diodes (LEDs) [5] for general lighting [3,6], displays [7], and visible-light communication (VLC) [8,9] technologies. Typical InGaN-based LED designs consist of active regions with one or more InGaN quantum wells (QWs), utilizing the narrower bandgap of InGaN (where the emission color being tunable by adjusting the In content) compared to GaN to ensure carrier confinement and facilitate recombination between the electrons and holes. Another application of III-nitride materials in the field of optoelectronics is in photovoltaic cells [10], due to the wide tunability of the bandgap to access the full-solar spectrum in multi-junction solar cells. InGaN/GaN heterostructures have also been used in visible-range photodetectors [11] as optical receivers in VLC links. Despite the wealth of research in the field of III-nitride devices, the details of carrier transport within the QWs active regions remains poorly understood.

To study carrier transport, unipolar heterostructures have been used as test vehicles for theoretical models as they are only subject to carrier transport behavior, circumventing the need to account for radiative and non-radiative recombination behavior. This approach was first proposed by Browne *et al.* [12] for the case of electron transport in InGaN using unipolar *n*-type GaN/InGaN/GaN heterostructures grown by ammonia-assisted MBE (NH_3-MBE) and metalorganic chemical vapor deposition (MOCVD). The results indicated that even a 3 nm thick $In_{0.13}Ga_{0.87}N$ layer would act as a barrier to electron transport [12]. The notion of InGaN, which has a lower bandgap than GaN, as a barrier may seem counterintuitive at first glance but can be explained using the concept of polarization fields. III-nitride heterostructures, such as InGaN/GaN,

feature piezoelectric as well as spontaneous polarization fields [13]. Due to the difference in lattice constants between GaN and InGaN materials, the compressive strain affects the piezoelectric component of the polarization, causing significant polarization discontinuity between GaN and InGaN layers. The polarization discontinuity results in the formation of a polarization-induced charge at the interface between GaN and InGaN, with hole accumulating on the bottom interface and the ionized acceptors (N_A^-) on the top (assuming the structure is c-plane). Thus, an electric field forms at both interfaces which in turn induces large band-bending in the region, forming a barrier against both electron and hole transport as shown in Figure 13 [14].

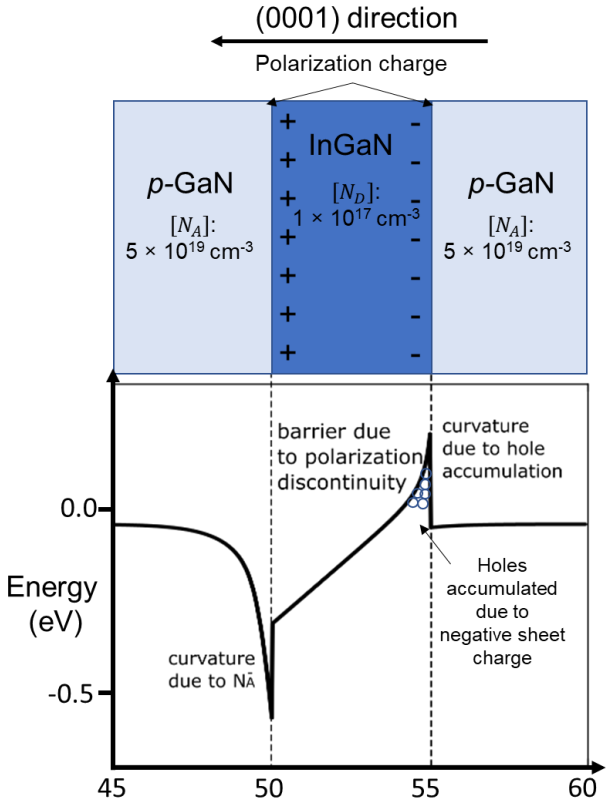

Figure 13: Diagram detailing the sheet charge due to polarization discontinuities and the resultant valence band profile. The hole accumulation causes band curvature on the right of the QW and the ionized acceptors (N_A^-) on the left.

Previous studies focused solely on the electron transport mechanism and is not applicable when discussing the physics of hole transport (due to their different effective masses and

conduction versus valence band offset), which is of great interest in the field of electronics and optoelectronics. With regards to hole transport structures, we [15] demonstrated electrical measurements on *p*-type unipolar AlGaN heterostructures, which were enabled by *n*-to-*p* tunnel junctions (TJs). The results indicated that UID AlGaN can act as a barrier to hole transport and that a moderate *p*-type doping of the AlGaN layer could suppress the barrier to hole injection, indicating the necessity of doping the AlGaN electron-blocking layer (EBL) for efficient hole injection in LED structures.

In this paper, we report the computational and experimental investigation of vertical hole transport through InGaN layers in *p*-type unipolar heterostructures. The transport behavior is expected to be different for InGaN compared to AlGaN due to their different bandgaps and the corresponding band structures. For theoretical calculations, a computational model using standard drift-diffusion formalism that incorporate Localization Landscape theory, both in 1D and 3D are used. Our 3D calculations also consider the effects of random alloy fluctuations within the InGaN region to simulate the disordered potential that carriers are exposed to see when transporting through the structure. To support the device simulations, unipolar *p*-type vertical transport structures are grown using NH_3-MBE, with the unipolar InGaN regions sitting on top of an *n*-to-*p* TJ. The tunnel junction layer is pivotal for our vertical transport structure as it helps with current spreading, due to the high resistivity of the *p*-GaN material. This could potentially cause the current to go through the sidewalls of the mesa structures instead of the InGaN layer. Apart from that, exposure of the *p*-GaN layer to ion damage during the reactive-ion etch process could cause material damage, generating nitrogen vacancies [16] that act as shallow donors which behave as compensating defects [17]. The experimental and computational data indicate an existence of

barriers to hole transport through unintentionally doped (UID) InGaN DHs and QWs in both reverse and forward bias.

Traditional 1D simulation packages, which use Schrödinger-Poisson-Drift-Diffusion calculations, consistently overestimate the turn-on voltage in LEDs. This is due to the assumption of abrupt junctions between GaN and InGaN as well as uniform alloy composition within the QWs [18]. However, incorporating the random alloy requires a huge amount of mesh nodes, which in turn requires an excessive amount of time to solve for the eigenstates due to the complexity of accounting for alloy disorder [18]. Hence, a new theory called Localization Landscape theory was proposed to solve the effective quantum potential without solving the eigenvalue problem. This theory was initially used to solve for systems with Anderson localization [20]. It can be included in Poisson and drift-diffusion solvers for modeling the carrier transport and recombination characteristics within LEDs [18,19]. Li *et. al* [18] estimated a significant reduction (nearly three orders of magnitude) in computation time when using the Localization Landscape theory compared to regular Schrödinger-Poisson methods for solving for disordered potentials.

II. Simulation Procedure

The band diagrams and current density-voltage (*J-V*) simulations were obtained by conducting Poisson-drift-diffusion calculations. The algorithm used by the software is the Gummel iteration method (Figure 15), which is a widely used algorithm used for solving for band energies as well as *J-V* characteristics [21]. In addition, the software also uses Localization Landscape theory [18], whereby instead of solving the time-independent Schrödinger eigen equation,:

$$\hat{H}\psi = \hat{E}\psi \tag{1}$$

it solves an ordinary differential equation:

$$\hat{H}u = 1 \tag{2}$$

where $\hat{H}$ is the Hamiltonian operator:

$$\hat{H} = -\hbar^2 \nabla \left(\frac{1}{2m^*} \nabla \right) + E_{c,v} \tag{3}$$

ψ is the eigenfunction for the Hamiltonian operator and u is the landscape function.

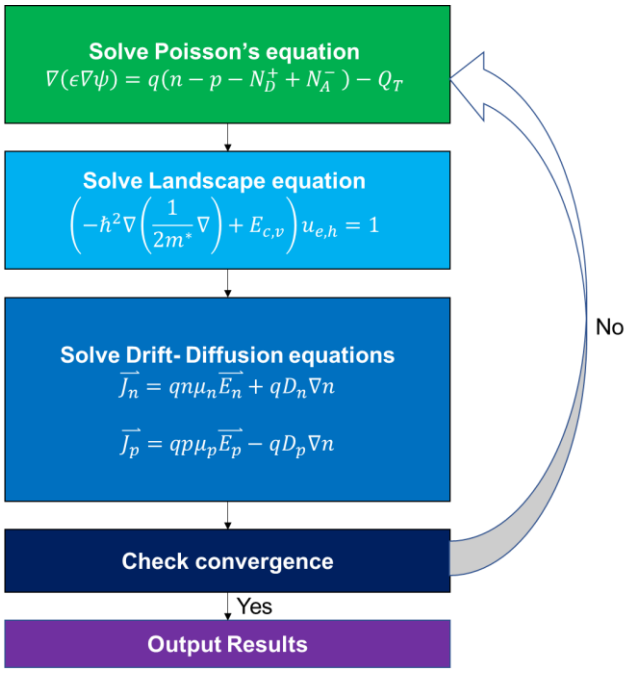

Figure 14 : Flow chart for the Gummel Method which details the Poisson-Drift-Diffusion calculations as well as incorporating Localization Landscape theory.

The theory posits that the locations of eigenstates, ψ in a specified potential V can be predicted using the solution of the equation, u. This is done by defining an effective potential called the Landscape potential, *W*, where *W=1/u*. It was shown that *W* delimits the regions where the eigenstates are located [14] .Thus, the landscape potential can be seen as an effective confining potential which partitions a system into subregions where low energy eigenstate are localized. The original eigenfunction, ψ is recovered from both *W* and *u* via an auxiliary function described in [22], thus showing that they are intrinsically connected to the Schrödinger equation.

To model the InGaN region of the structure, we have conducted both 1D and 3D simulations. The parameters of our simulations are tabulated on Table 1. The 1D model assumes

the InGaN alloy region to be homogeneously made of a semiconducting material that has properties that are interpolated between GaN and InN. This is unrealistic as actual alloys are not homogeneous and have GaN and InN randomly distributed throughout the region. Thus, we decided to conduct a 3D simulation, which allows for the incorporation of these compositional fluctuations within the InGaN alloy. According to Browne et al., [12]these fluctuations were found to improve electron transport within the alloy material as they result in a locally varying strain profile, which in turn affects the strength of the piezoelectric polarization field. Thus, regions of lower indium composition would have lower barrier heights, facilitating the injection of electrons. These regions where electrons have a lower barrier have been dubbed "percolation pathways" by previous studies [15,23]. For the 3D simulations, a random In composition map with an average composition of choice (~10%) was used as one of the input parameters for the full 3D calculation.

The alloys are generated by constructing a grid of lattice sites, with a distance of 2.833 Å between sites and with Indium and Gallium being randomly assigned to each site. Following this, a Gaussian broadening is conducted to smoothen the alloy disorder using the following equation:

$$x(r_i) = \frac{\sum_j atom(j) \times e^{-\frac{(r_j - r_i)^2}{2\sigma^2}}}{\sum_j e^{-\frac{(r_j - r_i)^2}{2\sigma^2}}} \qquad (4)$$

where x is the composition in the region, with the sum going over all atomic sites j of the domain. The atom(j) is randomly decided to be either Ga or In and σ is the half-width of the Gaussian broadening parameter. The value of this parameter was chosen to be σ = 2a (≈0.6 nm). This was chosen based on the findings of Reference [23] where they compared simulations with experimental APT data. In their work, APT data showed that the average indium composition along the quantum well had a full-width-at-half-maximum of 1.5 nm. This tallies with our choice of σ = 2a for the Gaussian Broadening width, 2σ. Since a is the lattice constant of GaN, which is

0.3186 nm, this means 2σ = 1.274 nm, which is very close the FWHM value seen from the reference. This contrasts with the 1D simulations, which uses an average composition map with no random compositional fluctuations. The entire mesh is generated with a software called GMesh, with the equations being self-consistently solved over each node.

Layer	***p*-GaN**	***UID*-InGaN (*n*-type)**	**GaN quantum barriers (*n*-type)**
Hole Mobility (cm^2/Vs)	5	10	10
Doping (cm^{-3})	5×10^{19}	1×10^{17}	1×10^{17}
Activation energy (meV)	180 (Mg)	34 (O)	34 (O)

Table 6 : Doping levels in each layer in the simulation and their activation energies

Units	**GaN**	**InN**
$\boldsymbol{E_g(eV)}$	3.437	0.61
$\boldsymbol{m_e^{\|\|}\ (m_0)}$	0.21	0.07
$\boldsymbol{m_e^{\perp}\ (m_0)}$	0.2	0.07
$\boldsymbol{m_{hh}\ (m_0)}$	1.87	1.61
$\boldsymbol{m_{lh}\ (m_0)}$	0.14	0.11
$\boldsymbol{\epsilon_r}$	10.4	15.3
$\boldsymbol{e_{33}\ (\frac{C}{cm^2})}$	0.73	0.73
$\boldsymbol{e_{31}\ \left(\frac{C}{cm^2}\right)}$	-0.49	-0.49
$\boldsymbol{e_{15}\ \left(\frac{C}{cm^2}\right)}$	-0.40	-0.40
Bowing parameter	1.4	
Mass of electron, m_0 (kg)	9.11×10^{-31}	

Table 2 : Bandgap, effective masses, relative permittivity, bowing parameter [24,25] and piezoelectric coefficient values [26] used in the simulations for the GaN and InN.

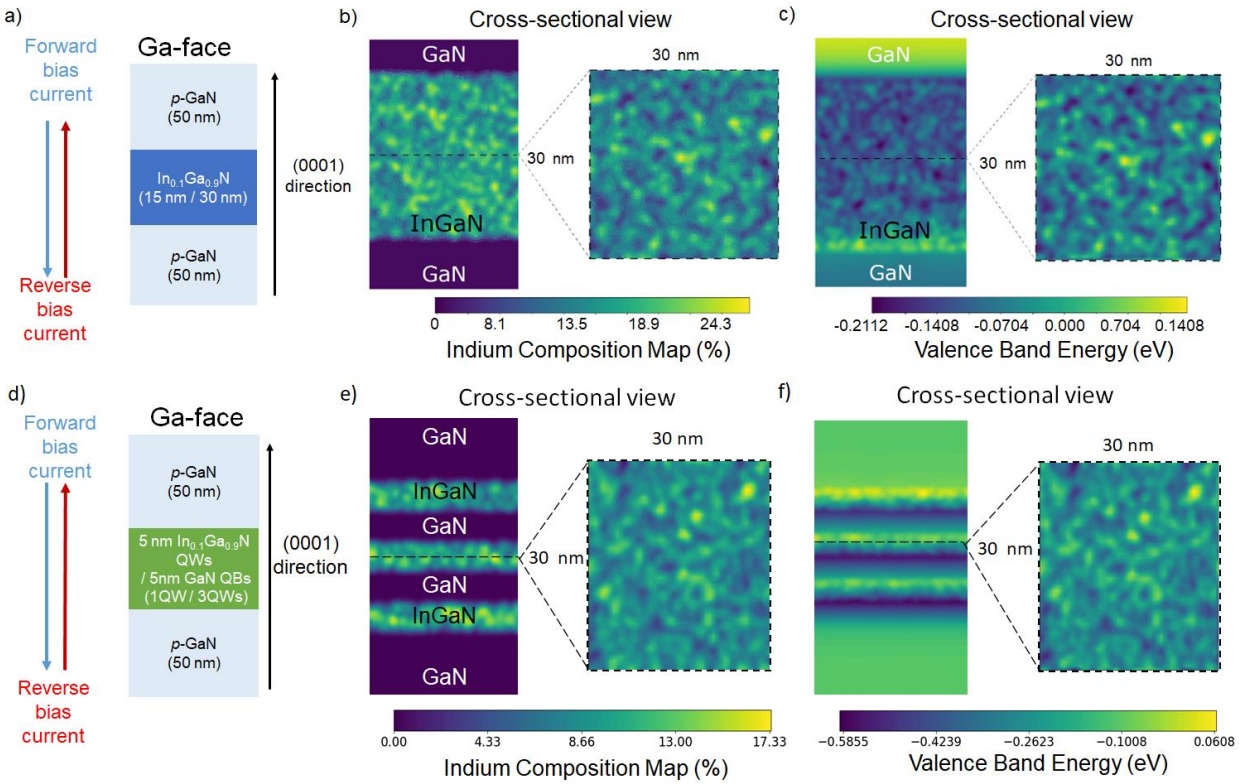

Figure 15: Schematics of the simulated DH (a) and MQW(d) devices along with the growth polarity and directionality of forward bias and reverse bias current. Figures (b) and (c) shows the resulting Indium composition map and valence band energy map respectively for 30 nm thick InGaN structure. Figure (e) and (f) shows the same maps for the 3 × 5 nm MQW structure.

The conduction band (E_c) and valence band (E_v) energies are calculated by solving Poisson's equation. These energies are plugged into the landscape equation and then used to calculate landscape potential for electrons (W_e) and holes (W_h). Following that, they were then used to obtain electron and hole carrier densities by integrating the Fermi-Dirac distribution function over the energy bands using the following integrals:

$$n = \int_{W_e}^{\infty} \sqrt{|E - W_e|}\, \frac{\sqrt{2} m_n^{*\frac{3}{2}}}{\pi^2 \hbar^3} f_n(E) dE \tag{3}$$

$$p = \int_{-\infty}^{W_h} \sqrt{|W_h - E|}\, \frac{\sqrt{2} m_p^{*\frac{3}{2}}}{\pi^2 \hbar^3} f_p(E) dE \tag{4}$$

where m_n^*, m_p^*, f_n and f_p are the effective masses and Fermi-Dirac distribution functions for electrons and holes, respectively. The simulated temperature of the device is assumed to be 300

K. Since electrons are minority carriers in *p*-type unipolar structures, their effects are assumed to be negligible and thus, no appreciable recombination occurs within the structures.

III. Simulation Results and Discussion

Band diagram calculations are obtained for a 15 nm c-plane Ga-polar $In_{0.1}Ga_{0.9}N$ layer, as demonstrated in Figure 16. The structures consist of the InGaN barrier layer sandwiched between Mg-doped *p*-GaN layers with a doping density of 5×10^{19} cm^{-3}. Using the calculated band energies, estimated barrier heights for forward and reverse bias are indicated by arrows in Figure 16(b). Finally, *J-V* results were obtained for both 1D and 3D unipolar structures for InGaN DH layers of 15 nm and 30 nm thicknesses. In the context of our unipolar device, we have defined forward bias as injecting holes from the top contact towards the bottom contact and vice versa for reverse bias. The main takeaway from the band energy simulation results is that holes experience barriers which are asymmetric in forward and reverse biases, with the reverse bias case generating a larger barrier compared to the forward case. In either forward or reverse bias, the barrier to the hole transport becomes larger as the thickness of the InGaN layer is increased.

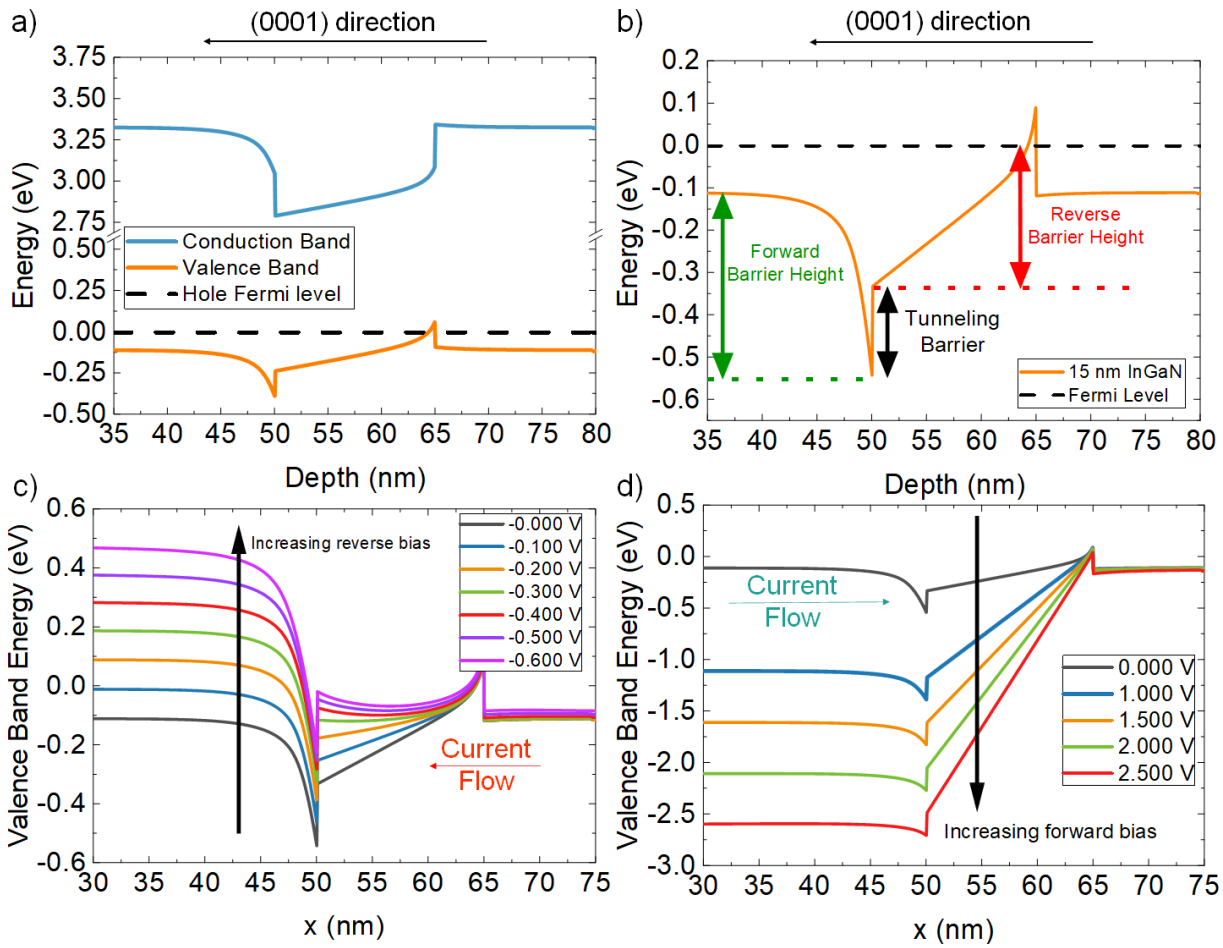

Figure 16: (a) Full band diagram for the unipolar 15 nm InGaN DH structure. Valence band diagrams for *p*-type unipolar structures with a 15 nm layer of $In_{0.1}Ga_{0.9}N$ at (b) zero, (c) reverse and (d) forward bias.

The quantified barrier heights for each bias were then plotted in Figure 17(a). The barrier heights are quantified by subtracting the highest from the lowest valence band energies in the direction of hole transport, as shown in Figure 16 (a). The maximum calculated barrier height for the 15 nm and 30 nm InGaN DH structures were 0.40 eV and 0.45 eV respectively. The barrier height vs bias voltage plot (Figure 17(a)) is asymmetric with respect to the zero-bias point, as expected from the asymmetric band diagrams (Figure 16 (a)) for the case of InGaN DHs. For example, the absolute barrier height to the hole transport at +1 V bias is higher compared to the barrier at -1 V (0.15 eV vs 0.1 eV). The barrier asymmetry is also reflected in the simulated *J-V* data where the voltages in the forward bias are much larger than those calculated in the reverse

direction. For example, the voltage values at 100 A/cm^2 are significantly larger (1.2 V and 2.6 V for 15 nm and 30 nm InGaN DH layers in 1D case, respectively) compared to those calculated at -100 A/cm^2 (~ 0.2 V for both 15 nm and 30 nm DH InGaN layers in 1D case), due to the asymmetry in the valence band diagrams (Figure 16 (a)). In addition, the voltage drop for the 3D simulation is much lower compared to that of the 1D simulation, due to the percolative pathways associated with natural alloy fluctuations in the InGaN alloys. These percolative pathways form due to the random distribution of the two constituents in the alloys which, because of their different band gaps, produces a corresponding random energy distribution in the band energies. Thus, the holes can traverse through the regions of low energies. The voltage values for the 3D simulations are almost negligible at -100 A/cm^2 for both barrier thicknesses, whereas the voltage at +100 A/cm^2 were at 0.05 V and 0.1 V for the 15 nm and 30 nm InGaN layers, respectively.

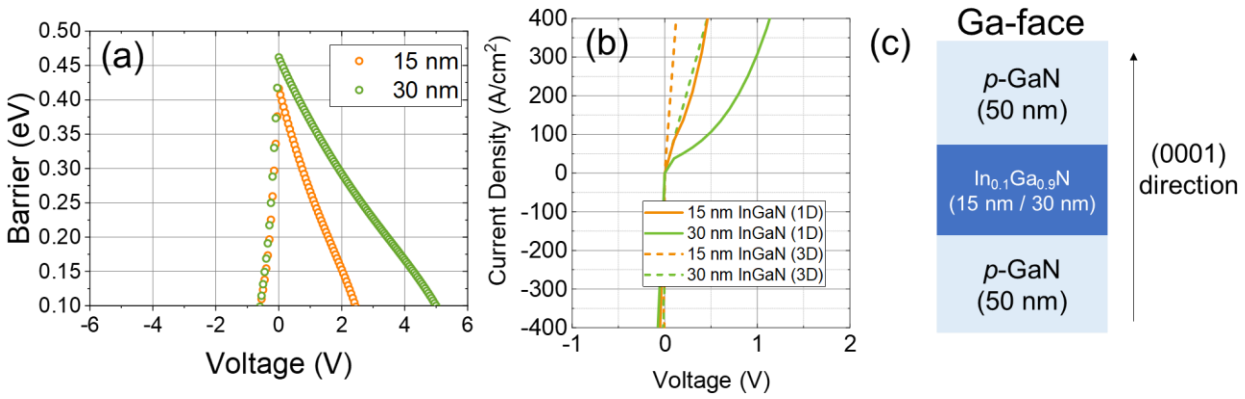

Figure 17. (a) Estimated barrier height versus applied bias voltage to the structure for 15 nm InGaN DH. The data shows that the barrier height is lower in reverse compared to forward bias. (b) Comparison of simulated *J-V* results for 1D and 3D models for 15 and 30 nm-thick InGaN DH layers. (c) Schematic of the simulated structures.

In addition to the InGaN DH structures, a similar analysis was conducted on single 5 nm and 3 × 5 nm multi-QW (MQW) structures with the same composition of Indium (~ 0.1) (Figures **Figure 17Figure 18**). In contrast to the InGaN DH layers, the MQW structure showed a more

symmetric barrier height in forward and reverse biases compared to the InGaN DHs, which is also reflected in the *J-V* simulations and the barrier height analysis (Figures 5(a) and 5(b)). The maximum calculated barrier heights for the SQW and MQW structures were 0.35 eV and 0.50 eV, respectively. According to the *J-V* results, the MQW structure show an increased voltage penalty compared to the SQW structure in both forward and reverse biases. Furthermore, the difference between the 1D and 3D J-V simulation results are much more significant for the case of SQW compared to the MQW case. The results suggest that the hole transport is significantly hindered by the polarization barrier between the InGaN QW and GaN quantum barrier (QB) for the MQW structure. On the other hand, in the case of the SQW structure, the polarization barrier is less pronounced and so the presence of percolative pathways for the holes will result in significantly higher *J* at a given bias for 3D model compared to the 1D case without alloy disorder.

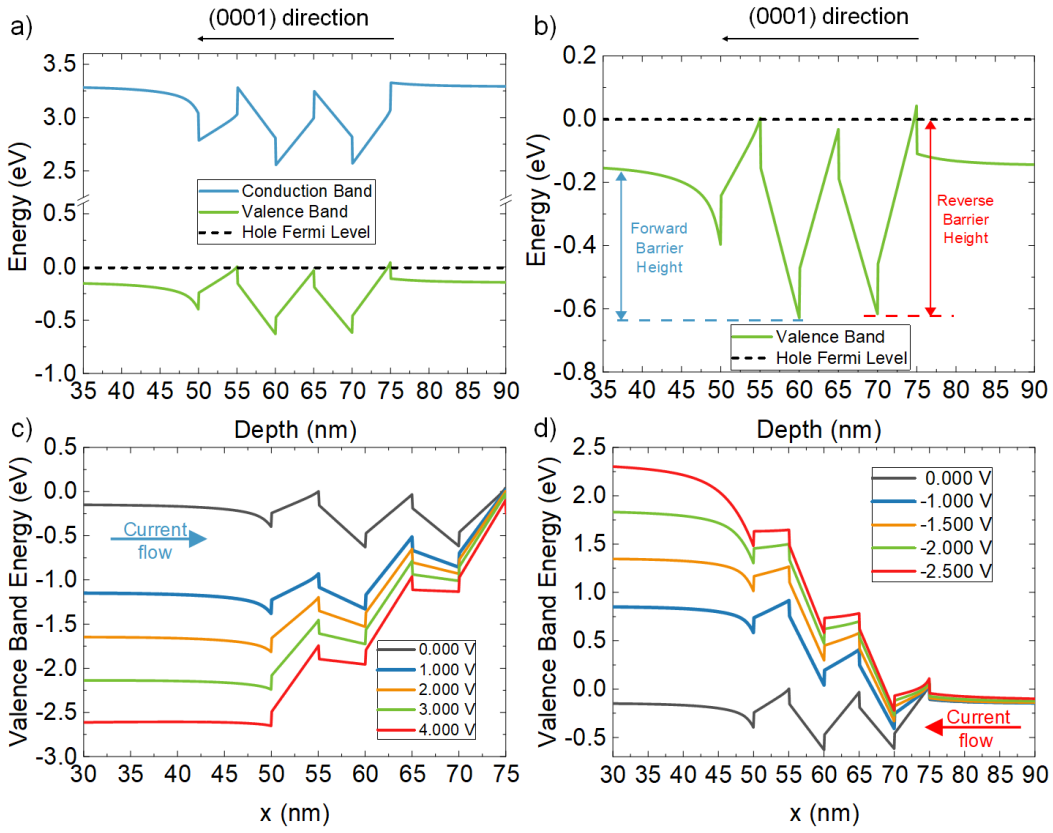

Figure 18. (a) Full band diagram for 3 × 5 nm QW structure. Valence band diagrams for p-type unipolar structures with 3 × 5 nm MQWs at (b) zero, (c) reverse and (d) forward bias.

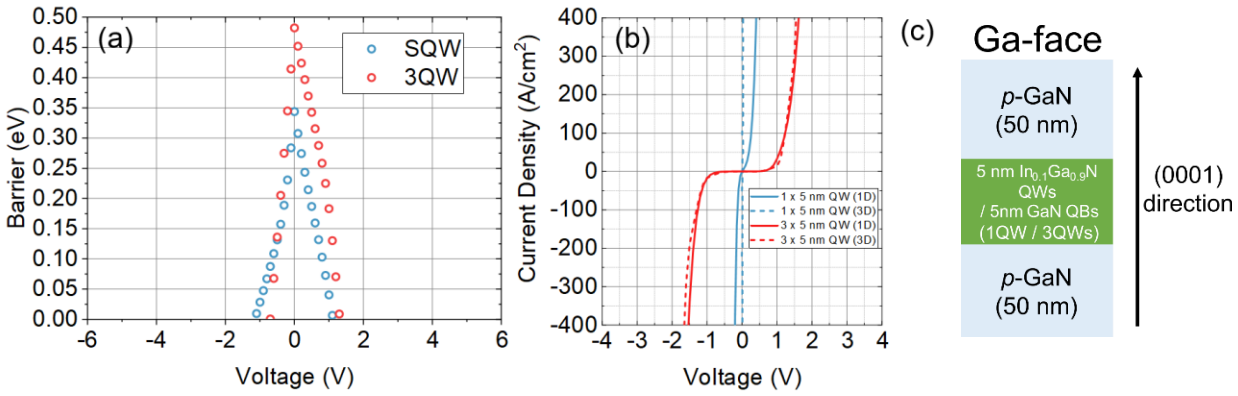

Figure 19: (a) Estimated barrier heights vs applied bias to the MQW structure. Data shows that the barrier height is lower in reverse compared to forward bias. (b) Comparison of 1D and 3D simulated *J-V* results for SQW and MQW structures. (c) Schematic of the simulated structures.

IV. Experimental Procedure

To experimentally verify the observed simulation results, unipolar hole transport structures with similar InGaN DH and QW structures were grown. Each structure consists of a unipolar *p*-type InGaN heterostructure on top of an *n*-to-*p* TJ. All structures were grown by NH_3-MBE on a Veeco Gen 930 on 1 cm^2 MOCVD-grown GaN/Sapphire templates from Lumilog Saint-Gobain. Prior to growth, a Ti/Pd/Ti (50/500/100 nm) metal stack was deposited on the back of the samples to improve heat conduction from the heating filament to the substrates and to monitor surface temperature more accurately via an optical pyrometer. The samples were then cleaned using standard solvent cleaning procedures, which is immersing them in acetone, methanol, and isopropanol successively under sonication. The samples were then loaded into the system and baked at 400ºC for an hour. Dual filament effusion cells were used to supply elemental Ga and In for GaN and InGaN growth and for Mg and Si dopants for *p*-type and *n*-type doping, respectively. A showerhead injector was used to supply NH_3, which provides the elemental N for growth. All growths were conducted under a 200 sccm NH_3 flow rate and a reactor pressure of 1×10^{-5} Torr. The growth structures consist of the following layers: first, a ~ 200 nm-thick *n*+ GaN contact layer ([Si]: 5×10^{19} cm^{-3}) was grown between two layers of 150 nm *n*-GaN ([Si]: 5×10^{19} cm^{-3}) at a substrate temperature of ~ 820 ºC. Then, an *n*-to-*p* TJ was grown with a highly doped *p*++ ([Mg]: 5×10^{20} cm^{-3})-*n*++([Si]: 5×10^{20} cm^{-3}) (10 nm/ 10 nm) design. The unipolar heterostructure were then separately grown, consisting of unintentionally doped (UID) InGaN DH or QW layers sandwiched between two 50 nm-thick *p*-GaN ([Mg]: 5×10^{19} cm^{-3}) layers at a 750 °C substrate temperature. The following structures were grown: Sample A with no InGaN as a reference, Sample B with a 15 nm UID $In_{0.1}Ga_{0.9}N$ DH layer, Sample C with a 30 nm UID $In_{0.1}Ga_{0.9}N$ DH layer, Sample D with 1 × 5 nm UID $In_{0.1}Ga_{0.9}N$ (SQW) and Sample E with 3 × 5 nm UID $In_{0.1}Ga_{0.9}N$ (MQW). In our previous investigation [15], we concluded that having a UID GaN as the barrier layer does not

provide any significantly barrier to the hole transport, so we excluded that particular structure here in this investigation. Finally, the samples are capped with a 10 nm-thick p++ GaN ([Mg] : 3×10^{20}) contact layer. Thickness and composition calibrations were conducted on separately grown calibration structures using high-resolution x-ray diffraction (HRXRD) while doping calibrations were conducted using secondary-ions mass spectroscopy (SIMS) on separately grown calibration samples.

The samples were then fabricated into standard mesa isolated devices with circular patterns. First, an SiO_2 layer (~300 nm) was deposited using plasma-enhanced chemical vapor deposition (PECVD) to protect the *p*++ GaN contact layers during the nanofabrication process. The mesas were then formed using self-aligned wet etching of SiO_2 with buffered hydrofluoric acid (BHF) followed by a 400 nm dry-etch using a reactive-ion etching (RIE) system. After that, another SiO_2 layer was deposited by electron-beam (E-beam) deposition for the *n*- and *p*- contacts. The circular metal contacts that were deposited on the mesa had diameters of 50 µm, 75 µm, 100 µm, 125 µm, 150 µm, 175 µm and 200 µm. Finally, a probe station with tungsten probes connected to a Keithley 4200A-SCS Parameter Analyzer was used to measure the electrical characteristics of our structures. Since the vertical distance of the *p*-region is much smaller than the lateral dimensions, there should be little to no current crowding on the mesa sidewalls and the current should be spread evenly through the mesas. Therefore, the current density, *J* is simply the injected current divided by the area of the *p*-contacts.

V. Experimental Results and Discussion

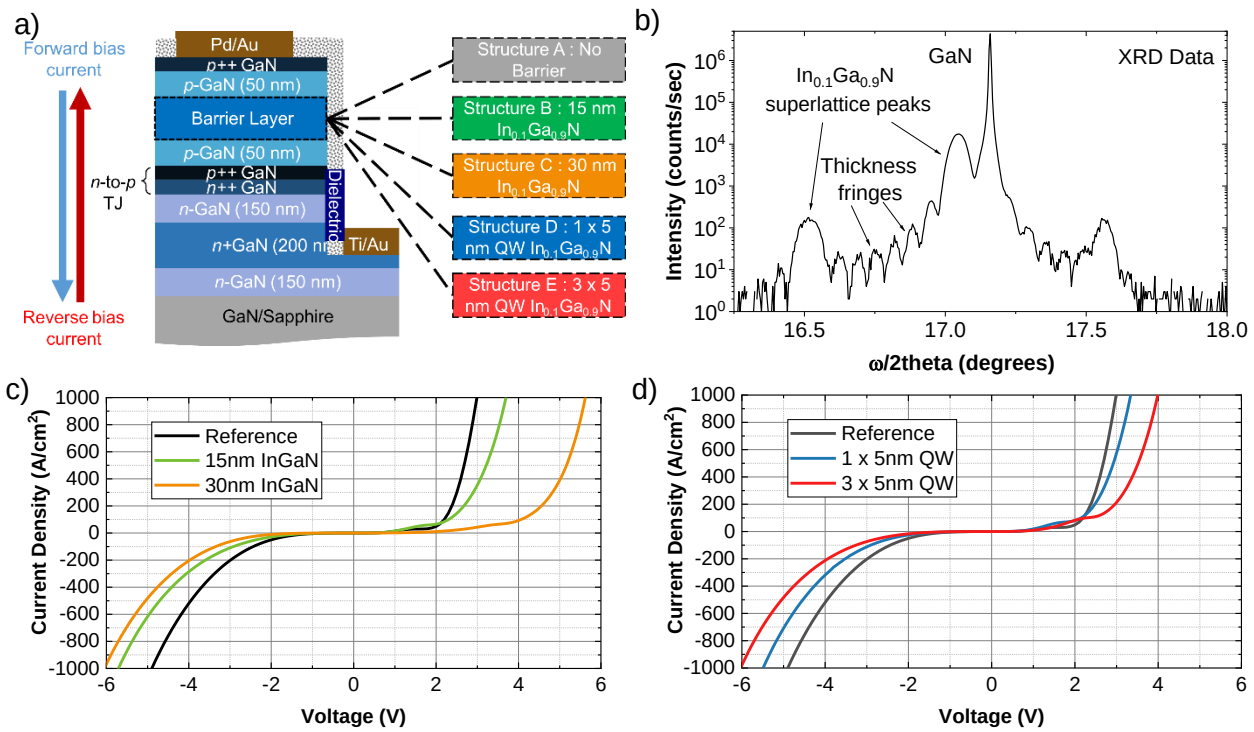

Figure 20: (a) Schematic of all the structures grown and fabricated in this study. (b) HRXRD data of the calibration structure used for the $In_{0.1}Ga_{0.9}N$ structure. (c) Experimental *J-V* plots for the InGaN DH series. (d) Experimental *J-V* plots for the QW series. (c) and (d) shows the *J-V* data for all the samples.

Strong correlations can be drawn between experimental and computational data (**Figure 20**). First, there is a larger voltage drop for the 30 nm-thick vs 15 nm-thick InGaN DH layers. For the QW series, the trend is confirmed; the MQW structure shows a larger voltage drop compared to the SQW structure. Furthermore, the voltage drop in the forward-bias is larger than in the reverse for the InGaN DH *J-V* data, particularly in the case of the thicker 30 nm InGaN structure, where the voltage penalty was 2.25 V at 500 A/cm^2 compared to 1.25 V at -500 A/cm^2. The experimental data also confirms that in the case of the QW structures, the voltage penalty is more symmetric (~0.75 V at 500 A/cm^2 and ~ 1.0 V at -500 A/cm^2 for the MQW structure) compared to the InGaN DH series (~2.5 V at 500 A/cm^2 and ~ 1.0 V at -500 A/cm^2 for the 30 nm-thick InGaN DHs). At the low-voltage regime, the voltages are slightly higher in the reference sample compared to the transport structures, which is likely due to some variations between the samples in terms of contact

resistivity and the doping in the TJs which could result in slight variations in the *J-V* characteristics. We have also conducted a perimeter-to-area ratio analysis to determine the effect of sidewall leakage on the overall current density in our experimental results. The analysis is detailed in the supplemental materials section of the paper.

The voltages on all the structures are larger than those from the simulations, potentially due to the voltage penalty associated with the TJs and the contacts, which are not included in the simulations. Despite the inconsistency in the actual values of the voltages, the experimental results agree with the trend shown in our simulations as adding the thickness and the number of quantum wells does produce a larger barrier to hole transport. A significant factor that leads to the discrepancy is the inability of our models to account for tunneling behavior. Hence, we only consider transport through *p-i-p* layers, leading to a smaller voltage drop. Most TJ models today rely on the Wentzel-Kramer-Brillouin (WKB) approximation [14], which is insufficient when accounting for tail states. In addition, most models today focus on the weak forward bias regime that was developed for narrow-bandgap semiconductors such as Si and GaAs [27,28]. For wide bandgap semiconductors such as GaN, the situation is more complicated due to the existence of the various defect states within the bandgap and the tail states. A consistent approach toward modeling the TJs is a subject of our other investigations which will be published elsewhere.

Upon further inspection of the data, it is concluded that there is a dependence of the current density, J on the device perimeter. The analysis was done using

$$I_{measured} = Area * J_{bulk} + Perimeter * J_{perimeter}.$$

Upon rearranging the terms, we obtain

$$J_{measured} = \frac{Perimeter}{Area} * J_{perimeter} + J_{bulk}.$$

Thus, the measured current density (Figure 21) at a given voltage for the different mesa sizes (*i.e.* their corresponding perimeter to area ratio) were plotted, as shown in Fig. 9. The data is also fitted linearly to obtain both the perimeter-dependent *J* from the slope as well as the corresponding bulk *J* from the *y*-intercept, which represents the true *J*-*V* characteristic, independent of the mesa size. The contribution of the perimeter term of *J*, $J_{perimeter}$ to the overall measured *J* obtained by dividing $J_{perimeter}$ by $J_{measured}$ for the device of size 200 μm was also plotted and shown in Fig. 10(a).

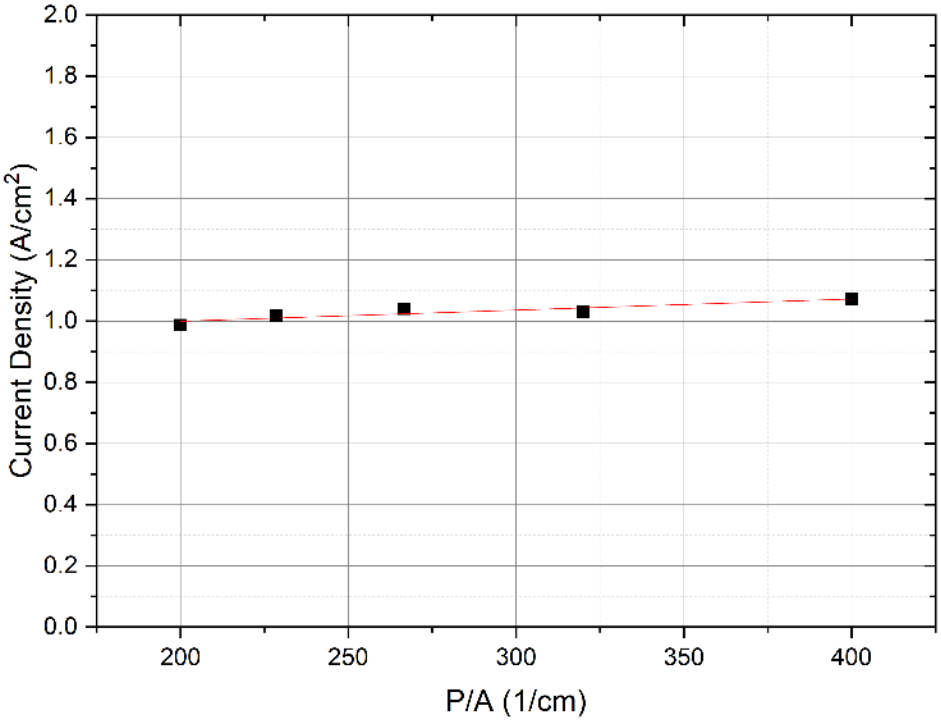

Figure 21: Measured *J* as a function of Perimeter/Area ratio (*P/A*). The dashed red line indicates a linear fitting of the data.

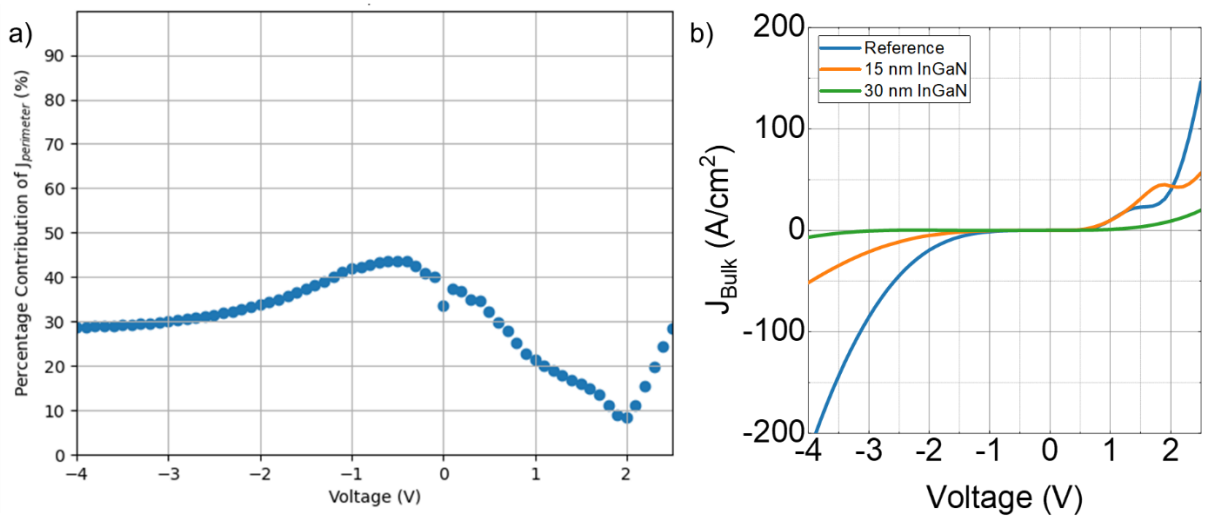

Figure 22: (a) Percentage contribution of $J_{perimeter}$ on the overall current density for a 200 µm device. (b) Corrected *J-V* plots for the reference, 15 nm InGaN and 30 nm InGaN samples, taking into account J_{Bulk}, instead of $J_{Measured}$

As shown in the plot above for the 200 µm device, ~40% of the current is from the outer section of the device. We attributed this to ion etch damage that must have seeped into the tunnel junction whilst processing the sample into devices. However, a plot of the bulk current density, J_{bulk} shows that that the trend does exist and that InGaN acts a barrier to hole transport.

VI. Conclusion

In conclusion, we investigated hole transport within InGaN alloys in *p*-type unipolar heterostructures through modeling and experimentation. Even a layer as thin as 5 nm of $In_{0.1}Ga_{0.9}N$ was sufficient to act as a barrier to hole transport in both reverse and forward bias. It was also found that, through the comparison of 1D and 3D simulations, percolative transport plays a larger role for the InGaN DH devices compared to the 3QW devices. This is believed to be due to the polarization discontinuity between the GaN layers and the InGaN QW layers, which hinder the transport of holes through the QW region. These findings will be important in our understanding of hole transport physics within GaN optoelectronics. Our results cement the effectiveness of unipolar hole transport structures, which are enabled by *n*-to-*p* TJs, as test vehicles for determining the barriers to hole transport. By decoupling recombination from the transport behavior, we can

determine the validity of our simulations without the complexities of recombination, which remains a challenge to simulate due to variation in recombination models.

VII. Acknowledgements

This work was supported by Collaborative Research in Engineering, Science and Technology (CREST), the Simons Foundation (Grant No. 601952, JS), Air Force Office of Scientific Research (Program No. FA9550-19-1-10090), National Science Foundation (NSF) RAISE program (Grant No. A007231601), Sandia National Laboratory (Award # 2150283), and Ministry of Science and Technology, Taiwan (Grant No. MOST 108-2628-E-002-010-MY3 and MOST 110-2923-E-002 - 002). A portion of this work was performed at the UCSB CNSI-Nanofabrication facility .

VIII. References

[1] S. Nakamura, M. Senoh, S. Nagahama, N. Iwasa, T. Yamada, T. Matsushita, H. Kiyoku, and Y. Sugimoto, *InGaN-Based Multi-Quantum-Well-Structure Laser Diodes,* Japanese Journal of Applied Physics **35**, L74 (1996).

[2] J. Hager, M. Seitz, C. Bemmer, P. Jahn, P. Ansorg, O. Woisetschläger, F. Buchmann, D. Sprenger, M. Vogl, O. Hering, J. Artzner, M. Glück, B. Reisinger, T. Mitterlehner, P. Schantl, L. Weber, S. Berlitz, C. Neumann , *Handling 17W of Scanning Laser Power Three Years of Exploration in the ILaS Project*, in *Proceedings of the 12th International Symposium on Automotive Lightning* (2017).

[3] S. P. DenBaars, D. Feezell, K. Kelchner, S. Pimputkar, C.-C. Pan, C.-C. Yen, S. Tanaka, Y. Zhao, N. Pfaff, R. Farrell, M. Iza, S. Keller, U. Mishra, J. S. Speck, and S. Nakamura, *Development of Gallium-Nitride-Based Light-Emitting Diodes (LEDs) and Laser Diodes for Energy-Efficient Lighting and Displays*, Acta Materialia **61**, 945 (2013).

[4] S. Watson, S. Gwyn, S. Viola, G. Giuliano, T. J. Slight, S. Stanczyk, S. Grzanka, A. Yadav, D. Rowe, L. Laycock, K. E. Docherty, E. Rafailov, P. Perlin, S. Najda, M. Leszczynski, and A. E. Kelly, *InGaN/GaN Laser Diodes and Their Applications*, in *2018 20th International Conference on Transparent Optical Networks (ICTON)* (2018), pp. 1–4.

[5] S. Nakamura, M. Senoh, N. Iwasa, and S. Nagahama, *High-Brightness InGaN Blue, Green and Yellow Light-Emitting Diodes with Quantum Well Structures*, Japanese Journal of Applied Physics **34**, L797 (1995).

[6] D. Feezell and S. Nakamura, *Invention, Development, and Status of the Blue Light-Emitting Diode, the Enabler of Solid-State Lighting*, Comptes Rendus Physique **19**, 113 (2018).

[7] M. Nami, A. Rashidi, M. Monavarian, S. Mishkat-Ul-Masabih, Ashwin. K. Rishinaramangalam, S. R. J. Brueck, and D. Feezell, *Electrically Injected GHz-Class GaN/InGaN Core–Shell Nanowire-Based MLEDs: Carrier Dynamics and Nanoscale Homogeneity*, ACS Photonics **6**, 1618 (2019).

[8] M. Monavarian, A. Rashidi, and D. Feezell, *A Decade of Nonpolar and Semipolar III-Nitrides: A Review of Successes and Challenges*, Physica Status Solidi (a) **216**, 1800628 (2019).
[9] S. Rajbhandari, J. J. D. McKendry, J. Herrnsdorf, H. Chun, G. Faulkner, Harald Haas, I. M. Watson, D. O'Brien, and M. D. Dawson, *A Review of Gallium Nitride LEDs for Multi-Gigabit-per-Second Visible Light Data Communications*, Semicond. Sci. Technol. **32**, 023001 (2017).
[10] J. Wu, W. Walukiewicz, K. M. Yu, W. Shan, J. W. Ager, E. E. Haller, H. Lu, W. J. Schaff, W. K. Metzger, and S. Kurtz, *Superior Radiation Resistance of In1−xGaxN Alloys: Full-Solar-Spectrum Photovoltaic Material System*, Journal of Applied Physics **94**, 6477 (2003).
[11] Y. D. Jhou, C. H. Chen, R. W. Chuang, S. J. Chang, Y. K. Su, P. C. Chang, P. C. Chen, H. Hung, S. M. Wang, and C. L. Yu, *Nitride-Based Light Emitting Diode and Photodetector Dual Function Devices with InGaN/GaN Multiple Quantum Well Structures*, Solid-State Electronics **49**, 1347 (2005).
[12] D. A. Browne, B. Mazumder, Y. Wu, and J. S. Speck, *Electron Transport in Unipolar InGaN / GaN Multiple Quantum Well Structures Grown by NH 3 Molecular Beam Epitaxy*, **185703**, (2015).
[13] F. Bernardini, V. Fiorentini, and D. Vanderbilt, *Spontaneous Polarization and Piezoelectric Constants of III-V Nitrides*, Phys. Rev. B **56**, R10024 (1997).
[14] S. Krishnamoorthy, D. N. Nath, F. Akyol, P. S. Park, M. Esposto, and S. Rajan, *Polarization-Engineered GaN/InGaN/GaN Tunnel Diodes*, Applied Physics Letters **97**, 203502 (2010).
[15] K. S. Qwah, M. Monavarian, G. Lheureux, J. Wang, Y.-R. Wu, and J. S. Speck, *Theoretical and Experimental Investigations of Vertical Hole Transport through Unipolar AlGaN Structures: Impacts of Random Alloy Disorder*, Applied Physics Letters **117**, 022107 (2020).
[16] X. A. Cao, H. Cho, S. J. Pearton, G. T. Dang, A. P. Zhang, F. Ren, R. J. Shul, L. Zhang, R. Hickman, and J. M. Van Hove, *Depth and Thermal Stability of Dry Etch Damage in GaN Schottky Diodes*, Applied Physics Letters **75**, 232 (1999).
[17] D. W. Jenkins and J. D. Dow, *Electronic Structures and Doping of InN, InxGa1-XN, and InxAl1-XN*, Phys. Rev. B **39**, 3317 (1989).
[18] C. K. Li, M. Piccardo, L. S. Lu, S. Mayboroda, L. Martinelli, J. Peretti, J. S. Speck, C. Weisbuch, M. Filoche, and Y. R. Wu, *Localization Landscape Theory of Disorder in Semiconductors. III. Application to Carrier Transport and Recombination in Light Emitting Diodes*, Physical Review B **95**, 1 (2017).
[19] H.-H. Chen, J. S. Speck, C. Weisbuch, and Y.-R. Wu, *Three Dimensional Simulation on the Transport and Quantum Efficiency of UVC-LEDs with Random Alloy Fluctuations*, Applied Physics Letters **113**, 153504 (2018).
[20] M. Filoche and S. Mayboroda, *Universal Mechanism for Anderson and Weak Localization*, Proceedings of the National Academy of Sciences **109**, 14761 (2012).
[21] H. K. Gummel, *A Self-Consistent Iterative Scheme for One-Dimensional Steady State Transistor Calculations*, IEEE Transactions on Electron Devices **11**, 455 (1964).
[22] D. N. Arnold, G. David, D. Jerison, S. Mayboroda, and M. Filoche, *Effective Confining Potential of Quantum States in Disordered Media*, Phys. Rev. Lett. **116**, 056602 (2016).

[23] T.-J. Yang, R. Shivaraman, J. S. Speck, and Y.-R. Wu, *The Influence of Random Indium Alloy Fluctuations in Indium Gallium Nitride Quantum Wells on the Device Behavior*, Journal of Applied Physics **116**, 113104 (2014).
[24] I. Vurgaftman, J. R. Meyer, and L. R. Ram-Mohan, *Band Parameters for III–V Compound Semiconductors and Their Alloys*, Journal of Applied Physics **89**, 5815 (2001).
[25] J. Piprek, *Nitride Semiconductor Devices: Principles and Simulation* (Wiley, 2007).
[26] A. E. Romanov, T. J. Baker, S. Nakamura, and J. S. Speck, *Strain-Induced Polarization in Wurtzite III-Nitride Semipolar Layers*, Journal of Applied Physics **100**, 023522 (2006).
[27] N. Moulin, M. Amara, F. Mandorlo, and M. Lemiti, *Tunnel Junction I(V) Characteristics: Review and a New Model for p-n Homojunctions*, Journal of Applied Physics **126**, 033105 (2019).
[28] M. Hermle, G. Létay, S. P. Philipps, and A. W. Bett, *Numerical Simulation of Tunnel Diodes for Multi-Junction Solar Cells*, Progress in Photovoltaics: Research and Applications **16**, 409 (2008).
[29] See Supplemental Material at [URL] for the design of the mask used for lithography

Chapter 3 : Modeling Dislocation-Related Leakage in GaN p-n Diodes

3.1 Forward-Bias

I. Introduction

III-N semiconductors have been widely used in high-speed transistors[1–5], visible and ultraviolet (UV) optoelectronics[6–12], and vertical power electronics[13–17]. The high theoretical breakdown field (~3.3 MV/cm) and carrier mobility (>1,000 cm^2/V-s) have garnered interest in the field of power electronics where energy efficiency and high voltage operation are necessary. Vertical device topologies are useful for reducing the wafer footprint of power electronics by allowing voltage to be held across epitaxially grown interfaces rather than lateral ones. One of the major challenges to the performance of GaN vertical power devices has been the ubiquitous presence of threading dislocations (TDs) in the substrates for epitaxial growth. TDs have been repeatedly shown to exacerbate catastrophic and non-catastrophic breakdown in vertical GaN devices[16,18,19], but the mechanisms by which this occurs has been hitherto unstudied despite being experimentally observed.

The dislocation structure in GaN has been extensively studied by high-resolution x-ray diffraction (HRXRD) and transmission electron microscopy (TEM). Edge and mixed-type threading dislocations have been shown to be much more prevalent than their screw-type counterparts, but they all have a line vector within ~10° of the <0001> direction regardless of their Burger's vector, $\vec{\boldsymbol{b}}$ [20,21]. Furthermore, the electrical nature of TD trap states in n-GaN has been shown to be a deep acceptor in the band gap with a line density of approximately one electron trap state per c-lattice translation[22,23]. It has also been observed that this trap state density associated with TDs results in a screening region around the dislocation as the donors interact with the trap states to create regions of significant net charge. In a simple picture, the occupied dislocation-related acceptors in n-type material are screened by ionized donors as shown in Figure 38. Similarly, we assume that dislocation-related donors are screened by ionized acceptors in p-type material.

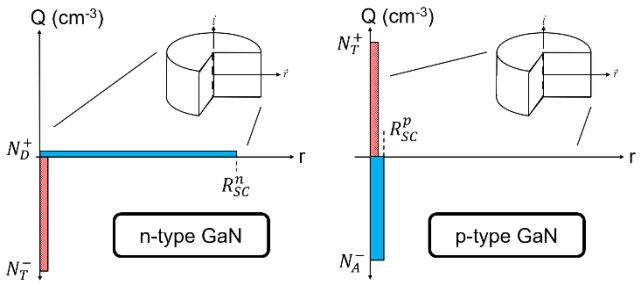

Figure 23: Simplified representation of screening regions around a dislocation in a lightly doped (N_D= 5×10^{17} cm^{-3}) n-type (left) and heavily doped (N_A= 5×10^{19} cm^{-3}) p-type (right) GaN. Note that the charge region around the dislocation in p-type GaN is much smaller than in n-type GaN due to the high doping required to produce p-type conductivity being on the order of the density of trap states. Note that N_D^+ and N_A^- are the ionized donor and acceptor concentrations, respectively, N_T^- and N_T^+ are the ionized negative and positive trap state concentrations, respectively, and R_{SC}^n and R_{SC}^p are the screening regions in the n- and p-type regions, respectively.

In the simplest treatment, the dislocation and space charge regions are cylindrical with constant trap state and dopant density (Figure 38). The screening radius can be simply calculated using Charge Neutrality and results in

$$R_{SC} = \sqrt{\frac{\rho_n}{\pi c}} * \sqrt{\frac{1}{N}} \qquad (3)$$

where ρ_n is the number of trap states per c-lattice translation, c is the c-lattice constant, and N is the uniform dopant concentration of the semiconductor. This ionization and screening of the cylindrical area of the TD line distorts the energy band profiles around the dislocation with potentials of ~2.5 V as observed by electron holography in n-GaN[24]. This behavior has been attributed to the coalescence of defects around the TD core as suggested by Arslan and Browning[25] and observed by Müller et al.[26]. The trap state energy associated with such a band bending closely matches an electron trap state ~1.0 eV above the valence band maximum found in DLTS measurements[22]; additionally, the trap state density are consistent with previous experimental and theoretical values of approximately one electron trap state per c-lattice translation[27]. From these experimental observations and theoretical predictions, it is possible to construct an accurate band structure model of n-type GaN pierced by a TD.

In contrast, a band structure model of p-type GaN that includes the treatment of TD trap states has been substantially more elusive. Electron holography analyses have found regions of negative space charge that is likely associated with screening acceptors around a donor trap states coalescing near TDs in p-GaN[24]. However, the high acceptor concentration needed to form achieve measurable hole conductivity results in a screening region that is beyond the resolution the holography method is likely able to measure accurately (~2 nm). Thus, the nature of the TD charge behavior in p-GaN remains experimentally unobserved. However, in our previous work, TDs in p-GaN act as nonradiative centers similar to n-GaN as shown by cathodoluminescence (CL) results[28], thus we assume that the TD trap states behave similarly in p- and n-type GaN.

These analyses indicate that in the unipolar bulk regions threading dislocations can be accurately described as a distribution of compensating trap states in the crystal along the TD line, but the interactions of the distortions in the band profiles of unipolar materials at a bipolar junction presents an interesting physical problem that has now been modeled. In this study, a physical model is presented to treat a vertical GaN pn junction with a TD puncturing junction. Energy band, electric field, and current flow diagrams are presented along with other plots of merit, and the mechanisms therein are discussed.

II. Model

In Appendix A, all relevant variables are given in alphabetical order to assist in understanding the parameters and models used in this work.

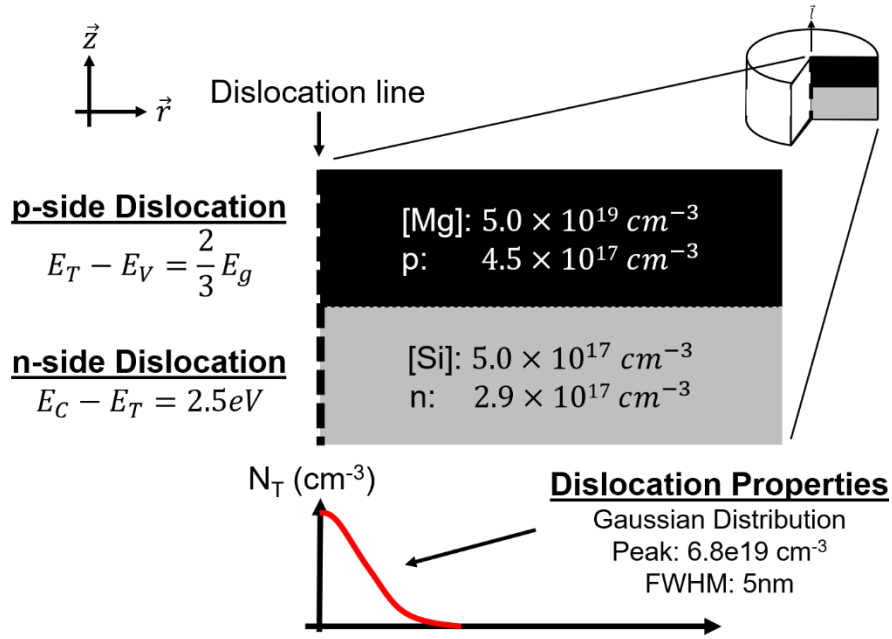

n-type GaN		
σ_n	10^{-12}	cm^2
τ_p	148	fs
L_T^{hole}	3.2	nm
p-type GaN		
σ_p	10^{-12}	cm^2
τ_n	56	fs
L_T^{elec}	2.2	nm

Figure 24: A cylindrically symmetric pn diode is modeled for this study with a Gaussian distribution of deep trap states used to represent the TD-associated traps. Typical doping densities for the p- and n-type regions are used, and experimentally standard hole and electron concentrations are observed in the model. The location of the trap state energy within the n-type region was based on experimental results while the p-type region was placed arbitrarily deep in the energy gap. In the right table, values for trap capture cross section (σ), minority carrier lifetime (τ), and minority carrier diffusion length (L_T) are given for the trap state region associated with the TD line. These values were chosen such that these model variables all matched experimental values as closely as possible.

In this study, Silvaco's ATLAS modeling software was used to solve for the 2D pn junction model shown in Figure 39. Cylindrical coordinates were used to simplify the computational requirements by utilizing the six-fold rotational symmetry of the 3D crystal structure about the TD line vector, <0001>, without resorting to a full 3D treatment. N_A and N_D values are chosen based on experimentally typical values for vertical GaN pn junctions doped with Mg and Si, respectively. The model r-dimension limit of 564 nm approximates a 10^8 cm^{-2} TD density as is typical in commercially available GaN growth on either Al_2O_3 or SiC. Our TD-associated trap state region was treated as a Gaussian distribution with FWHM of 5 nm and a peak trap state density of 6.84×10^{19} cm^{-3}. This is a close approximation of experimental observations of edge and mixed-type dislocations with coalesced charged defects[29,30] around an electrically inactive core as shown by Muller et al[26] and proposed by Arslan and Browning[25], however it should be noted that pure screw-type dislocations show substantially different charge profiles[24] and leakage

characteristics[31] that are not modeled in this work. The distribution used approximates a one electron per c-lattice translation when normalized in the z-direction. Trap energy levels within the bandgap were E_C – 2.5 eV and E_V + 2.3 eV for n- and p-type GaN, respectively. Although the energy level of the dislocation trap state in n-GaN is well-documented, the level for p-GaN is approximated as an arbitrarily deep donor state. This assumption will be discussed later.

The trap state properties are also chosen such that the minority carrier diffusion lengths and lifetimes match those given in the literature. Using the approximation of a $10^{16}\ cm^{-3}$ trap state density in the bulk away from the dislocation, a capture cross section for both electrons and holes of $10^{-12}\ cm^2$ was chosen based on the following equations:

$$\tau = (\rho_T * \sigma * \nu)^{-1} \tag{5}$$

$$\mathrm{L_T} = \sqrt{\frac{kT}{q} * \mu * \tau}, \tag{6}$$

where τ is the minority carrier lifetime; ρ_T is the local trap concentration; σ is the trap minority carrier capture cross section; ν is the minority carrier thermal velocity; L_T is the minority carrier diffusion length; and μ is the minority carrier mobility. These values resulted in a lifetimes and transfer lengths given in Table 9 using the minority carrier mobilities found by Kumakura et al.[30]. The bulk values for ρ_T approximate experimental observations[23,27,33], and the lifetimes given in this table are within the expected range for minority carrier diffusion length and lifetime[30–33] and were observed in our diode model with no dislocation.

	$\rho_T\ (cm^{-3})$	τ_n	$L_T^n\ (nm)$	τ_p	$L_T^p\ (nm)$
TD core	6.84×10^{19}	56 fs	2.1	148 fs	3.2
Bulk	10^{16}	0.38 ns	178	1.01 ns	261

Table 7: Minority carrier lifetimes and diffusion lengths for different trap state conditions. The bulk lifetimes are within experimental parameters for minority carrier lifetimes[30].

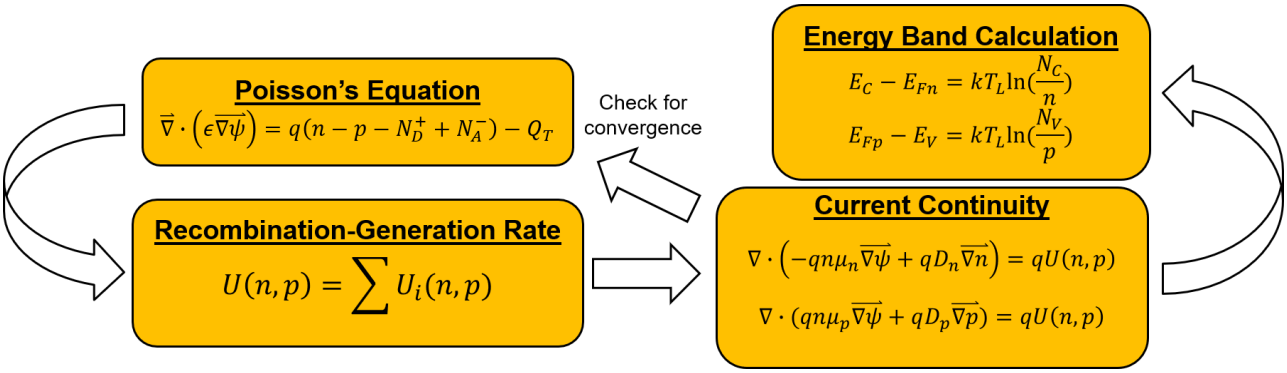

Figure 25. Process overview the Gummel method which was used extensively for modeling dislocation behavior; however, the Newton-Raphson methodology was used if convergence was not achieved.

Using this physical model, the Poisson and steady-state Current Continuity equations are solved on the mesh self-consistently using the Gummel method (Figure 40).

$$\vec{\nabla} \cdot \left(\epsilon \vec{\nabla} \psi\right) = q(n - p - N_D^+ + N_A^-) - Q_T \tag{7}$$

$$\nabla \cdot \overrightarrow{J_n} = -qU(n,p) \tag{8}$$

$$\nabla \cdot \overrightarrow{J_p} = qU(n,p) \tag{9}$$

In the Poisson equation (27), ψ is the electric potential; n and p are the electron and hole concentration; N_D^+ and N_A^- are the ionized donor and acceptor concentrations. In the Current continuity equations, $\overrightarrow{J_n}$ and $\overrightarrow{J_p}$ are the electron and hole current densities, and $U(n, p)$ is the net recombination-generation rate. If convergence is not achieved, the solver will switch from the Gummel to the Newton-Raphson method to solve the system of equations.

In addition to these core equations, additional models are necessary to include the various behaviors of the GaN material systems and trap physics. These are discussed below.

Incomplete Ionization Model

It has been well-documented experimentally that Mg_{Ga} has an activation energy around 190 meV[34], thus to accurately model p-GaN, we utilized the incomplete ionization model[38] to account for the thermal activation of both the donors and acceptors in GaN.

$$N_D^+ = \frac{N_D}{1 + g_n exp\left(\frac{E_{Fn} - (E_C - E_D)}{kT}\right)} \tag{10}$$

$$N_A^- = \frac{N_A}{1 + g_p \exp\left(\frac{(E_A - E_V) - E_{Fp}}{kT}\right)}, \tag{11}$$

where N_D^+ and N_A^- are the ionized donor and acceptor concentrations; N_D and N_A are the donor and acceptor concentrations; g_n and g_p are the conduction and valence band degeneracies; E_{Fn} and E_{Fp} are the electron and hole quasi-Fermi levels; $(E_C - E_D)$ and $(E_A - E_V)$ are the donor and acceptor activation energies. This model predicts that only ~1% of the Mg acceptor dopants will contribute holes to the GaN semiconductor while ~60% of the Si donors will contribute electrons. Furthermore, unintentionally-doped GaN is usually slightly n- due to the unintentional doping by oxygen. This combined with the low activation efficiency necessitate high Mg concentrations to achieve p-type GaN experimentally.

Our model makes two basic doping assumptions. Firstly, the model uses an abrupt metallurgical junction such that there is no overlap between the p- and n-type regions of the diode. Secondly, the model does not explicitly specify any compensating defects or recombination centers in the model away from the dislocation but rather combines the holistic crystal imperfections into a minority carrier lifetime within the range of values provided in the literature[30].

Shockley-Read-Hall (SRH) Trap-Assisted Recombination Model

To model the charging and screening effects around the dislocation line, a trap ionization model was implemented. The Simmons and Taylor model (based on Shockley-Read-Hall recombination

statistics)[39–41] was used to simulate the occupancy, $f(E_T)$, and charge state density of trap states, Q_T, associated with the TD line:

$$Q_T = q(N_{tD}^{+} - N_{tA}^{-}) \tag{12}$$

$$N_{tA}^{-} = \rho_T * f(E_T) \tag{13}$$

$$N_{tD}^{+} = \rho_T * (1 - f(E_T)) \tag{14}$$

$$f(E_T) = \frac{\bar{n} + e_p}{e_n + \bar{n} + \bar{p} + e_p} \tag{15}$$

$$\bar{n} = \nu_n \sigma_n n \tag{16}$$

$$\bar{p} = \nu_p \sigma_p p \tag{17}$$

$$e_p = \nu_p \sigma_p N_V \exp\left(\frac{E_V - E_T}{kT}\right) \tag{18}$$

$$e_n = \nu_n \sigma_n N_C \exp\left(\frac{E_T - E_C}{kT}\right) \tag{19}$$

In this system of equations, Q_T is the concentration of charged trap states; N_{tD}^{+} and N_{tA}^{-} are the concentration of ionized donor and acceptor trap states; ρ_T is the density of trap states, $f(E_T)$ is the Fermi occupancy function at the trap state energy level; $\bar{n}$ and $\bar{p}$ are the electron and hole capture rates; ν_n and ν_p are the thermal velocities for electrons and holes; σ_n and σ_p are the electron and hole capture cross sections; n and p are the electron and hole concentrations; e_p and e_n are the hole and electron trap emission rates; N_V and N_C are the effective density of states for the valence and conduction bands; E_V and E_C are the valence and conduction bands; and E_T is the trap state energy level. These equations tie into the previous models given in two important ways. Firstly, the electron and hole concentrations given in (36) and (37) are functions of the quasi-Fermi levels associated with the carriers. In forward bias, these quasi-Fermi levels split near the junction and would therefore change the behavior of the traps in these regions. This change carrier statistics in the regions with Fermi level splitting is considered in these two equations by the inclusion of the local

carrier concentrations which are functions of the quasi-Fermi levels. Secondly, as previously stated, the trap states are given a capture cross section such that the minority carrier lifetimes and minority diffusion lengths in the bulk associated with a lower concentration of these traps matches with previously found experimental evidence. The chosen values for capture cross section also come into effect here when calculating the carrier capture rate for trap occupancy. Additionally, in equation (32), N_{tD}^{+} and N_{tA}^{-} represent the concentration of ionized donor and acceptor trap states, respectively. In brief, the occupancy of the trap states within the semiconductor depends on the mechanistic rates at which that trap either captures or emits carriers. These rates are a function of the traps' position in the energy band as well as the local Fermi level which dictates the concentration of free carriers at that point. For the electron occupancy of traps given in Equation (35), the mechanisms that will cause that trap to be occupied by an electron are the capture rate of electrons, $\bar{n}$, and the emission rate of holes, e_p. Thus, the steady state occupancy of the trap can be described as the ratio of these occupying rates to all of the rates on that trap state.

Equation (35) expressing the occupancy of the localized trap state is simply a re-written form of the SRH recombination equation with the coefficients rewritten to more explicitly represent carrier emission and capture.

Additionally, Shockley-Read-Hall[41] recombination rates are used directly to model trap-assisted recombination rates using the following equation:

$$U_{SRH} = \frac{pn - n_i^2}{\tau_n \left[p + n_i \, exp\left(\frac{E_i - E_T}{kT}\right)\right] + \tau_p \left[n + n_i \, exp\left(\frac{E_T - E_i}{kT}\right)\right]} \qquad (20)$$

where U_{SRH} is the Shockley-Read-Hall recombination rate; p and n are the hole and electron concentrations; n_i is the intrinsic carrier concentration; τ_n and τ_p are the electron and hole lifetimes; E_i is in the intrinsic energy level; and E_T is the trap state energy level.

III. Results

Zero Bias Model

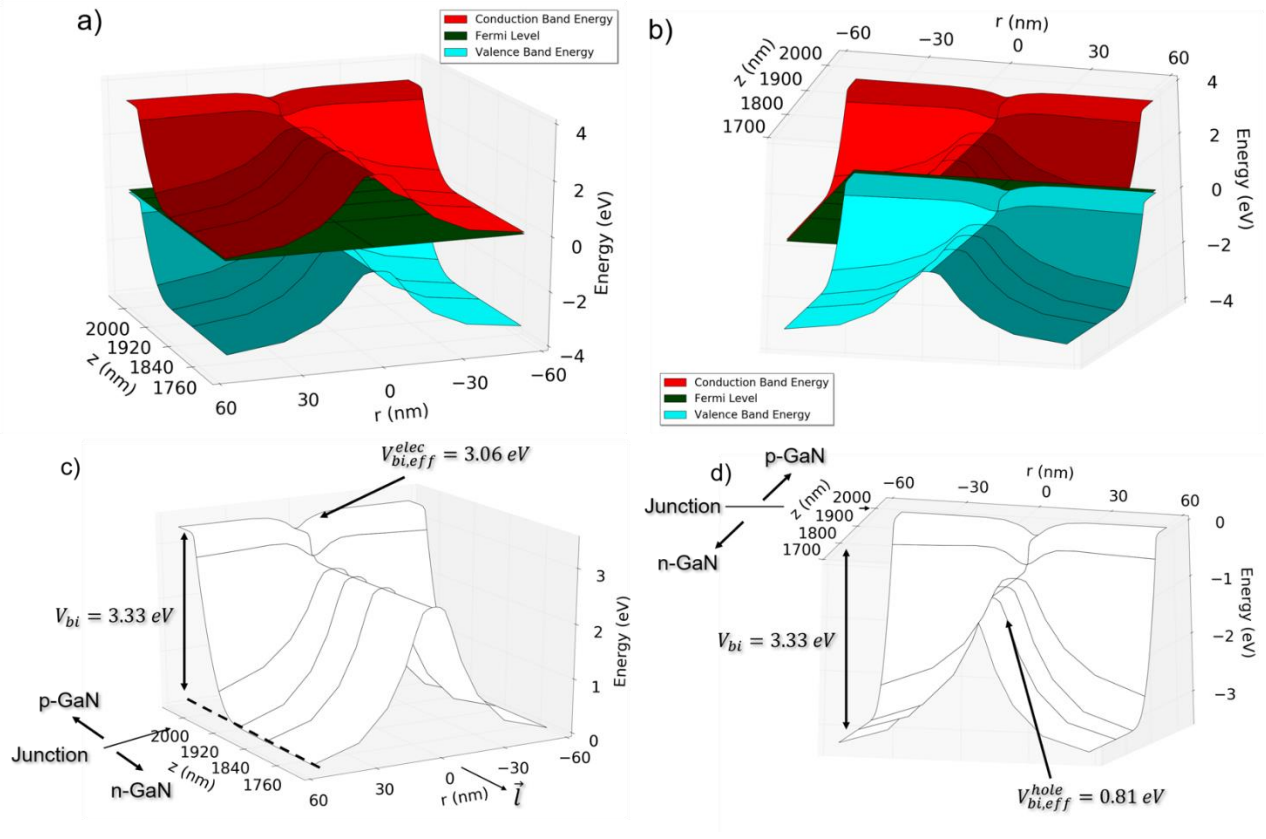

Figure 26: a) The full 3D zero bias band diagram of the p-n junction looking from the n-side down the dislocation line to clearly show the distortion of the band diagram around the TD line that reduces the barrier to diffusive electron current. b) The full 3D zero bias band diagram of the p-n junction rotated such that the perspective looks down the TD from the p-side. This shows more clearly the barrier to hole diffusive current and how the barriers to diffusive currents are asymmetric at the junction. c) The 3D zero bias band diagram of the p-n junction conduction band numerically annotated to demonstrate the reduction in the electron diffusion barrier around the dislocation. d) The 3D zero bias band diagram of the p-n junction valence band numerically annotated to demonstrate the marked reduction in hole diffusion barrier around the dislocation. Note that for all figures in this work that the metallurgical junction of the diode is at z = 2 μm.

In Figure 26a) and b), the modeled band diagram of a GaN *p-n* junction around a TD is presented. The TD screening region permeates much further into the n-GaN region than the p-GaN region due to the screening behavior of lightly vs. heavily doped material. This reduced area of influence of the TD within the p-GaN compared to the n-GaN means that any influence of the screening region on pn junction leakage current is minimal in the p-type region of the device. Furthermore, this means that as power devices push towards lower drift region doping levels to hold large reverse voltages, the effects of the TD on the leakage

associated with this screening region will similarly be amplified. It can also be seen that the band bending observed on the heavily doped p-side of the junction is substantially less than the n-side despite their trap energy levels being similarly distanced from their respective energy bands. On the p-side of the junction, the density of acceptors and trap states are on the same order of magnitude, thus there is little band bending behavior as the net charge in this region will be lower as the intentional acceptors can almost locally compensate the dislocation-related donor trap states.

In Figure 26(c) and (d), the contours of the conduction and valence bands respectively are shown separately from the full band diagram construction. In this construction, the asymmetry of the built-in voltage reduction on the n- and p-type sides of the junction is easier to observe. The difference in diffusion barrier height can be given by

$$\Delta V_{bi} = V_{bi} - V_{bi,eff}, \tag{21}$$

where V_{bi} is the bulk built-in potential and $V_{bi,eff}$ is the effective potential at the TD. On the n-type side, this is only 270 meV; this small reduction in the electron diffusion barrier is contrasted with the marked reduction in the barrier (2.52 eV) for holes. This result foreshadows that this structure should leak substantially more holes than electrons in forward bias since the equilibrium built-in potentials are asymmetric.

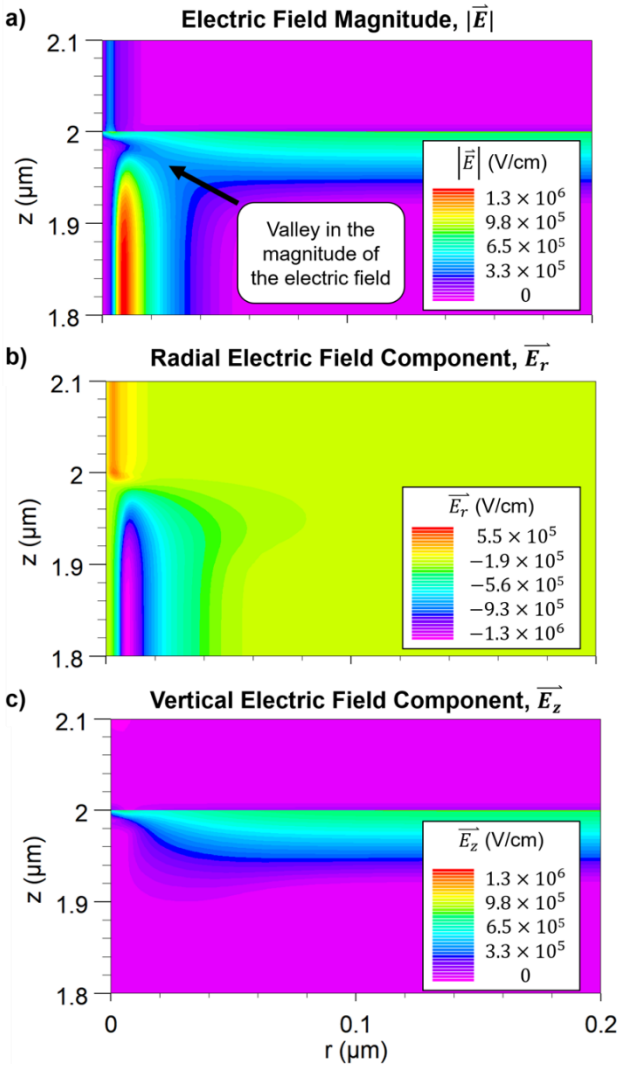

Figure 27: Electric field colormaps showing the a) magnitude, b) radial, and c) z-direction components. Note that at the intersection of the screening and depletion regions there is a valley in the magnitude of the electric field labeled in a). Additionally, it can also be seen that near the intersection, the electric field magnitude approaches zero where the maximum screening field would intersect with the maximum depletion electric field. Note that in c), the z-component of the electric field quickly approaches the field profile of a similar p-n junction with no dislocation (e.g., at a distance r ≈ 0.05 μm).

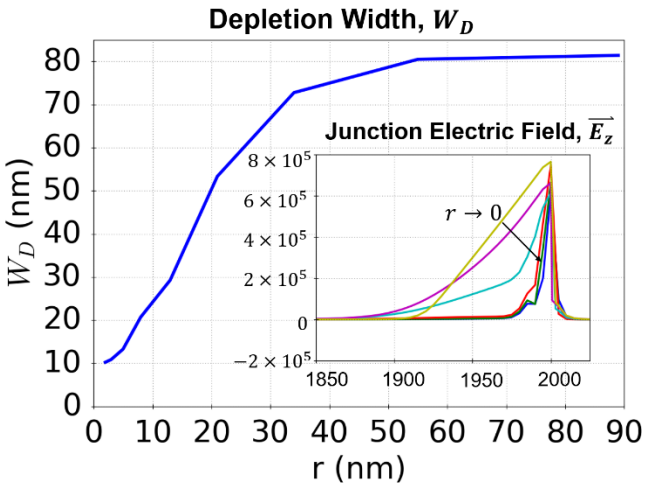

Figure 28: Plot of the depletion region width (calculated using the Depletion Approximation) changing with proximity to the TD core. Inset into the plot are the profiles of $\overrightarrow{E_z}$ approaching the dislocation core (r = 0) that are responsible for the formation of the junction depletion region. Note that near the TD ($r = 0$) both the maximum $\overrightarrow{E_z}$ and depletion widths are reduced thereby creating a reduced barrier to diffusion current through this region. Additionally, note that the W_D far away from the dislocation line approaches the value derived from basic depletion calculations for a p-n junction with no dislocation.

In Figure 27 a), the 2D electric field colormap of the zero bias pn junction is shown. The confluence of the screening and depletion region electric fields correlates to a marked reduction in the electric field magnitude near the dislocation core. Under forward bias, this region of reduced electric field enhances the diffusive current flow as will be shown in the following section. The potential peak appears in the core of TD. Therefore, the electric field, which is the differential of potential is zero as expected.

In Figure 28, the depletion region width is plotted with respect to distance from the TD core. Near the TD, the depletion width is reduced by 67%. Furthermore, in the inset of the plot, it can be observed that the maximum junction electric field is similarly reduced by 37%. These two factors result in a substantially reduced barrier to diffusive current across the junction.

Leakage Regime (2.4V Forward Bias)

At ($V = 2.4V$), high TD density GaN pn diodes have measurable leakage currents, and these currents can be reliably observed in standard computational models without problems with numerical noise.

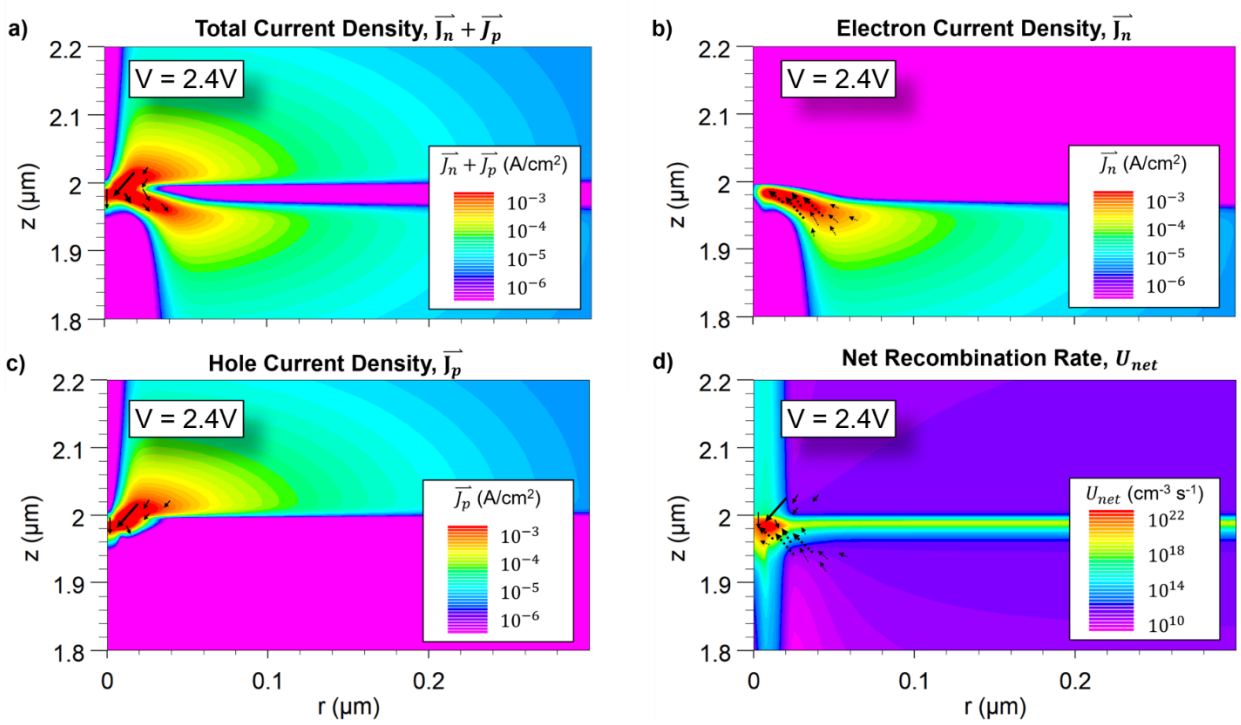

Figure 29: Carrier transport diagrams in the leakage regime. a) The total conduction current density for the vertical diode punctured by a threading dislocation. Note that there is current on both sides of the junction mediated by the intersection. b) The electron current density showing flow from the bulk of the n-GaN through the intersection and into dislocation trap region on the p-type side. c) The hole current density showing the flow of holes in similar magnitude to the flow of electrons. However, the holes appear to intrude much further into the n-GaN region than the electrons into the p-GaN region. d) Net recombination rate diagram showing a wide and strong area of recombination near the intersection and around the TD in the bulk. This recombination center at the intersection will be discussed further in the "Discussion" section.

In Figure 29, carrier current flow diagrams are presented. The flow of holes and electrons is almost symmetric on the p- and n-type sides of the junction, respectively. It has been previously observed at zero bias that the depletion width of the device reduces drastically with proximity to the TD, and in forward bias, this barrier reduction facilitates forward diffusive current to the region near the intersection. With a reduction in this barrier near the TD, carriers in the bulk regions of the device bypass the bulk depletion field by moving through this region. Once both carriers are confined together in this region within the device, they will rapidly recombine (ref. Equation (20)). Lastly, it is significant to note that the hole current from the p-type side of the junction intrudes much further into the n-GaN TD than electrons into the p-GaN. This phenomenon will be discussed further in the Discussion section.

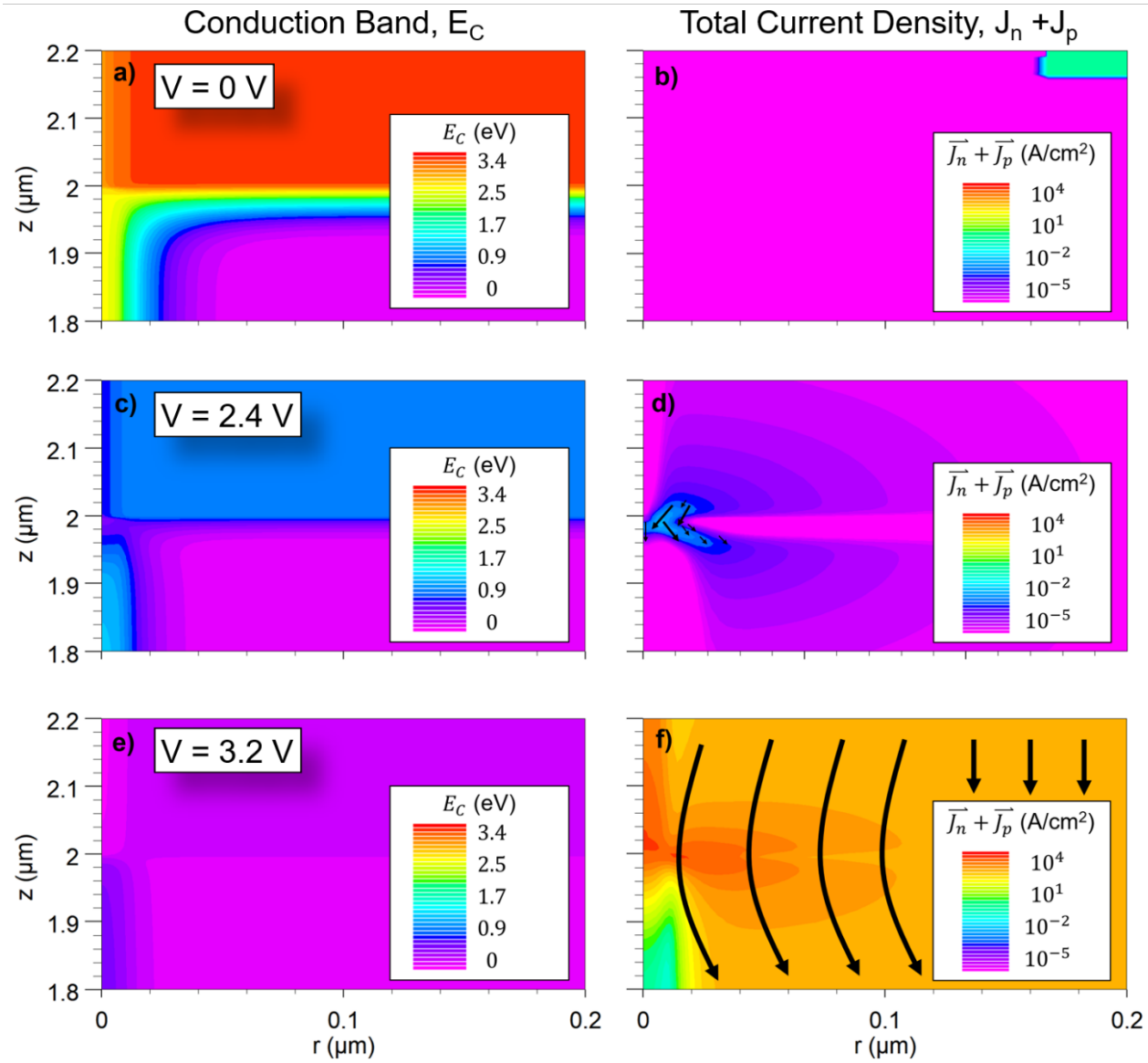

Figure 30: Conduction band diagrams for a) 0V, c) 2.4V, and e) 3.2V forward bias, and current density plots for b) 0V, d) 2.4V, and f) 3.2V forward bias. From these figures, note that the collapse in both the junction and screening electric field correlates to an increase in both the junction and TD mediated currents densities until full turn-on.

In Figure 30, it can be clearly seen that the intersection mediates leakage current at sub-turn-on voltages thereby allowing current to flow through the region of reduced depletion due to the distortion in the energy band diagrams around the TD. The contrast is particularly apparent when comparing the current vectors near the TD to those far away from the dislocation at V=2.4V. Away from the TD, there is negligible

current flow as would be expected in an ideal diode; however, near the TD, the current density magnitude exponentially increases as the flow of carriers moves through the region of influence of the TD.

J-V Characteristics

I-V curves were also simulated for this model and were compared to a control diode with no dislocation region. These I-V curves were normalized to a 3D model structure with cylindrical symmetry to obtain a current density (Figure 31).

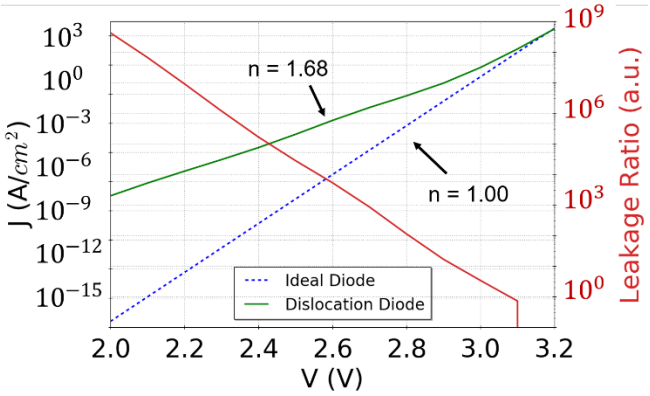

Figure 31: Voltage sweep analysis for the diode studied in this work against an ideal GaN pn diode of the same geometry. The left axis shows the current density of the diode as well as annotations indicating the ideality factors of the diode. The right axis shows the ratio of the current in the diode with a dislocation to one without a dislocation thereby showing a leakage ratio associated with a sample having a 10^{8} cm^{-2} threading dislocation density as is typical on heteroepitaxially grown GaN-on-sapphire.

When compared to an ideal diode, the diode with the dislocation puncturing the metallurgical junction displays quantifiably higher leakage current before turn-on. After turn-on, the effects of the dislocation on the carrier transport get screened by the injected carriers at forward bias, and this effect can be seen in both the J-V curves as well as the 2D models (Figure 29).

In Figure 31, the ratio between the current densities of a diode with and without a TD is plotted with the models' J-V data using the following formula

$$\Gamma = \frac{J_{TD} - J_{noTD}}{J_{noTD}} \tag{22}$$

where Γ is the leakage ratio, J_{TD} is the current density of a *p-n* diode with a TD, and J_{noTD} is the current density of the ideal *p-n* diode. The leakage current contributes substantially more current before turn-on after which the dislocation has been screened by the forward bias current. These current ratios match very closely with previous experimental work analyzing leakage current in vertical pn junctions in GaN[42].

IV. Discussion

Pinning Behavior at the Dislocation

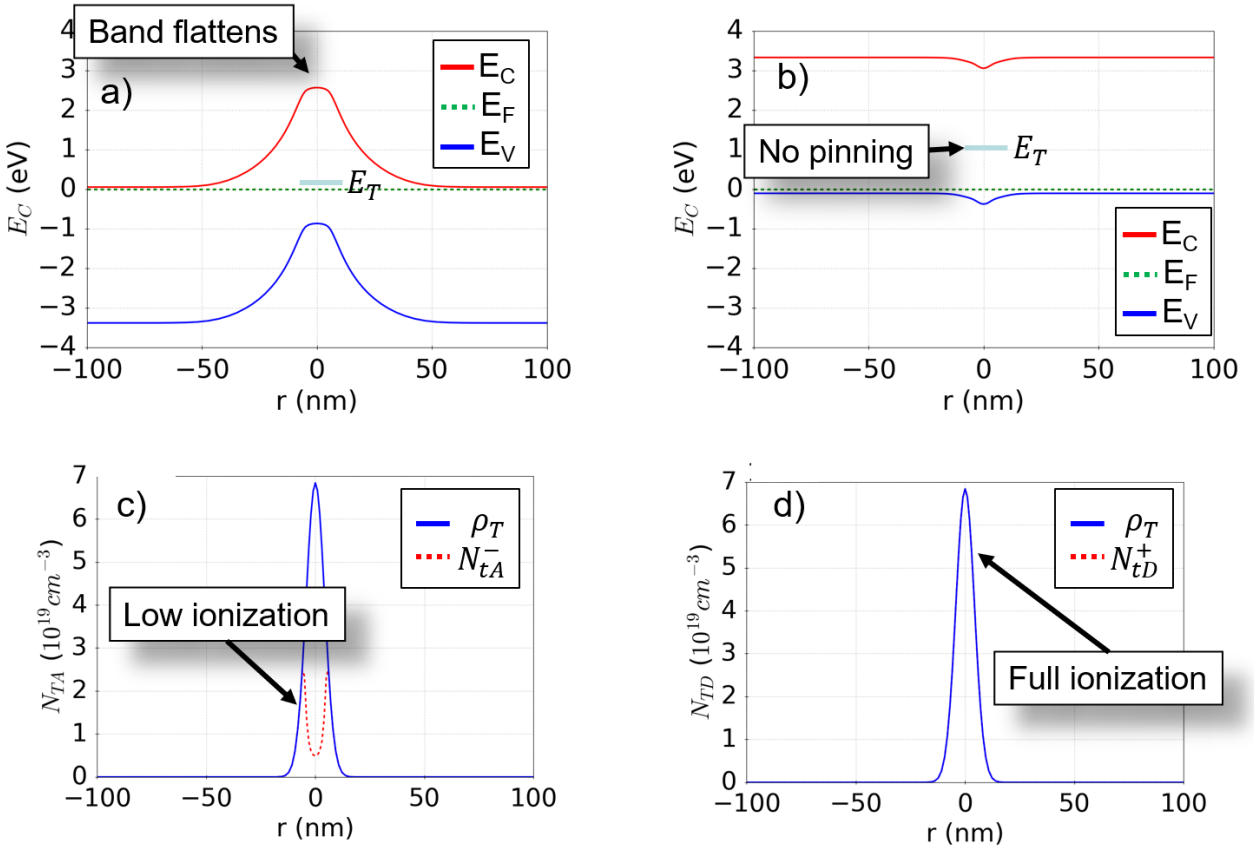

Figure 32: Band diagrams for a) lightly-doped n-GaN and b) heavily-doped p-GaN around a TD. In the bottom row are also shown the charge densities for c) lightly-doped n-GaN and d) heavily-doped p-GaN. Note that in the lightly-doped n-GaN, the band flattens near the dislocation indicating a very low electric field and reflecting a low occupancy as also indicated in the charge density graph in c).

Our results demonstrate that the previously observed small potential profiles around TDs in p-GaN[24] are due to the necessary doping required to obtain p-type conduction. Since the concentration of acceptors in

p-type GaN ($N_A = 5 \times 10^{19}\ cm^{-3}$) are on the order of trap state density near the dislocation core ($\rho_{T,max} = 6.84 \times 10^{19}\ cm^{-3}$), the net charge in the TD region in p-GaN is less than the net charge in the n-GaN where the donor concentration is much smaller ($N_D = 5 \times 10^{17}\ cm^{-3}$). This reduction in the net charge density in p-GaN directly correlates to the reduction in the associated dislocation band bending around those dislocations and results in a 100% hole occupancy of the dislocation-related trap states. It is significant to note that the trap states in the lightly doped n-GaN region of the diode are not fully occupied near the TD thus causing the hump in the charge concentration profile, as shown in the lower left corner of Fig. 10.

Furthermore, our results also demonstrate that the lightly doped, n-type side of the p-n junction does not actually physically pin the Fermi level at the trap state either. The low donor concentration is physically unable to compensate the trap states without bending the bands such that the trap state remains at or below the Fermi level. Although graphical representations appear to have the trap state pinned at the Fermi energy, it is in fact 67 meV above the trap energy level. Using Fermi statistics,

$$f(E) = \frac{1}{\exp\left(\frac{E_T - E_F}{kT}\right) + 1}, \tag{23}$$

it can be calculated that the occupancy of a trap state located 67 meV above the Fermi level will be ~8% which matches the occupancy given by the model.

Major Mechanisms of Leakage

The results presented clearly demonstrate a strong leakage mechanism at the intersection where the dislocation and metallurgical junction interact; however, additional studies are necessary to fully verify the effect of lightly doped regions with TDs on p-n junction leakage.

Leakage in n+ - p Diode

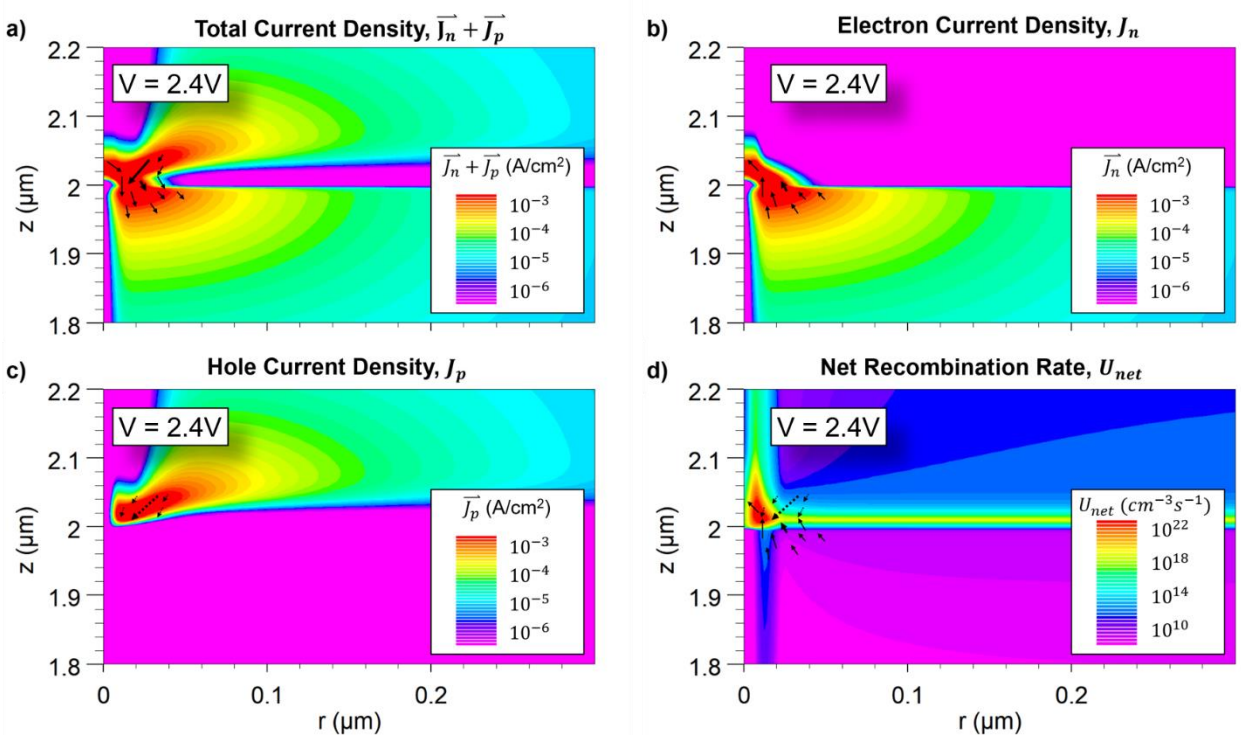

Figure 33: n+ - p diode leakage current and recombination profiles. All plots are plotted using a log scale with the same magnitudes given in previous current density figures. a) Total current density, b) electron current density, c) hole current density, and d) net recombination rate.

The first exploratory model inverted the weight of the doping to create a n+ - p junction rather than the p+ - n junction. This model verified that it is the lightly doped region of the diode that mediates the most leakage; in Figure 33a), the TD on the p-type side (which is now lightly doped with $N_A = 5 \times 10^{17}\ cm^{-3}$) carries a significant amount of electron current with the same partial occupancy and band flattening behavior observed in our main model. Furthermore, this current goes substantially further into the p-type region through the TD which indicates that carriers in these regions are more likely inhibited by their mobility as would be predicted if they were acting as majority carriers in these regions.

p-GaN Trap State Energy Dependence

As was previously stated, the precise location of the trap energy level for TDs in p-GaN is not known, thus models looking at p-n junctions with different p-GaN TD trap energy levels were simulated. It was observed that the trap state level of the p-type side was largely irrelevant to the presence of the previously observed leakage mechanisms. This finding indicates that although the energy level for TD traps in p-GaN is approximated as a deep trap state, its location within the band ultimately does not matter since one side of the junction trap states are deep and distort the band structure to allow the leakage mechanisms to occur. This result further reinforces the notion that if the acceptor concentration is on the order of the trap state concentration, they play a much more significant role than the trap state energy in determining the bending behavior around the TD.

Trap-Assisted Recombination Dependence

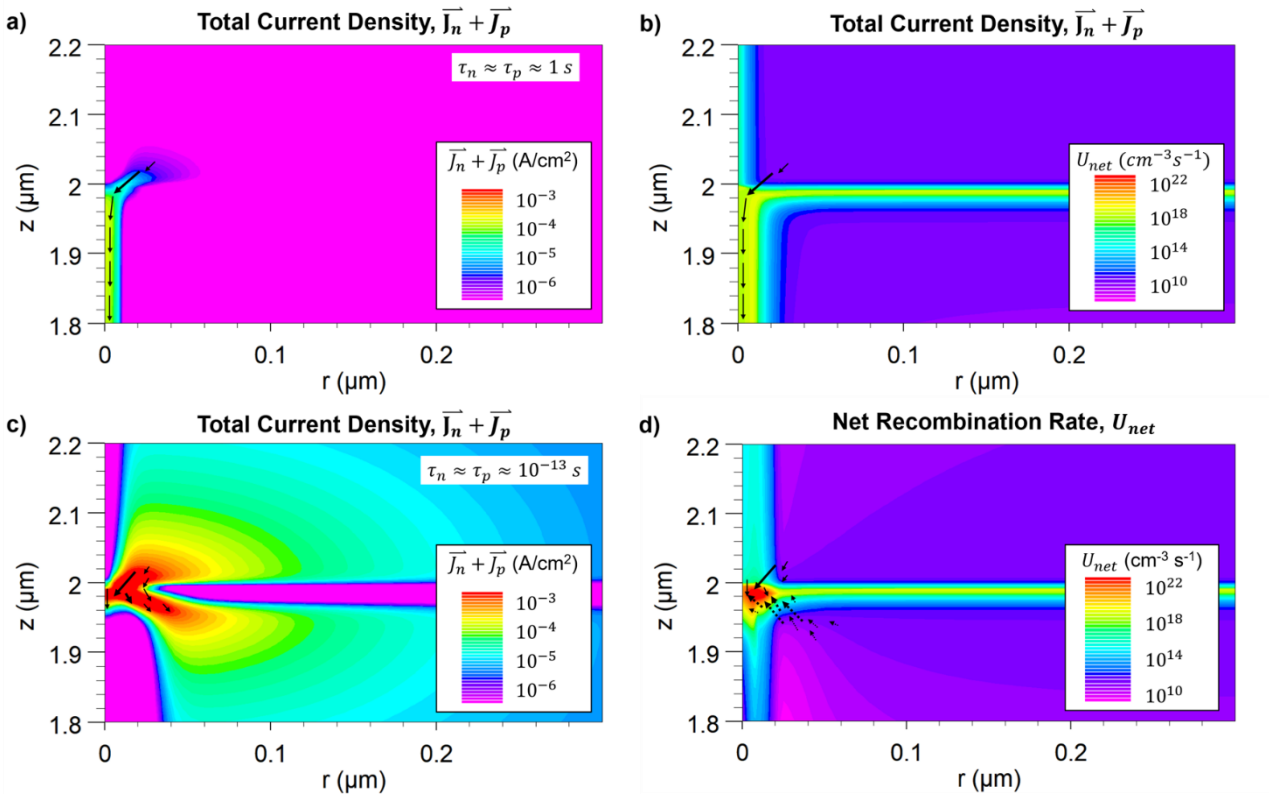

Figure 34: Total current density color maps highlighting the effect that the explicit, dislocation trap mediated carrier recombination has on the leakage current magnitude. a) Total current density colormap of

the diode with a 1s carrier lifetime (thereby negating recombination effects of the dislocation trap states). Note that even without any trap state recombination, the dislocation screening region on the lightly doped side of the junction continues to mediate leakage current. b) Total current density colormap of the control diode with 1fs carrier lifetime.

Previous models have indicated that the leakage mechanism around TDs are related to carrier recombination near the intersection as shown by disk-shaped regions of high recombination rates in Figure 29 and Figure 33. To test this, a model with trap-associated lifetimes of 1s was simulated to nullify the effect of trap state recombination at the interface. As can be seen in Figure 34, the removal of SRH recombination at TD trap states does not completely remove leakage currents, but it does reduce them by almost an order of magnitude. In addition to the SRH recombination at the interface near the TD, the diffusion current of the junction alone near the TD also provides leakage current well over what would be expected in a perfect p-n diode. This effect can further be seen in Figure 35. Although the SRH recombination at the TD trap states appears to have a significantly high leakage current in Figure 34, Figure 35 shows that the leakage current is largely caused by the depletion region and diffusion barrier reduction effects around the TD, for the leakage ratio of the no TD recombination diode over the ideal diode is approximately 10^4 at V = 2.4V compared to 10 between the Control and the no TD recombination diode. With the absence of recombination at the trap states, the diffusive current component of the Drift-Diffusion current model

$$\overrightarrow{J_n} = qn\mu_n\overrightarrow{E_n} + \boldsymbol{qD_n\nabla n} \tag{24}$$

is still greater than the drift component thereby allowing leakage current to flow. However, the drift current still reduces the overall current by repelling carriers away from the intersection. By adding in trap state recombination, the drift component of the model becomes irrelevant as carriers do not need to fully cross the depletion region. Instead, they simply need to overlap with the carriers diffusing from the other side of the junction at which point they rapidly recombine and create a much higher leakage current mediated by the depletion and barrier reduction and enhanced by the trap state recombination.

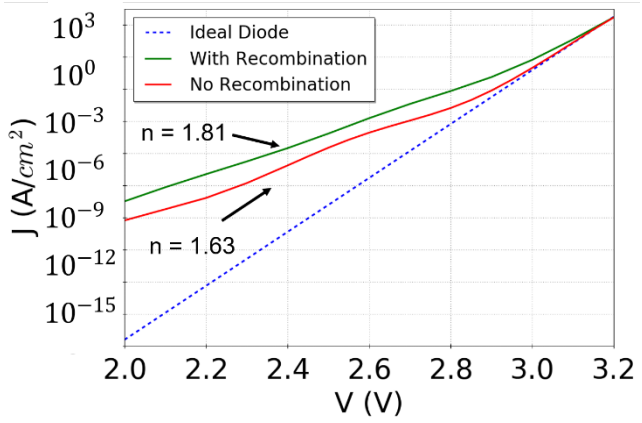

Figure 35: J-V curves comparing the ideal, control, and no recombination diode models.

Isolated Screening Region Geometry Dependence

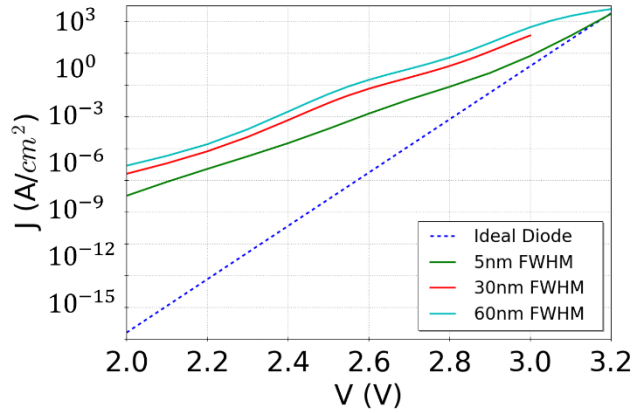

Figure 36: J-V curves contrasting the effects of only the trap state distribution (hence screening region length) on the leakage current. This study differentiates the effects of only the screening geometry without changing the dislocation line charge or device doping.

In addition to exploring the effect of screening region variance by controlling the doping in the junction, the screening region was also modified by changing the density profile of the TD-associated traps. These Gaussian FWHMs were modified to make them broader, but the peak trap state densities were also changed such that an experimentally observed one electron per c-lattice translation was maintained. Although models were attempted with narrow trap state distributions, these led to numerical instability that prevent simulation convergence. In Figure 36, the J-V curves of these broader trap state models are shown,

and it can be clearly observed that the width of the distortions does contribute significantly to the forward bias leakage current.

With the reduced trap state densities, the effects previously seen on the trap occupancy in the lightly doped region of the diode are eliminated, yet leakage current not only persists but increases substantially. This indicates that the occupancy of the trap states does not play a major role in facilitating leakage since the trap states are fully occupied for these cases. Furthermore, in Figure 37, we can see that the local magnitude of the leakage currents remains relatively unchanged with broader screening regions even as the total device current density increases. This indicates that the broader screening region interaction with the junction simply broadens the region over which diffusion current and SRH recombination can occur.

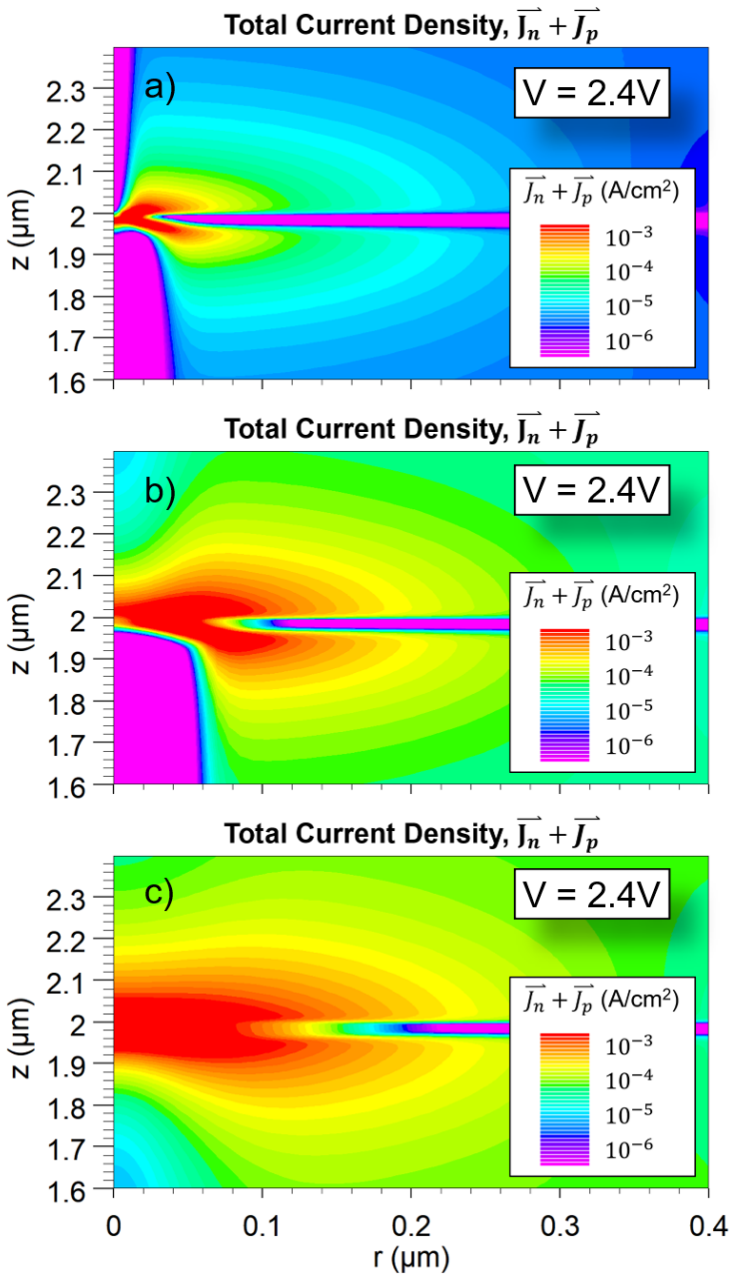

Figure 37: Conduction current densities for various FWHM TD trap distributions with a) the main model with a FWHM = 5nm, b) a FWHM = 30nm, and c) a FWHM = 60nm.

V. Conclusion

This work has presented a 2D model of a *p-n* diode punctured by a distribution of trap states associated with dislocations in accordance with prior investigations[26,40] and solved the Poisson-Drift-Diffusion system of equations using the Gummel method to determine the mechanisms by which dislocations mediate

leakage. It was discovered that the dislocation trap states were ionized by the surrounding dopants thus distorted the band in their vicinity with a heavy dependence on the doping density. This distortion of the energy bands results in a drastically reduced barrier to diffusion in forward bias, and this reduced diffusion barrier allows carriers to flow into a region of incredibly high recombination rates. It was discovered that regions around TDs in lightly doped semiconductors also inverted their majority carrier behavior which allowed leaked carriers to travel very far into lightly doped region through the TD. The regions of barrier reduction, SRH recombination, and majority carrier inversion created by the distortion in the band structure results in observable leakage currents and increased ideality factors in GaN *p-n* junctions with dislocations.

VI. Acknowledgements

This research was supported the Solid State Lighting and Energy Electronics Center (SSLEEC) at UCSB and by ARPA-E PNDiodes Program through a subcontract from the University of New Mexico (I. Kizilyalli, program manager). Prof. Yuh-Renn Wu was also funded by Ministry of Science and Technology (MOST) 108-2628-E-002-010-MY3.

VII. Reference Table

The table is arranged in alphabetical order of the description with similar variables grouped together in the table (i.e. conduction, valence, and intrinsic energies are grouped together).

Sym.	Description	Value	Units
k	Boltzmann constant	8.62×10^{-5}	eV / K
σ_n	Capture cross section – electrons	1×10^{-12} [22]	cm^2
σ_p	Capture cross section – holes	1×10^{-12} [22]	cm^2
$\bar{n}$	Capture rate – electrons	N/A	s^{-1}
$\bar{p}$	Capture rate – holes	N/A	s^{-1}
N_A	Concentration – acceptor dopants	5×10^{19}	cm^{-3}
N_D	Concentration – donor dopants	5×10^{17}	cm^{-3}
n	Concentration – electrons	N/A	cm^{-3}
Q_T	Concentration – charged trap states	N/A	
p	Concentration – holes	N/A	cm^{-3}
n_i	Concentration – intrinsic carriers	3.43×10^{-10}	cm^{-3}
N_A^-	Concentration – ionized acceptor dopants	N/A	cm^{-3}
N_{tA}^-	Concentration – ionized acceptor traps	N/A	cm^{-3}
N_D^+	Concentration – ionized donor dopants	N/A	cm^{-3}

N_{tD}^{+}	Concentration – ionized donor traps	N/A	cm^{-3}
ρ_T	Concentration – trap states*	N/A	cm^{-3}
J_n	Current density – electrons	N/A	A/cm^2
J_p	Current density - holes	N/A	A/cm^2
ϵ_r	Dielectric constant	8.9	---
N_C	Effective density of states – conduction band	2.2×10^{18}	cm^{-3}
N_V	Effective density of states – valence band	4.2×10^{19}	cm^{-3}
m_n^*	Effective mass – electron	1.98×10^{-31} ($0.2m_0$ [41])	Kg
m_p^*	Effective mass – holes	1.28×10^{-30} ($1.4m_0$ [42])	Kg
ψ	Electric potential	N/A	V
q	Electron charge	1.61×10^{-19}	C
e_n	Emission rate – electrons	N/A	s^{-1}
e_p	Emission rate – holes	N/A	s^{-1}
E_A	Energy level – acceptor	0.19 [34]	eV
$\underline{E_C}$	Energy level – conduction band edge	N/A	eV
E_D	Energy level – donor	0.025 [34]	eV
E_{Fn}	Energy level – electron quasi-Fermi	N/A	eV
E_{Fp}	Energy level – hole quasi-Fermi	N/A	eV
E_i	Energy level - intrinsic	1.73	eV
E_V	Energy level – valence band edge	N/A	eV
c	Lattice parameter – c-component	5.186	Å
τ_n	Lifetime – electrons	N/A	s
τ_p	Lifetime – holes	N/A	s
μ_n^{maj}	Mobility – majority electrons	400	$\frac{cm^2}{Vs}$
μ_n^{min}	Mobility – minority electrons	32	$\frac{cm^2}{Vs}$
μ_p^{maj}	Mobility – majority holes	8	$\frac{cm^2}{Vs}$
μ_p^{min}	Mobility – minority holes	26	$\frac{cm^2}{Vs}$
ϵ_0	Permittivity of free space	8.85×10^{-14}	F/cm
U	Recombination rate - net	N/A	s^{-1}
U_{SRH}	Recombination rate – Shockley-Read-Hall	N/A	s^{-1}
R_{SC}	Screening radius	N/A	nm
g_n	State degeneracy – conduction band	2	---
g_p	State degeneracy – valence band	4	---
T	Temperature	300	K
v_n	Thermal velocity – electrons	2.60×10^7	cm / s
v_p	Thermal velocity – holes	9.87×10^6	cm / s
$f(E_T)$	Trap state occupancy	N/A	---

Table 8: Variable legend providing detailed information on variables and units used in this work.

VIII. References

[1] C. Poblenz, P. Waltereit, S. Rajan, S. Heikman, U.K. Mishra, and J.S. Speck, Journal of Vacuum Science & Technology B: Microelectronics and Nanometer Structures Processing, Measurement, and Phenomena **22**, 1145 (2004).
[2] U.K. Mishra, L. Shen, T.E. Kazior, and Y.F. Wu, Proceedings of the IEEE **96**, 287 (2008).
[3] D. Denninghoff, J. Lu, M. Laurent, E. Ahmadi, S. Keller, and U.K. Mishra, in *70th Device Research Conference* (2012), pp. 151–152.
[4] S.W. Kaun, M.H. Wong, U.K. Mishra, and J.S. Speck, Semicond. Sci. Technol. **28**, 074001 (2013).
[5] B. Romanczyk, S. Wienecke, M. Guidry, H. Li, E. Ahmadi, X. Zheng, S. Keller, and U.K. Mishra, IEEE Transactions on Electron Devices **65**, 45 (2018).
[6] T. Nishida, T. Makimoto, H. Saito, and T. Ban, Appl. Phys. Lett. **84**, 1002 (2004).
[7] P. Waltereit, H. Sato, C. Poblenz, D.S. Green, J.S. Brown, M. McLaurin, T. Katona, S.P. DenBaars, J.S. Speck, J.-H. Liang, M. Kato, H. Tamura, S. Omori, and C. Funaoka, Appl. Phys. Lett. **84**, 2748 (2004).
[8] R. Sharma, P.M. Pattison, H. Masui, R.M. Farrell, T.J. Baker, B.A. Haskell, F. Wu, S.P. DenBaars, J.S. Speck, and S. Nakamura, Appl. Phys. Lett. **87**, 231110 (2005).
[9] H. Sato, A. Tyagi, H. Zhong, N. Fellows, R.B. Chung, M. Saito, K. Fujito, J.S. Speck, S.P. DenBaars, and S. Nakamura, Physica Status Solidi (RRL) – Rapid Research Letters **1**, 162 (2007).
[10] A. Tyagi, R.M. Farrell, K.M. Kelchner, C.-Y. Huang, P.S. Hsu, D.A. Haeger, M.T. Hardy, C. Holder, K. Fujito, D.A. Cohen, H. Ohta, J.S. Speck, S.P. DenBaars, and S. Nakamura, Appl. Phys. Express **3**, 011002 (2009).
[11] D.A. Haeger, E.C. Young, R.B. Chung, F. Wu, N.A. Pfaff, M. Tsai, K. Fujito, S.P. DenBaars, J.S. Speck, S. Nakamura, and D.A. Cohen, Appl. Phys. Lett. **100**, 161107 (2012).
[12] S. Lee, C.A. Forman, C. Lee, J. Kearns, E.C. Young, J.T. Leonard, D.A. Cohen, J.S. Speck, S. Nakamura, and S.P. DenBaars, Appl. Phys. Express **11**, 062703 (2018).
[13] Y. Hatakeyama, K. Nomoto, N. Kaneda, T. Kawano, T. Mishima, and T. Nakamura, IEEE Electron Device Letters **32**, 1674 (2011).
[14] I.C. Kizilyalli, A.P. Edwards, H. Nie, D. Disney, and D. Bour, IEEE Transactions on Electron Devices **60**, 3067 (2013).
[15] T. Oka, T. Ina, Y. Ueno, and J. Nishii, Appl. Phys. Express **8**, 054101 (2015).
[16] O. Aktas and I.C. Kizilyalli, IEEE Electron Device Letters **36**, 890 (2015).
[17] J.R. Dickerson, A.A. Allerman, B.N. Bryant, A.J. Fischer, M.P. King, M.W. Moseley, A.M. Armstrong, R.J. Kaplar, I.C. Kizilyalli, O. Aktas, and J.J. Wierer, IEEE Transactions on Electron Devices **63**, 419 (2016).
[18] Y. Yoshizumi, S. Hashimoto, T. Tanabe, and M. Kiyama, Journal of Crystal Growth **298**, 875 (2007).
[19] M. Qi, K. Nomoto, M. Zhu, Z. Hu, Y. Zhao, V. Protasenko, B. Song, X. Yan, G. Li, J. Verma, S. Bader, P. Fay, H.G. Xing, and D. Jena, Applied Physics Letters **107**, 232101 (2015).
[20] S. k. Mathis, A. e. Romanov, L. f. Chen, G. e. Beltz, W. Pompe, and J. s. Speck, Phys. Stat. Sol. (a) **179**, 125 (2000).
[21] S.K. Mathis, A.E. Romanov, L.F. Chen, G.E. Beltz, W. Pompe, and J.S. Speck, Journal of Crystal Growth **231**, 371 (2001).
[22] Z.-Q. Fang, D.C. Look, D.H. Kim, and I. Adesida, Appl. Phys. Lett. **87**, 182115 (2005).
[23] E.C.H. Kyle, S.W. Kaun, P.G. Burke, F. Wu, Y.-R. Wu, and J.S. Speck, Journal of Applied Physics **115**, 193702 (2014).
[24] D. Cherns, C. g. Jiao, H. Mokhtari, J. Cai, and F. a. Ponce, Phys. Stat. Sol. (b) **234**, 924 (2002).
[25] I. Arslan and N.D. Browning, Phys. Rev. B **65**, 075310 (2002).
[26] E. Müller, D. Gerthsen, P. Brückner, F. Scholz, Th. Gruber, and A. Waag, Phys. Rev. B **73**, 245316 (2006).
[27] D.C. Look and J.R. Sizelove, Phys. Rev. Lett. **82**, 1237 (1999).
[28] E.C.H. Kyle, S.W. Kaun, E.C. Young, and J.S. Speck, Appl. Phys. Lett. **106**, 222103 (2015).
[29] S.L. Rhode, M.K. Horton, W.Y. Fu, S.-L. Sahonta, M.J. Kappers, T.J. Pennycook, C.J. Humphreys, R.O. Dusane, and M.A. Moram, Appl. Phys. Lett. **107**, 243104 (2015).

[30] S. Usami, N. Mayama, K. Toda, A. Tanaka, M. Deki, S. Nitta, Y. Honda, and H. Amano, Appl. Phys. Lett. **114**, 232105 (2019).
[31] S. Usami, Y. Ando, A. Tanaka, K. Nagamatsu, M. Deki, M. Kushimoto, S. Nitta, Y. Honda, H. Amano, Y. Sugawara, Y.-Z. Yao, and Y. Ishikawa, Appl. Phys. Lett. **112**, 182106 (2018).
[32] K. Kumakura, T. Makimoto, N. Kobayashi, T. Hashizume, T. Fukui, and H. Hasegawa, Applied Physics Letters **86**, 052105 (2005).
[33] N.G. Weimann, L.F. Eastman, D. Doppalapudi, H.M. Ng, and T.D. Moustakas, Journal of Applied Physics **83**, 3656 (1998).
[34] K.C. Collins, A.M. Armstrong, A.A. Allerman, G. Vizkelethy, S.B. Van Deusen, F. Léonard, and A.A. Talin, Journal of Applied Physics **122**, 235705 (2017).
[35] S. Hafiz, F. Zhang, M. Monavarian, V. Avrutin, H. Morkoç, Ü. Özgür, S. Metzner, F. Bertram, J. Christen, and B. Gil, Journal of Applied Physics **117**, 013106 (2015).
[36] Z.Z. Bandić, P.M. Bridger, E.C. Piquette, and T.C. McGill, Solid-State Electronics **44**, 221 (2000).
[37] M. Leroux, N. Grandjean, B. Beaumont, G. Nataf, F. Semond, J. Massies, and P. Gibart, Journal of Applied Physics **86**, 3721 (1999).
[38] R.C. Jaeger and F.H. Gaensslen, IEEE Transactions on Electron Devices **27**, 914 (1980).
[39] J.G. Simmons and G.W. Taylor, Phys. Rev. B **4**, 502 (1971).
[40] W. Shockley, The Bell System Technical Journal **28**, 435 (1949).
[41] W. Shockley and W.T. Read, Phys. Rev. **87**, 835 (1952).
[42] C.A. Hurni, O. Bierwagen, J.R. Lang, B.M. McSkimming, C.S. Gallinat, E.C. Young, D.A. Browne, U.K. Mishra, and J.S. Speck, Applied Physics Letters **97**, 222113 (2010).
[43] L. Lymperakis, J. Neugebauer, M. Albrecht, T. Remmele, and H.P. Strunk, Phys. Rev. Lett. **93**, 196401 (2004).
[44] I. Vurgaftman, J.R. Meyer, and L.R. Ram-Mohan, Journal of Applied Physics **89**, 5815 (2001).
[45] A. Kasic, M. Schubert, S. Einfeldt, D. Hommel, and T.E. Tiwald, Phys. Rev. B **62**, 7365 (2000).

3.2 : Reverse Bias

I. Introduction

III-N semiconductors have been widely used in high-speed transistors[1–5], visible and ultraviolet (UV) optoelectronics[6–12], and vertical power electronics[13–17]. The high theoretical breakdown field (~3.3 MV/cm) and carrier mobility (>1,000 cm^2/V-s) have garnered interest in the field of power electronics where energy efficiency and high voltage operation are necessary. Vertical device topologies are useful for reducing the wafer footprint of power electronics by allowing voltage to be held across epitaxially grown interfaces rather than lateral ones. One of the major challenges to the performance of GaN vertical power devices has been the ubiquitous presence of threading dislocations (TDs) in the substrates for epitaxial growth. TDs have been repeatedly shown to exacerbate breakdown modes such as reverse bias current leakage in vertical GaN devices[16,18,19], but the breakdown mechanisms have been hitherto unstudied despite being experimentally observed.

The dislocation structure in GaN has been extensively studied by high-resolution x-ray diffraction (HRXRD) and transmission electron microscopy (TEM). Edge and mixed-type threading dislocations have been shown to be much more prevalent than their screw-type counterparts, but they all have a line vector within ~10° of the <0001> direction regardless of their Burger's vector, $\vec{\boldsymbol{b}}$ [20,21]. Furthermore, the electrical nature of TD trap states in *n*-GaN has been shown to be a deep acceptor in the band gap[22] with a line density of approximately one electron trap state per c-lattice translation[23]. It has also been observed that this trap state density associated with TDs results in a screening region around the dislocation as the donors provide electrons to the trap states to create regions of significant net charge. In a simple picture, the occupied dislocation-related acceptors in *n*-type material are screened by ionized donors as shown in Figure 38. Similarly, we assume that dislocation-related donors are screened by ionized acceptors in *p*-type material.

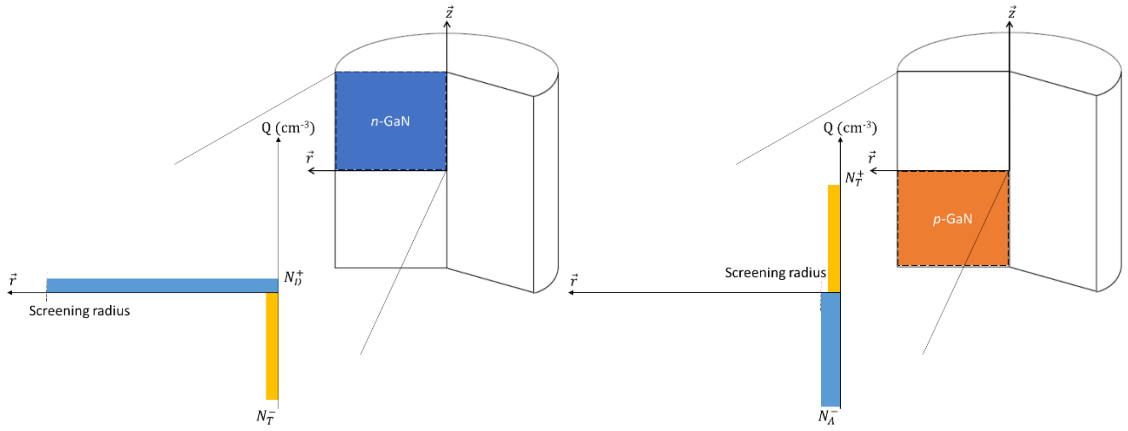

Figure 38: Schematic of screening region in the vicinity of a dislocation in a n-type (N_D= 5×10^{17} cm^{-3}) (left) and p-type (N_A= 5×10^{19} cm^{-3}) (right) GaN along with the corresponding charge profile. The charge region in p-GaN is much smaller due to the higher doping required for p-type conductivity

In the simplest treatment, the dislocation and space charge regions are cylindrical with constant trap state and dopant density (Figure 38). The screening radius can be simply calculated using charge neutrality and results in

$$R_{SC} = \sqrt{\frac{\rho_n}{\pi c}} * \sqrt{\frac{1}{N}} \qquad (3)$$

where ρ_n is the number of trap states per c-lattice translation, c is the c-lattice constant, and N is the uniform dopant concentration of the semiconductor. It is noted that, in typical nitride *p*-*n* junctions, all acceptors are assumed to be ionized within the *p*-side of the depletion width (typically on the order of 1-2 nm). The Mg acceptors would then provide screening in the band-bending region. This ionization and screening of the cylindrical area of the TD line distorts the energy band profiles around the dislocation with potentials of ~2.5 V as observed by electron holography in *n*-GaN[24]. This behavior has been attributed to the coalescence of defects around the TD core as suggested by Arslan and Browning[25] and observed by Müller et al.[26]. The trap state energy associated with such a band bending closely matches an electron trap state ~1.0 eV above the valence band maximum found in DLTS measurements[27]; additionally, the trap state density are consistent with previous experimental and theoretical values of approximately one electron trap state per c-lattice translation[28]. From these experimental observations and theoretical predictions, it is possible to construct an accurate band structure model of *n*-type GaN pierced by a TD.

In contrast, a band structure model of *p-type* GaN that includes the treatment of TD trap states has been substantially more elusive. Electron holography analyses have found regions of negative space charge that is likely associated with screening acceptors around a donor trap states coalescing near TDs in *p*-GaN[24]. However, the high acceptor concentration (needed to achieve measurable hole conductivity) results in a screening region that is smaller than the resolution of the electron holography method (~2 nm). Thus, the nature of the TD charge behavior in *p*-GaN remains experimentally unobserved. However, in previous studies, TDs in *p*-GaN act as nonradiative centers similar to *n*-GaN as shown by cathodoluminescence (CL) results[23], thus we assume that the TD trap states behave similarly in *p*- and *n*-type GaN.

In our previous work[29], GaN *p-n* diodes with a single threading dislocation were modeled in forward bias. It was found that the band distortions observed in the unipolar regions experimentally result in a reduced diffusion barrier for carriers to bypass the built-in potential of the diode thereby mediating a diffusive leakage current in forward bias. In this work, we will use the same simulation system with an additional mathematical model to address dislocation-mediated reverse bias leakage currents.

II. Model

In Appendix A, all relevant variables are given in alphabetical order to assist in understanding the parameters and models used in this work.

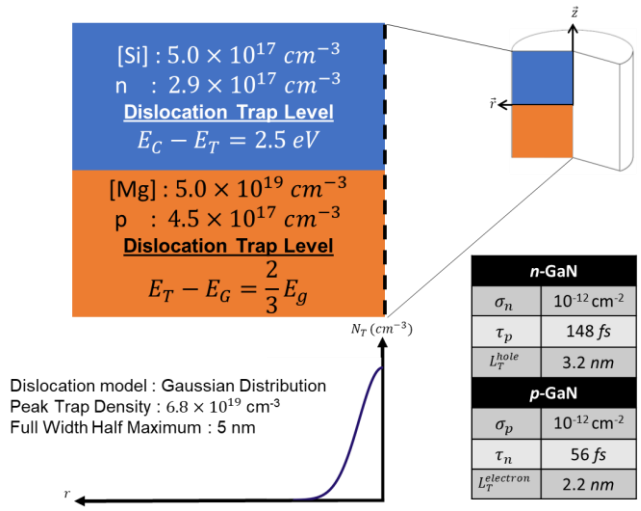

Figure 39. Figure shows the model for the p-n diode, which is a cylinder around a dislocation. The dislocation was modeled as a Gaussian distribution of deep trap states. Trap state energy within the n-type

region was based on experimental results while the p-type region was placed arbitrarily deep in the energy gap. In the right table, values for trap capture cross section (σ), minority carrier lifetime (τ), and minority carrier diffusion length (L_T) are given for the trap state region associated with the TD line.

In this study, Silvaco's ATLAS modeling software was used to solve for the 2D *p-n* junction model shown in Figure 39. Cylindrical coordinates were used to simplify the computational requirements by utilizing the six-fold rotational symmetry of the 3D crystal structure about the TD line vector, <0001>, without resorting to a full 3D treatment. N_A and N_D values are chosen based on experimentally typical values for vertical GaN *p-n* junctions doped with Mg and Si, respectively. The model r-dimension limit of 564 nm approximates a 10^8 cm^{-2} TD density as is typical in commercially available GaN growth on either Al_2O_3 or SiC. Our TD-associated trap state region was treated as a Gaussian distribution with FWHM of 5 nm and a peak trap state density of 6.84×10^{19} cm^{-3}. This Gaussian broadening was necessary as treating the dislocation as a line charge results in errors due to charge discontinuities. This distribution approximates a one electron per c-lattice translation when normalized in the z-direction[42]. Trap energy levels within the bandgap were E_C – 2.5 eV and E_V + 2.3 eV for *n*- and *p*-type GaN, respectively. Although the energy level of the dislocation trap state in *n*-GaN is well-documented, the level for *p*-GaN is approximated as an arbitrarily deep donor state. To represent the dislocation traps within bulk *p*-GaN, we used the deep level spectroscopy data presented by Zhang et.al.[27] The paper reported *p*-GaN to have trap levels at 0.48 eV, 1.02 eV, 1.50 eV, 2.42 eV, 3.00 eV and 3.28 eV above the valence band. Taking the average of these different energy levels gives us 0.59 eV, which approximates to two-thirds of the bandgap.

Using the approximation of a $10^{16}\ cm^{-3}$ trap state density in the bulk regions away from the dislocation, a capture cross section for both electrons and holes of $10^{-12}\ cm^2$ was chosen based on the following equations:

$$\tau = (\rho_T * \sigma * v)^{-1} \tag{25}$$

$$L_T = \sqrt{\frac{kT}{q} * \mu * \tau}, \tag{26}$$

where τ is the minority carrier lifetime; ρ_T is the local trap concentration; σ is the trap minority carrier capture cross section; v is the minority carrier thermal velocity; L_T is the minority carrier diffusion length; and μ is the minority carrier mobility. The parameters chosen resulted in lifetime and diffusion length values given in Table 9 using the minority carrier mobilities found by Kumakura et al.[30]. The bulk values given in this table are within the expected range for minority carrier diffusion length and lifetime[30–33] and were observed in our diode model with no dislocation.

	$\rho_T\ (cm^{-3})$	τ_n	$L_T^{elec}\ (nm)$	τ_p	$L_T^{hole}\ (nm)$
TD core	6.84×10^{19}	56 fs	2.1	148 fs	3.2
Bulk	10^{16}	0.38 ns	178	1.01 ns	261

Table 9: Minority carrier lifetimes and diffusion lengths for different trap state conditions. The bulk lifetimes are within experimental parameters for minority carrier lifetimes[30].

The model consisted of a mesh with a radial dimension of 0.564 μm which approximates to a threading dislocation density (TDD) of 10^8 cm^{-2} and a vertical dimension of 4 μm with the metallurgical junction at 2 μm. The resolution of the mesh varies from 1 Å near the junction and dislocation to 50 nm in the bulk. The Poisson and steady-state Current Continuity equations are solved on our mesh self-consistently using the Gummel method (Figure 40).

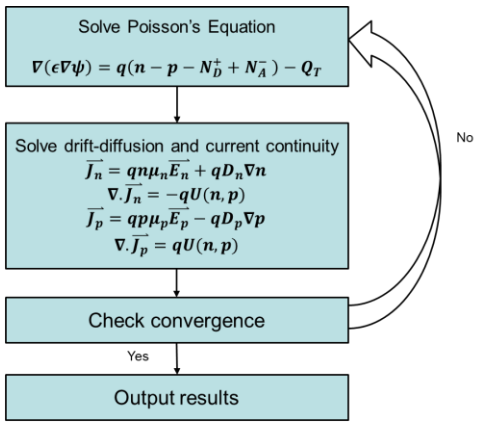

Figure 40: Process overview the Gummel method

$$\vec{\nabla} \cdot \left(\epsilon \vec{\nabla} \psi\right) = q(n - p - N_D^+ + N_A^-) - Q_T \tag{27}$$

$$\nabla \cdot \overrightarrow{J_n} = -qU(n,p) \tag{28}$$

$$\nabla \cdot \overrightarrow{J_p} = qU(n,p) \tag{29}$$

In the Poisson equation (27), ψ is the electric potential; n and p are the electron and hole concentration; N_D^+ and N_A^- are the ionized donor and acceptor concentrations. In the current continuity equations, $\overrightarrow{J_n}$ and $\overrightarrow{J_p}$ are the electron and hole current densities, and $U(n, p)$ is the net recombination-generation rate. The current density values are calculated by dividing the current values with the cross-sectional area of the cylinder (which has a radius of 564 nm).

In addition to these core equations, additional models are necessary to include the various behaviors of the GaN material systems and trap physics. These are discussed below.

Incomplete Ionization Model

Mg_{Ga} has been found to have activation energy approximately 190 meV[34]. In order to accurately model *p*-GaN, we used the incomplete ionization model[35] to account for the thermal activation of both the donors and acceptors in GaN.

$$N_D^+ = \frac{N_D}{1 + g_n exp\left(\frac{E_{Fn} - (E_C - E_D)}{kT}\right)} \tag{30}$$

$$N_A^- = \frac{N_A}{1 + g_p \exp\left(\frac{(E_A - E_V) - E_{Fp}}{kT}\right)}, \tag{31}$$

where N_D^+ and N_A^- are the ionized donor and acceptor concentrations; N_D and N_A are the donor and acceptor concentrations; g_n and g_p are the conduction and valence band degeneracies; E_{Fn} and E_{Fp} are the electron

and hole quasi-Fermi levels; $(E_C - E_D)$ and $(E_A - E_V)$ are the donor and acceptor activation energies. Using these equations, it is predicted that only ~1% of the Mg acceptor dopants will contribute holes to the GaN semiconductor while ~60% of the Si donors will contribute electrons. In addition, unintentionally-doped (UID) GaN is generally *n*-type due to the unintentional doping by oxygen (on the order of 10^{16}). This, along with the low activation efficiency requires high Mg concentrations to produce *p*-type GaN with the necessary hole concentration for conductivity.

Our model makes two basic doping assumptions. Firstly, the model uses an abrupt metallurgical junction such that there is no overlap between the *p*- and *n*-type regions of the diode. Secondly, the model does not explicitly specify any compensating defects or recombination centers away from the dislocation but rather combines the all real crystal imperfections into a minority carrier lifetime within the range of values provided in the literature[30].

Shockley-Read-Hall (SRH) Trap-Assisted Recombination Model

To model the charging and screening effects around the dislocation line, a trap ionization model was implemented. The Simmons and Taylor model (based on Shockley-Read-Hall recombination statistics)[36–38] was used to simulate the occupancy, $f(E_T)$, and charge state density of trap states, Q_T, associated with the TD line:

$$Q_T = q(N_{tD}^{+} - N_{tA}^{-}) \tag{32}$$

$$N_{tA}^{-} = \rho_T * f(E_T) \tag{33}$$

$$N_{tD}^{+} = \rho_T * (1 - f(E_T)) \tag{34}$$

$$f(E_T) = \frac{\bar{n} + e_p}{e_n + \bar{n} + \bar{p} + e_p} \tag{35}$$

$$\bar{n} = \nu_n \sigma_n n \tag{36}$$

$$\bar{p} = \nu_p \sigma_p p \tag{37}$$

$$e_p = \nu_p \sigma_p N_V \exp\left(\frac{E_V - E_T}{kT}\right) \tag{38}$$

$$e_n = \nu_n \sigma_n N_C \exp\left(\frac{E_T - E_C}{kT}\right) \tag{39}$$

In this system of equations, Q_T represents the concentration of charged trap states; N_{tD}^{+} and N_{tA}^{-} are the concentration of ionized donor and acceptor trap states; ρ_T is the density of trap states, $f(E_T)$ is the Fermi occupancy function at the trap state energy level; $\bar{n}$ and $\bar{p}$ are the electron and hole capture rates; ν_n and ν_p are the thermal velocities for electrons and holes; σ_n and σ_p are the electron and hole capture cross sections; n and p are the electron and hole concentrations; e_p and e_n are the hole and electron trap emission rates; N_V and N_C are the effective density of states for the valence and conduction bands; E_V and E_C are the valence and conduction bands; and E_T is the trap state energy level. The electron and hole concentrations given in (36) and (37) depend on the carrier quasi-Fermi levels. This means that, in forward bias, the quasi-Fermi levels split near the junction, changing the behavior of the traps in these regions. This change in carrier statistics in the regions is incorporated in these two equations by the inclusion of the local carrier concentrations which depend on the quasi-Fermi levels. Apart from that, the trap states are given a capture cross section such that the minority carrier lifetimes and minority diffusion lengths in the bulk associated with a lower concentration of these traps matches with previously found experimental evidence. The chosen values for capture cross section also come into effect here when calculating the carrier capture rate for trap occupancy. Additionally, in equation (32), N_{tD}^{+} and N_{tA}^{-} are the concentration of ionized donor and acceptor trap states, respectively. The occupancy of the trap states within the semiconductor depends on the mechanistic rates at which that trap either captures or emits carriers. These rates depend on the traps' position in the energy band as well as the local Fermi level which dictates the local free carrier concentration. For the electron occupancy of traps given in Equation (35), the capture rate of electrons, $\bar{n}$, and the emission rate of holes, e_p are the mechanisms that will cause that trap to be occupied by an electron

are Thus, the steady state occupancy of the trap is characterized by the ratio of these occupying rates to all the rates on that trap state.

Equation (35) expressing the occupancy of the localized trap state is simply a re-written form of the SRH recombination equation with the coefficients rewritten to more explicitly represent carrier emission and capture.

Additionally, Shockley-Read-Hall[38] recombination rates are used directly to model trap-assisted recombination rates using the following equation:

$$U_{SRH} = \frac{pn - n_i^2}{\tau_n \left[p + n_i \, exp\left(\frac{E_i - E_T}{kT}\right)\right] + \tau_p \left[n + n_i \, exp\left(\frac{E_T - E_i}{kT}\right)\right]} \tag{40}$$

where U_{SRH} is the Shockley-Read-Hall recombination rate; p and n are the hole and electron concentrations; n_i is the intrinsic carrier concentration; τ_n and τ_p are the electron and hole lifetimes; E_i is in the intrinsic energy level; and E_T is the trap state energy level.

Trap Assisted Tunneling

In addition to these core equations and the models outlined above for general GaN *p-n* junction, the Trap-Assisted Tunneling model[39,40] was also included for the purposes of simulating reverse bias leakage currents in the presence of a high electric field. In this model, an additional recombination-generation term

$$U_{TAT} = \frac{q m^* \left|\vec{E}\right| M^2 g_T \rho_T}{8\pi\hbar^3 (E_T - E_V)} \exp\left(-\frac{4\sqrt{2m^*(E_T - E_V)^3}}{3q\hbar\left|\vec{E}\right|}\right) \tag{41}$$

is included in Equations (28) and (29). In this model, U_{TAT} is the trap-assisted tunneling net recombination-generation rate, q is the electron charge, m^* is the effective mass of the carrier, $|\vec{E}|$ is the magnitude of the local electric field, M^2 is the matrix element for the trap potential[41], g_T is the degeneracy of the trap states, ρ_T is the density of trap states, $\hbar$ is Planck's constant, and E_T is the trap state energy level. Note that the

electric field magnitude is located in both the numerator outside the exponent and in the denominator of the argument of the exponent – this means that as the electric field magnitude increases at each mesh point, the exponential will converge to 1 while the outside multiple will increase linearly, thus for the purposes of this work where the electric fields are very large, the net recombination-generation rate is approximately linearly related to the electric field magnitude. This model accounts for the net recombination-generation of carriers across the band with the assistance of trap states with negative values of U_{TAT} correlating to a net generation of carriers. It was shown below that the peak in net generation of carriers occurs in a small region on the *n*-side of the junction. This corresponds to the peak in the electric field, which occurs on the *n*-side due to the structure being under reverse bias.

III. Results

Before discussing reverse bias results, we first confirmed that our zero bias band diagram with the additional physical models added matched our band diagram in previous work[29] on forward bias leakage currents.

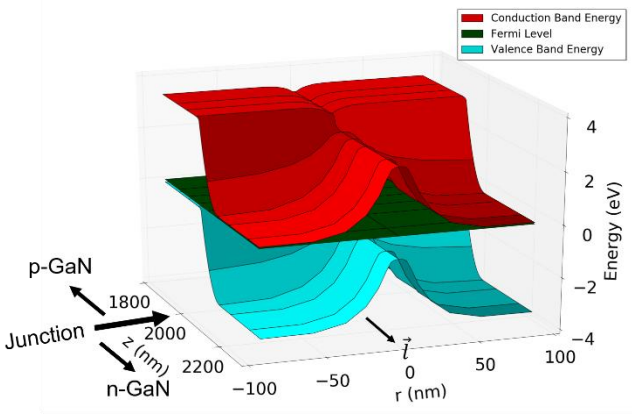

Figure 41: Equilibrium band diagram for the p-n junction in this work. This band structure matches our previously modeled p-n junctions observing forward bias leakage currents.

As the voltage bias applied to the system increases, the numerical stability decreases, extending the time it takes for the calculations to converge. Thus, beyond 80 V, the software hits a ceiling and is unable to converge to a solution. Upon confirmation of expected equilibrium band structure, the band diagram under 80 V reverse bias was analyzed and is shown in Figure 42.

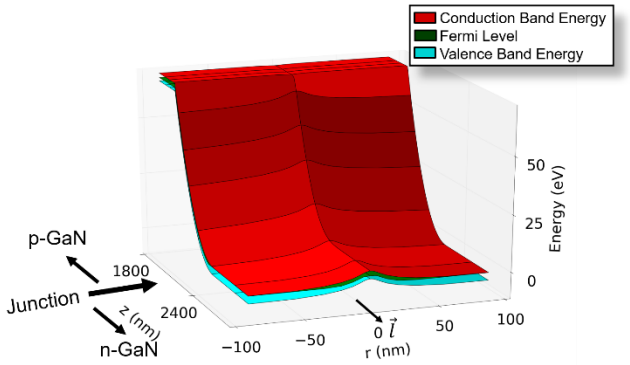

Figure 42: Band diagram for the modeled p-n junction under 80 V reverse bias. Note that the band distortions observed at equilibrium persist into reverse bias but are overshadowed by the bending of the junction due to the applied bias.

Since the mechanisms for leakage in reverse bias are inherently drift rather than diffusion related, the electric field profiles are considered and shown in Figure 43. In contrast to modeling forward bias characteristics, the electric fields are enhanced rather than diminished in reverse bias. This causes a peak in the electric field near the dislocation and junction due to the intersection of large components of the r- and z-components of the electric field. Recall that the recombination-generation due to TAT relates linearly to electric field, thus this peak in the electric field should generated electron-hole pairs that result in leakage. It was also found that varying the doping density in the junction did not affect its behavior.

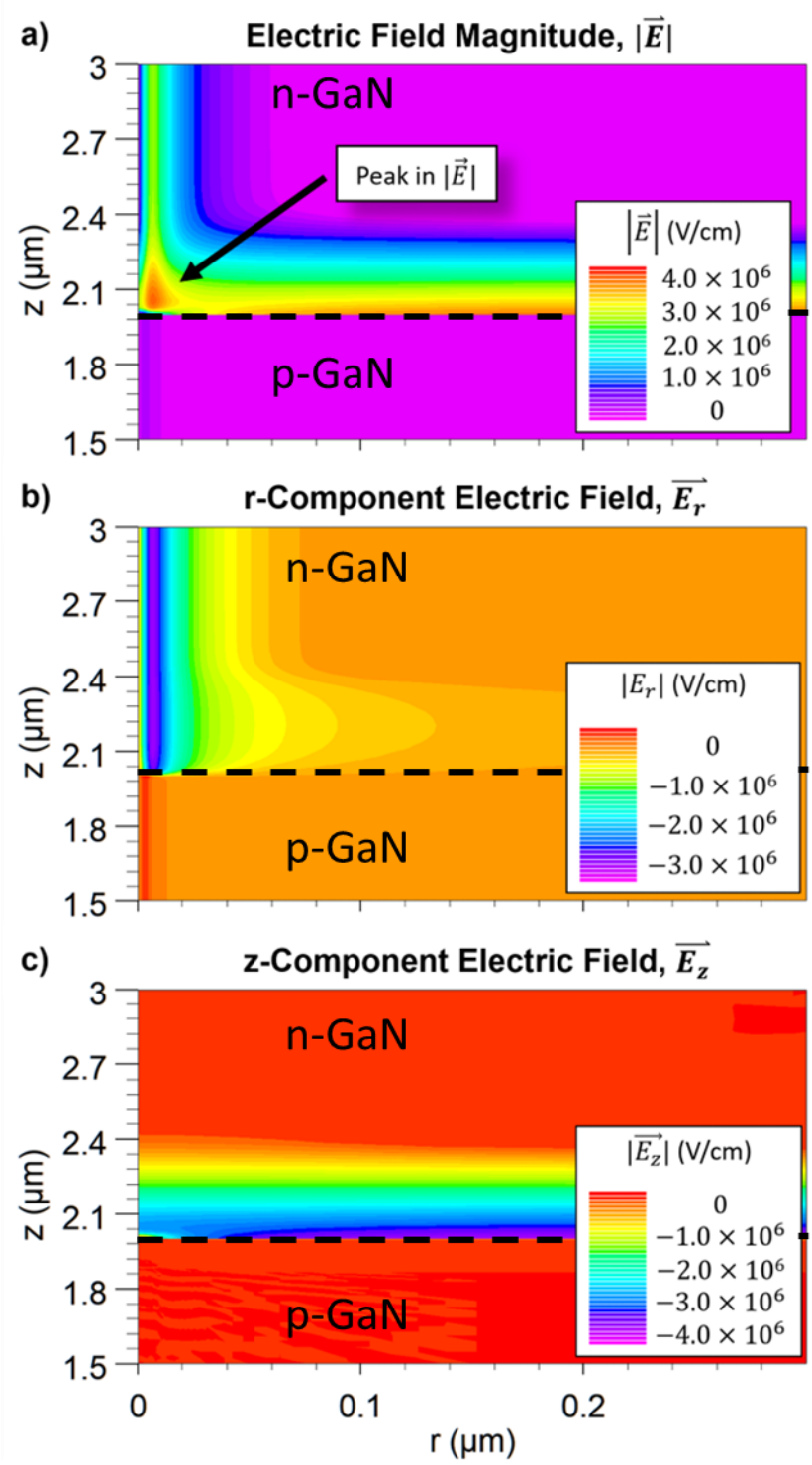

Figure 43: Electric field colormaps for the diode under study. a) The electric field magnitude - note the peak in electric field near the intersection of the dislocation with the junction. b) the radial component of the electric field. c) the z-component of the electric field.

In Figure 44, colormaps of the leakage currents are given as well as a recombination colormap on a linear scale. It shows that dislocation-mediated leakage current at reverse bias is driven by a generation of carriers at the peak electric field point.

These e-h pairs are generated into a strong electric field that then sweeps the carriers apart with the holes going into the *p*-GaN and the electrons going into the *n*-GaN thereby resulting in a leakage current.

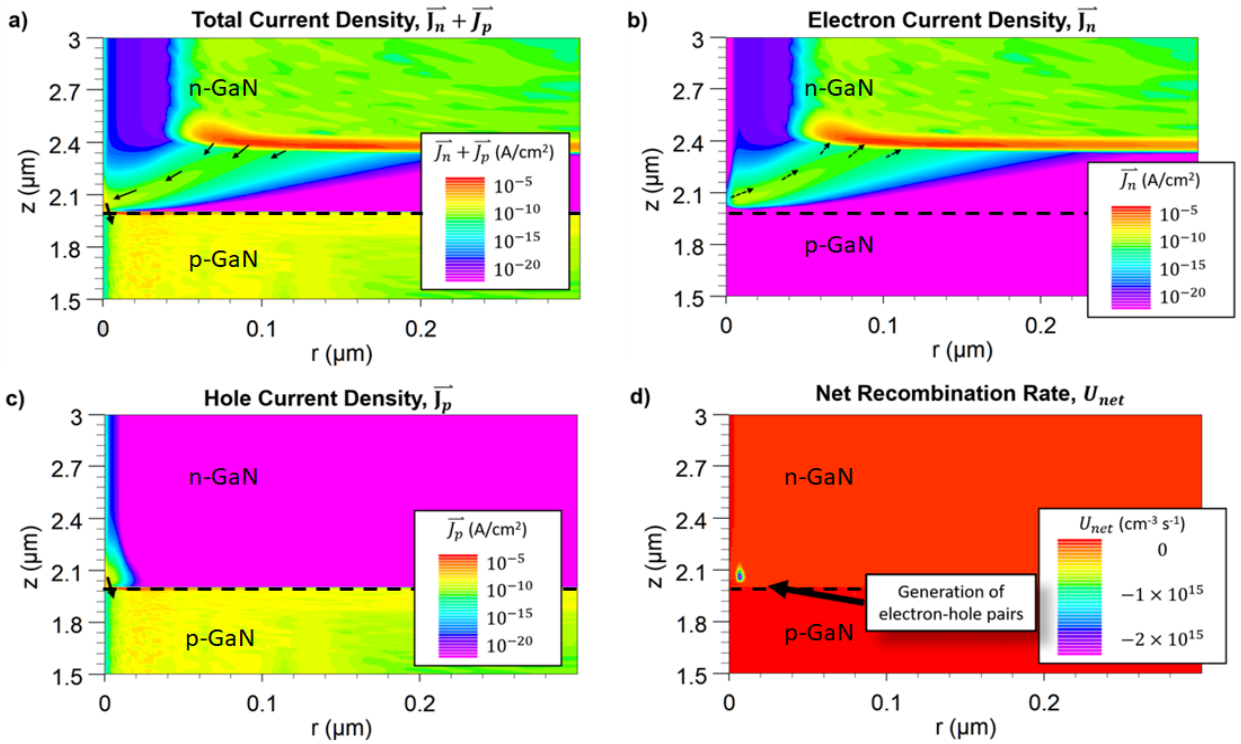

Figure 44: Leakage current color maps. The bold arrows represent the flow of current in the conventional sense ie. following a positive test charge whereas dotted arrows denote the actual direction of flow of the electrons. a) The total conduction current density showing current flowing from the n- to the p-side of the junction. b) The electron current density showing that electrons are flowing from the dislocation-junction intersection towards the p-side bulk due to the high electric field. c) Hole current density showing a geometrically smaller region in which holes are flowing from the intersection into the nearby p-GaN region. d) The net recombination-generation colormap on a linear scale showing a sharp, negative region at the peak electric field. Negative values on this scale indicate that generation occurs in this region. The slight difference in hues between the red in the p-GaN and n-GaN region are a result of slight numerical differences from the simulation. The values in both regions are still essentially zero, thus showing for all practical purposes, recombination only occurs in the vicinity of the interaction of the threading dislocation and the junction

Finally, J-V curves comparing the reverse bias leakage currents of the diode studied in this work with different models were also plotted. In Figure 45, current densities are plotted with respect to the reverse

bias voltage. The first comparative model removes the trap states completely from the model to simulate a diode with no dislocation in it – this is an ideal diode and should demonstrate no leakage current. The second comparative model keeps the dislocation-associated trap states in the model but removes the trap-assisted tunneling mechanism that appears to be essential to this leakage mechanism. In Figure 45, it can be observed that both the diodes without the dislocation trap states and without TAT have leakage currents that are primarily characterized by noise. This noisy behavior is due to the floating-point limit in our simulations and an artifact of the convergence error requirement. Thus, we assume the region to be at zero current. The dislocated sample with TAT included, however, displays a measurable leakage current after approximately 50 V reverse bias when the average reverse electric field is 1.7 MV/cm in the junction. This implies that trap-assisted tunneling, which leads to minority carrier recombination, is a fundamental mechanism in which dislocations causes leakage in the reverse direction. Although this model hasn't been explicitly tested in the literature, the results are incredibly close to previous work conducted by Hurni et al.[42].

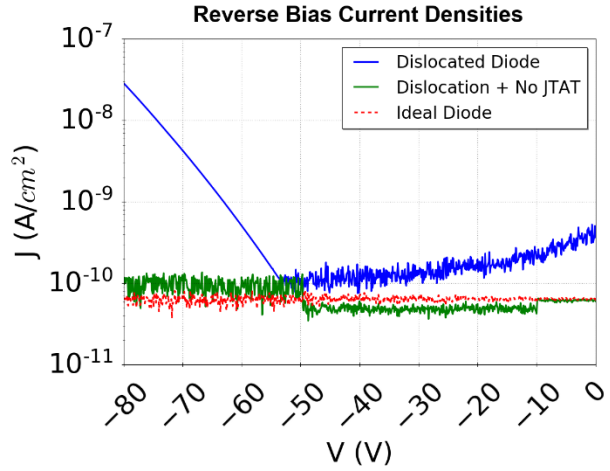

Figure 45: Reverse bias current density plots for the models under study. Note that the J-V curves for the model with no dislocation and with no trap-assisted tunneling are almost the same while the dislocated sample in this study demonstrates a measurable leakage current at applied biases greater than 50V. The onset of leakage currents in the dislocated diode corresponds with the appearance of measurable net generation due to the TAT mechanisms discussed in this work.

IV. Conclusion

In this work, a vertical *p-n* diode with typical doping characteristics and an equivalent threading dislocation density of $10^8\ cm^{-2}$ was modeled in reverse bias. The model in this work uses a previously submitted

model used to model forward bias leakage characteristics and adds an additional mathematical model to account for the effects of defects in high electric fields. The model shows that the dislocation-mediated leakage mechanism for reverse bias leakage in GaN *p*-n diodes is the generation of electron-hole pairs that are swept out of the junction by the reverse bias electric field. This behavior results in a measurable leakage current within the model with behavior consistent with experimental values.

V. Reference Table

The table is arranged in alphabetical order of the description with similar variables grouped together in the table (i.e. conduction, valence, and intrinsic energies are grouped together).

Sym.	Description	Value	Units
k	Boltzmann constant	8.62×10^{-5}	eV / K
σ_n	Capture cross section – electrons	1×10^{-12} [22]	cm^2
σ_p	Capture cross section – holes	1×10^{-12} [22]	cm^2
$\bar{n}$	Capture rate – electrons	N/A	s^{-1}
$\bar{p}$	Capture rate – holes	N/A	s^{-1}
N_A	Concentration – acceptor dopants	5×10^{19}	cm^{-3}
N_D	Concentration – donor dopants	5×10^{17}	cm^{-3}
n	Concentration – electrons	N/A	cm^{-3}
Q_T	Concentration – charged trap states	N/A	
p	Concentration – holes	N/A	cm^{-3}
n_i	Concentration – intrinsic carriers	3.43×10^{-10}	cm^{-3}
N_A^-	Concentration – ionized acceptor dopants	N/A	cm^{-3}
N_{tA}^-	Concentration – ionized acceptor traps	N/A	cm^{-3}
N_D^+	Concentration – ionized donor dopants	N/A	cm^{-3}
N_{tD}^+	Concentration – ionized donor traps	N/A	cm^{-3}
ρ_T	Concentration – trap states*	N/A	cm^{-3}
J_n	Current density – electrons	N/A	A/cm^2
J_p	Current density - holes	N/A	A/cm^2
ϵ_r	Dielectric constant	8.9	---
N_C	Effective density of states – conduction band	2.2×10^{18}	cm^{-3}
N_V	Effective density of states – valence band	4.2×10^{19}	cm^{-3}
m_n^*	Effective mass – electron	1.98×10^{-31} ($0.2m_0$ [41])	Kg
m_p^*	Effective mass – holes	1.28×10^{-30} ($1.4m_0$ [42])	Kg
ψ	Electric potential	N/A	V
q	Electron charge	1.61×10^{-19}	C
e_n	Emission rate – electrons	N/A	s^{-1}

e_p	Emission rate – holes	N/A	s^{-1}
E_A	Energy level – acceptor	0.19 [34]	eV
E_C	Energy level – conduction band edge	N/A	eV
E_D	Energy level – donor	0.025 [34]	eV
E_{Fn}	Energy level – electron quasi-Fermi	N/A	eV
E_{Fp}	Energy level – hole quasi-Fermi	N/A	eV
E_i	Energy level - intrinsic	1.73	eV
E_V	Energy level – valence band edge	N/A	eV
c	Lattice parameter – c-component	5.186	Å
τ_n	Lifetime – electrons	N/A	s
τ_p	Lifetime – holes	N/A	s
μ_n^{maj}	Mobility – majority electrons	400	$\frac{cm^2}{Vs}$
μ_n^{min}	Mobility – minority electrons	32	$\frac{cm^2}{Vs}$
μ_p^{maj}	Mobility – majority holes	8	$\frac{cm^2}{Vs}$
μ_p^{min}	Mobility – minority holes	26	$\frac{cm^2}{Vs}$
ϵ_0	Permittivity of free space	8.85×10^{-14}	F/cm
U	Recombination rate - net	N/A	s^{-1}
U_{SRH}	Recombination rate – Shockley-Read-Hall	N/A	s^{-1}
R_{SC}	Screening radius	N/A	nm
g_n	State degeneracy – conduction band	2	---
g_p	State degeneracy – valence band	4	---
T	Temperature	300	K
v_n	Thermal velocity – electrons	2.60×10^7	cm / s
v_p	Thermal velocity – holes	9.87×10^6	cm / s
$f(E_T)$	Trap state occupancy	N/A	---

VI. References

[1] C. Poblenz, P. Waltereit, S. Rajan, S. Heikman, U.K. Mishra, and J.S. Speck, Journal of Vacuum Science & Technology B: Microelectronics and Nanometer Structures Processing, Measurement, and Phenomena **22**, 1145 (2004).
[2] U.K. Mishra, L. Shen, T.E. Kazior, and Y.F. Wu, Proceedings of the IEEE **96**, 287 (2008).
[3] D. Denninghoff, J. Lu, M. Laurent, E. Ahmadi, S. Keller, and U.K. Mishra, in *70th Device Research Conference* (2012), pp. 151–152.
[4] S.W. Kaun, M.H. Wong, U.K. Mishra, and J.S. Speck, Semicond. Sci. Technol. **28**, 074001 (2013).
[5] B. Romanczyk, S. Wienecke, M. Guidry, H. Li, E. Ahmadi, X. Zheng, S. Keller, and U.K. Mishra, IEEE Transactions on Electron Devices **65**, 45 (2018).
[6] T. Nishida, T. Makimoto, H. Saito, and T. Ban, Appl. Phys. Lett. **84**, 1002 (2004).
[7] P. Waltereit, H. Sato, C. Poblenz, D.S. Green, J.S. Brown, M. McLaurin, T. Katona, S.P. DenBaars, J.S. Speck, J.-H. Liang, M. Kato, H. Tamura, S. Omori, and C. Funaoka, Appl. Phys. Lett. **84**, 2748 (2004).
[8] R. Sharma, P.M. Pattison, H. Masui, R.M. Farrell, T.J. Baker, B.A. Haskell, F. Wu, S.P. DenBaars, J.S. Speck, and S. Nakamura, Appl. Phys. Lett. **87**, 231110 (2005).
[9] H. Sato, A. Tyagi, H. Zhong, N. Fellows, R.B. Chung, M. Saito, K. Fujito, J.S. Speck, S.P. DenBaars, and S. Nakamura, Physica Status Solidi (RRL) – Rapid Research Letters **1**, 162 (2007).
[10] A. Tyagi, R.M. Farrell, K.M. Kelchner, C.-Y. Huang, P.S. Hsu, D.A. Haeger, M.T. Hardy, C. Holder, K. Fujito, D.A. Cohen, H. Ohta, J.S. Speck, S.P. DenBaars, and S. Nakamura, Appl. Phys. Express **3**, 011002 (2009).
[11] D.A. Haeger, E.C. Young, R.B. Chung, F. Wu, N.A. Pfaff, M. Tsai, K. Fujito, S.P. DenBaars, J.S. Speck, S. Nakamura, and D.A. Cohen, Appl. Phys. Lett. **100**, 161107 (2012).
[12] S. Lee, C.A. Forman, C. Lee, J. Kearns, E.C. Young, J.T. Leonard, D.A. Cohen, J.S. Speck, S. Nakamura, and S.P. DenBaars, Appl. Phys. Express **11**, 062703 (2018).
[13] Y. Hatakeyama, K. Nomoto, N. Kaneda, T. Kawano, T. Mishima, and T. Nakamura, IEEE Electron Device Letters **32**, 1674 (2011).
[14] I.C. Kizilyalli, A.P. Edwards, H. Nie, D. Disney, and D. Bour, IEEE Transactions on Electron Devices **60**, 3067 (2013).
[15] T. Oka, T. Ina, Y. Ueno, and J. Nishii, Appl. Phys. Express **8**, 054101 (2015).
[16] O. Aktas and I.C. Kizilyalli, IEEE Electron Device Letters **36**, 890 (2015).
[17] J.R. Dickerson, A.A. Allerman, B.N. Bryant, A.J. Fischer, M.P. King, M.W. Moseley, A.M. Armstrong, R.J. Kaplar, I.C. Kizilyalli, O. Aktas, and J.J. Wierer, IEEE Transactions on Electron Devices **63**, 419 (2016).
[18] Y. Yoshizumi, S. Hashimoto, T. Tanabe, and M. Kiyama, Journal of Crystal Growth **298**, 875 (2007).
[19] M. Qi, K. Nomoto, M. Zhu, Z. Hu, Y. Zhao, V. Protasenko, B. Song, X. Yan, G. Li, J. Verma, S. Bader, P. Fay, H.G. Xing, and D. Jena, Applied Physics Letters **107**, 232101 (2015).
[20] S. k. Mathis, A. e. Romanov, L. f. Chen, G. e. Beltz, W. Pompe, and J. s. Speck, Phys. Stat. Sol. (a) **179**, 125 (2000).
[21] S.K. Mathis, A.E. Romanov, L.F. Chen, G.E. Beltz, W. Pompe, and J.S. Speck, Journal of Crystal Growth **231**, 371 (2001).
[22] D.C. Look, G.C. Farlow, P.J. Drevinsky, D.F. Bliss, and J.R. Sizelove, Applied Physics Letters **83**, 3525 (2003).
[23] E.C.H. Kyle, S.W. Kaun, P.G. Burke, F. Wu, Y.-R. Wu, and J.S. Speck, Journal of Applied Physics **115**, 193702 (2014).
[24] D. Cherns, C. g. Jiao, H. Mokhtari, J. Cai, and F. a. Ponce, Phys. Stat. Sol. (b) **234**, 924 (2002).
[25] I. Arslan and N.D. Browning, Phys. Rev. B **65**, 075310 (2002).
[26] E. Müller, D. Gerthsen, P. Brückner, F. Scholz, Th. Gruber, and A. Waag, Phys. Rev. B **73**, 245316 (2006).
[27] Z. Zhang, A.R. Arehart, E.C.H. Kyle, J. Chen, E.X. Zhang, D.M. Fleetwood, R.D. Schrimpf, J.S. Speck, and S.A. Ringel, Applied Physics Letters **106**, 022104 (2015).
[28] D.C. Look and J.R. Sizelove, Phys. Rev. Lett. **82**, 1237 (1999).

[29] C.A. Robertson, K.S. Qwah, Y.-R. Wu, and J.S. Speck, Journal of Applied Physics **126**, 245705 (2019).
[30] K. Kumakura, T. Makimoto, N. Kobayashi, T. Hashizume, T. Fukui, and H. Hasegawa, Applied Physics Letters **86**, 052105 (2005).
[31] K.C. Collins, A.M. Armstrong, A.A. Allerman, G. Vizkelethy, S.B. Van Deusen, F. Léonard, and A.A. Talin, Journal of Applied Physics **122**, 235705 (2017).
[32] S. Hafiz, F. Zhang, M. Monavarian, V. Avrutin, H. Morkoç, Ü. Özgür, S. Metzner, F. Bertram, J. Christen, and B. Gil, Journal of Applied Physics **117**, 013106 (2015).
[33] Z.Z. Bandić, P.M. Bridger, E.C. Piquette, and T.C. McGill, Solid-State Electronics **44**, 221 (2000).
[34] M. Leroux, N. Grandjean, B. Beaumont, G. Nataf, F. Semond, J. Massies, and P. Gibart, Journal of Applied Physics **86**, 3721 (1999).
[35] R.C. Jaeger and F.H. Gaensslen, IEEE Transactions on Electron Devices **27**, 914 (1980).
[36] J.G. Simmons and G.W. Taylor, Phys. Rev. B **4**, 502 (1971).
[37] W. Shockley, The Bell System Technical Journal **28**, 435 (1949).
[38] W. Shockley and W.T. Read, Phys. Rev. **87**, 835 (1952).
[39] C.T. Sah, Phys. Rev. **123**, 1594 (1961).
[40] D. Rosenfeld and G. Bahir, IEEE Transactions on Electron Devices **39**, 1638 (1992).
[41] Q.K. Yang, F. Fuchs, J. Schmitz, and W. Pletschen, Appl. Phys. Lett. **81**, 4757 (2002).
[42] C.A. Hurni, O. Bierwagen, J.R. Lang, B.M. McSkimming, C.S. Gallinat, E.C. Young, D.A. Browne, U.K. Mishra, and J.S. Speck, Applied Physics Letters **97**, 222113 (2010).
[43] Z.-Q. Fang, D.C. Look, D.H. Kim, and I. Adesida, Appl. Phys. Lett. **87**, 182115 (2005).
[44] I. Vurgaftman, J.R. Meyer, and L.R. Ram-Mohan, Journal of Applied Physics **89**, 5815 (2001).
[45] A. Kasic, M. Schubert, S. Einfeldt, D. Hommel, and T.E. Tiwald, Phys. Rev. B **62**, 7365 (2000).

Chapter 4 : Indium as a surfactant: Effects on growth morphology and background impurity in GaN films grown by ammonia-assisted molecular beam epitaxy

4.1 Introduction

Over the past few decades, III-nitride materials have gained tremendous attention for many different areas including optoelectronics and power electronics. In optoelectronics, having a direct bandgap ranging from 0.7 eV to over 6 eV has resulted in light sources in wide variety of wavelengths from infrared[1] to deep ultra violet[2]. In power electronics, III-nitride binary and alloy systems such as GaN and AlGaN are favorable over the conventional narrower gap materials, such as Si and GaAs due to reasonable carrier mobility and higher breakdown field that results in larger Baliga's figure of merit.[3]

Since the demonstration of III-nitride based transistors and diodes[3,4], their progress is limited by different challenges, one of which includes the presence of extended defects such as high densities of threading dislocations in the material grown on lattice-mismatched foreign substrates, which results in the degradation of device performance. This is demonstrated for GaN *p-n* diodes, in which threading dislocations behave as leakage pathways under both forward and reverse biases[5,6]. In addition to this, high-voltage power switches require thick drift regions (on the order of 10 μm) with low background doping levels (on the order of $10^{15} – 10^{16}$ cm^{-3}) to realize high blocking voltages[3]. Hence, there is also a need for growth methods and optimized conditions to enhance the growth rate, maintaining the low background doping[7]. Another challenge is related to selective-area doping for bipolar devices such as junction field-effect transistors (JFETs) and current aperture vertical electron transistors (CAVETs) which requires etched-and-regrown interfaces, resulting in large densities of etch-induced defects and impurities resulting from ambient exposure at the regrowth junction[8,9].

Some specialized devices, such as vertical fin field-effect transistors (FinFETs) and simpler devices such as Schottky barrier diodes (SBDs), which are unipolar in nature, do not require selective-area-doping.

However, the processing of FinFETs requires selective wet etching of the sidewalls with potassium hydroxide (KOH)[10]. Upon wet etching, the V-defects that are present on the surface could increase in size and depth, providing more leakage paths through the low-doped n^- drift regions[11]. Vertical FinFETs and SBDs require thick drift regions and should also be grown at high growth rates (~1 μm/hour) such that the growth can be realized in a reasonable time. However, increased growth rates could result in increased surface roughness, V-defect density, and background impurity concentration, all of which are detrimental to the device performance[7].

To improve the surface morphology in epitaxial growth, surfactants are commonly employed. For the case of group III nitrides, indium has been shown to be a highly effective surfactant. Typically, surfactants alter the surface morphology by modifying the surface energy and/or the adatom mobility[12]. One example of using indium as a surfactant was the application of trimethylindium as a source of indium, which has demonstrated to facilitate step-flow growth of AlN and AlGaN by metal-organic chemical vapor deposition (MOCVD), producing high quality conductive films[13–15]. In addition, indium has also been used in the plasma-assisted molecular beam epitaxy (PAMBE) growth of non-polar $(10\bar{1}0)$ AlGaN/InGaN multi-quantum well heterostructures[16]. Finally, indium has also resulted in improved surface morphology and *p*-type conductivity in Mg-doped *p*-GaN grown by ammonia-assisted molecular beam epitaxy (NH_3-MBE)[17].

Despite the observed advantages of using indium surfactant for growth of GaN and AlN, the indium surfactant has not been reported for NH_3-MBE growth of unintentionally doped (UID) GaN under fast growth rates (practical for device applications with thick drift regions). In addition to controllably low background impurities[7], high material quality and high interface abruptness[18], the NH_3-MBE growth method has an additional advantage of higher doping in the n^{++} layer required for improved source contacts (resulting in a reduced on-resistance) beneficial for the vertical GaN power transistors and diodes. We report on the effects of indium as a surfactant and other growth conditions on the surface morphology during NH_3-MBE growth of unintentionally doped (UID) GaN under fast growth rates (1 μm/hour). The improvements in the surface morphology while maintaining low background impurity levels for fast growth

rates would provide a path toward high-quality thick drift regions growths with smooth morphologies for regrowth-free high-voltage vertical devices for power switching applications.

4.2 Experimental Procedure

The structures consisted of 1 µm-thick UID GaN grown at ~1 µm/hour as shown in Figure 46: (a) Simple cross-sectional schematic of the structure. (b) HRXRD ω-2θ scan of a calibration sample . All samples were grown using a Veeco Gen 930 NH_3-MBE on 1 cm^2 MOCVD-grown GaN-on-Sapphire templates from Lumilog Saint-Gobain. To facilitate heat conduction from the heating filament, the substrates were coated with a Titanium/Palladium/Titanium (50/500/100 nm) metal stack on the backside. This also enables us to accurately monitor the surface temperature using an optical pyrometer that is calibrated to the emissivity of the backside metal stack. The samples were then cleaned by immersing in acetone, methanol and isopropanol for three minutes each under sonication. They were then loaded onto the system to be baked at 400 °C for one hour. During growth, elemental gallium and indium were supplied using dual filament effusion cells. Atomic force microscopy (AFM) was used to evaluate the film surface morphology. The surface roughness was quantified using root-mean-square (RMS) roughness calculated from the AFM scans. Apart from that, secondary ions mass spectroscopy (SIMS) was also conducted to determine the background impurity levels (mainly Oxygen and Silicon) of the UID GaN layers. Thicknesses and growth rates were confirmed by evaluating thickness fringes from high-resolution X-ray diffraction (HRXRD) scans on separate calibration samples (Figure *46*(b)).

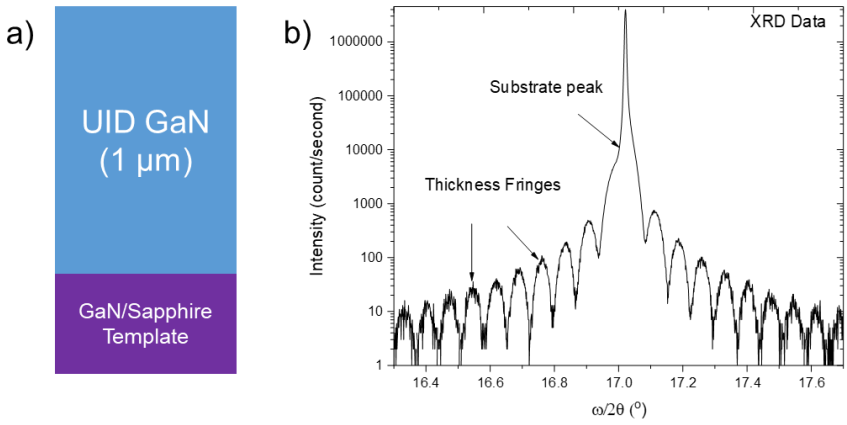

Figure 46: (a) Simple cross-sectional schematic of the structure. (b) HRXRD ω-2θ scan of a calibration sample for growth rate evaluation.

Sample	Temperature (°C)	NH_3 flow rate (sccm)	V/III Ratio	Indium Flux BEP (Torr)	RMS roughness (nm)	Substrate	Notes
1A	800	200	700	0	2.58	STINS	
1B	800	200	700	5×10^{-8}	1.78	STINS	
1C	800	200	700	1×10^{-7}	1.71	STINS	
1D	800	200	700	5×10^{-7}	2.51	STINS	
2A	780	200	700	5×10^{-8}	1.32	STINS	
2B	800	500	2000	5×10^{-8}	1.78	STINS	
2C	820	750	3200	5×10^{-8}	1.95	STINS	
2D	780	200	700	5×10^{-8}	0.81	STINS	
2E	800	500	2000	5×10^{-8}	0.69	STINS	
2F	820	750	3200	5×10^{-8}	1.42	STINS	
2G	780	200	700	5×10^{-8}	0.82	STINS	
2H	800	500	2000	5×10^{-8}	0.93	STINS	
2I	820	750	3200	5×10^{-8}	0.94	STINS	
3A	800	750	3200	0	1.10	STINS	
3B	800	750	3200	5×10^{-8}	0.90	STINS	
3C	800	750	3200	1×10^{-7}	0.94	STINS	
3D	800	750	3200	5×10^{-7}	1.49	STINS	
4A	800	500	2000	0		FS GaN	C-V device
4B	800	500	2000	5×10^{-8}		FS GaN	C-V device
5	800	750	3200	5×10^{-8}	0.21	FS GaN	FinFET test

Table 10 : Summary table for all the samples grown for this investigation

Table 10 summarizes all the samples grown in this investigation. In the first sample series (samples 1A, 1B, 1C and 1D) In surfactant flux beam equivalent pressure (BEP) was changed, while keeping the substrate temperature (800 °C) and the NH_3 flow rate (200 sccm) constant. While the indium flux BEPs were varied (0 Torr, 5×10^{-8} Torr, 1×10^{-7} Torr and 5×10^{-7} Torr), the Ga flux was fixed at a BEP of 4×10^{-7} Torr.

4.3 Results and Discussion

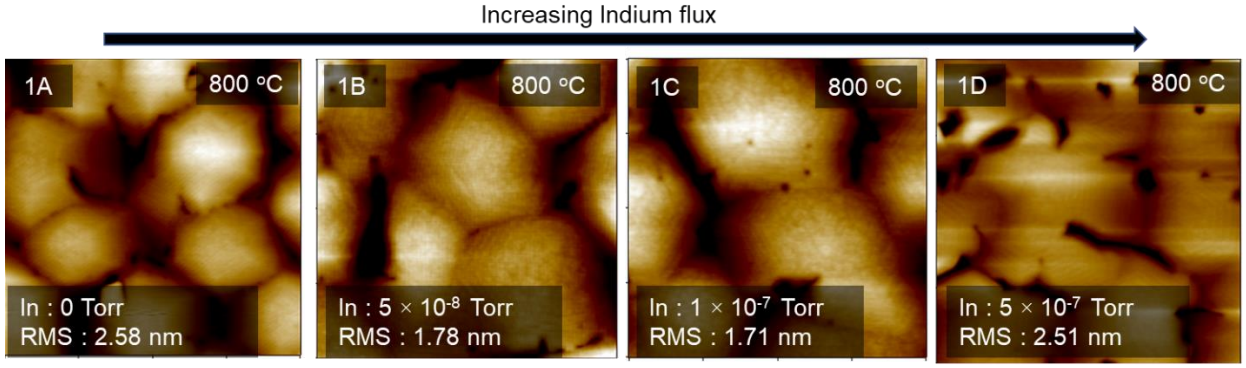

Figure 47: 2 × 2 μm AFM scans for 1 μm-thick UID GaN grown with indium flux BEPs of (a) 0, (b) 5×10^{-8} Torr, (c) 1×10^{-7} Torr, and (d) 5×10^{-7} Torr at 800C and an NH_3 flow rate of 200 sccm.

Figure 47 compares the AFM results of the first sample series, indicating a clear effect of indium on the surface morphology. Adding the indium increased the widths of the terraces due to the enhanced Ga adatom mobility because of indium atoms acting as surfactants. The hillock surface feature increases in size and the RMS roughness was reduced by increasing the indium flux up to a BEP of 1×10^{-7} Torr (Figure 47(a) to (c)). However, as the indium flux was increased beyond the indium flux of 1×10^{-7} Torr, the surface starts to deteriorate, and deep elongated features start to form at an indium flux of 1×10^{-7} Torr (Figure 47(d)) and become very significant at 5×10^{-7} Torr.

The improvements in the surface morphology upon introducing the indium surfactant was not very significant in the first series. Hence, we suspected that our growth conditions were not optimized for the fast growth rate of 1 μm/hour. At temperatures well above the decomposition temperature of GaN at 500 °C, a higher V/III ratio is necessary to suppress it[19]. Thus, with a higher Ga flux, a higher NH_3 flow was necessary[19]. Besides that, the substrate temperature for fast growth rates, in the presence of indium surfactant, may also need optimization to make the most use of the improve in the adatom mobility. Following the initial first series, a separate series of samples were grown to optimize the growth conditions. Therefore, we varied the NH_3 flow rate as well as the substrate temperature, while keeping the indium flux BEP fixed at 5×10^{-8} Torr (Sample 1B). The NH_3 flow rates were varied from 200 sccm, to 500 sccm and

750 sccm, whereas the temperatures were varied from 780 °C, to 800 °C and 820 °C. A detailed description of the samples are given in Table 1.

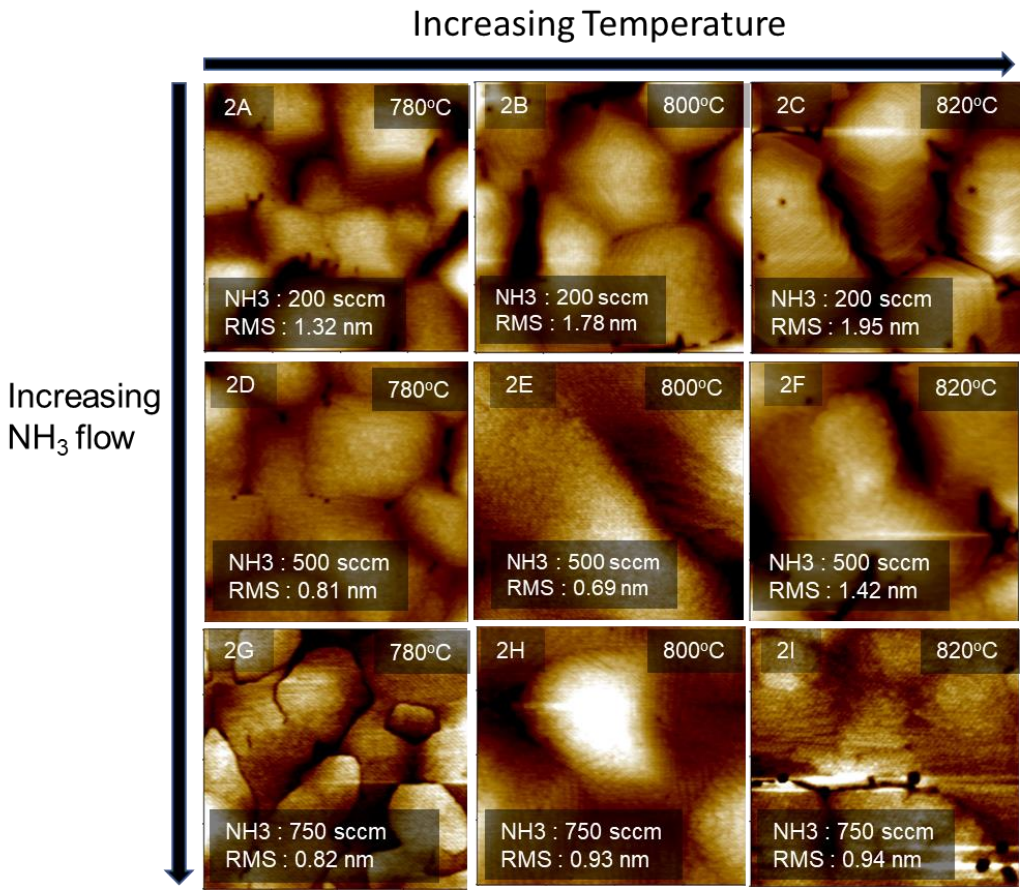

Figure 48: 2 × 2 μm AFM scans for 1 μm-thick UID GaN grown with a indium flux BEP of 5×10^{-8} Torr under different growth temperature and NH_3 flow rates (V/III ratio).

Figure 48 compares the surface morphologies of the samples grown at different substrate temperatures and NH_3 flow rates (different V/III ratios). The surface morphology improved, and the RMS roughness values reduced by increasing the NH_3 flow rate for samples grown at 780 and 800 °C. However, for the higher growth temperature of 820 °C, the roughness values slightly increased for sample 2I (~1.5 nm) compared to sample 2H (~0.9 nm). This meant that the optimum substrate temperature of 800 °C and NH_3 flow rate of 750 sccm resulted in the lowest density of pits and the smoothest morphology.

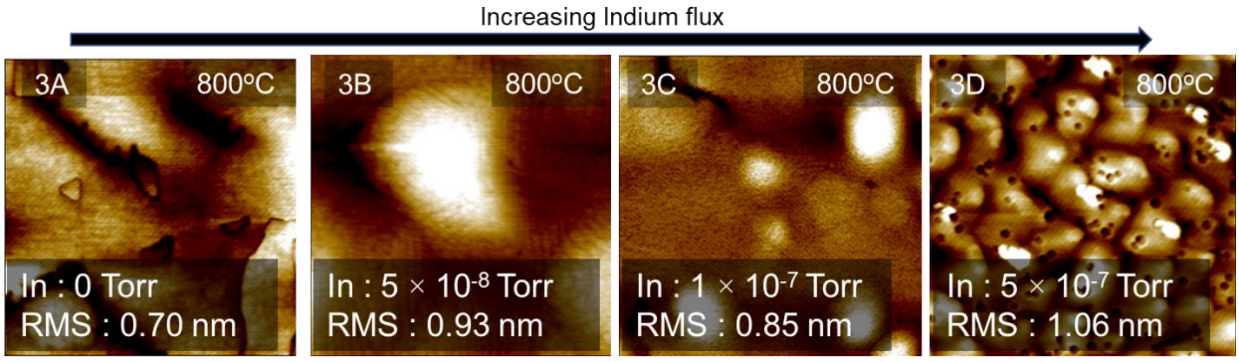

Figure 49: 2 × 2 μm AFM scans for 1 μm-thick UID GaN grown under optimized temperature of 800 °C and NH_3 flow rate of 750 sccm with indium flux BEPs of (a) 0, (b) 5×10^{-8} Torr, (c) 1×10^{-7} Torr, and (d) 5×10^{-7} Torr.

Another sample series was grown to study the impacts of indium surfactant flux using the optimal growth conditions (800 °C and 750 sccm of NH_3), using an identical indium flux as used in the initial series. Figure 49 compares AFM scans for the samples grown under different indium flux under the optimum temperature and V/III ratio. The results confirm an optimal indium flux BEP value of 5×10^{-8} Torr (Figure 49(b)) corresponding to the RMS roughness value of 0.93 nm. The results indicate a strong effect of indium surfactant on the surface morphology under the optimized condition. The reason for this is due to indium improving the adatom mobilities of both Ga and N on the surface. Neugebauer *et al.* conducted density functional theory (DFT) calculations to study the effect of an indium adlayer on the diffusion barriers of Ga and N adatoms. The study found that, in both cases, the diffusion barrier is lower with an In-adlayer when compared to a bare surface.[20]

The excessive amount of indium surfactant could also result in surface degradation (Figure 49(c) and Figure 49(d)). This has been observed by other studies[17,21] and was theorized due to the NH_3 reacting with the indium, preventing the gallium atoms from reacting to the NH_3 on the surface during growth[21]. Due to the reaction of NH_3 to the excess indium on the surface, the gallium atoms are unable to incorporate into the crystal, leading to the deterioration of the crystal surface observed here on Figure 49(c) and 4(d). This is also possibly due to the stabilization of the $(10\bar{1}1)$ plane, which are the sidewall planes for V-defects.

First principle calculations by Northrup and Neugebauer[12] show that In atoms reduce the formation energy of the $(10\bar{1}1)$ plane relative to the (0001) plane.

To evaluate the impact of indium as a surfactant on any potential impurity incorporating in the GaN films, a series of secondary ions mass spectroscopy (SIMS) measurements were performed to track the background Si and O concentrations. Figure 50 compares the oxygen (Figure 50(a)), indium (Figure 50 (b)) and silicon (Figure 50(c)) SIMS profiles for the samples grown with 0, 5×10^{-8} and 1×10^{-7} Torr indium BEPs. According to the data of Figure 50, the O background level is independent of change in the indium BEP (note the different background O levels for the substrate below the regrowth junctions for the three samples, which remain the same for the regrown layers for all three samples). Besides that, the indium concentration is higher in the sample grown with the higher indium flux. However, the indium concentration is significantly below the alloying level and should just behave as a dilute isoelectronic impurity. The background Si, however, shows a slight decrease with the increase in indium flux. The slight reduction of Si background impurity levels with the increase in the indium BEP may be explained by the surface being saturated with In atoms, preventing Si from incorporating to the film.

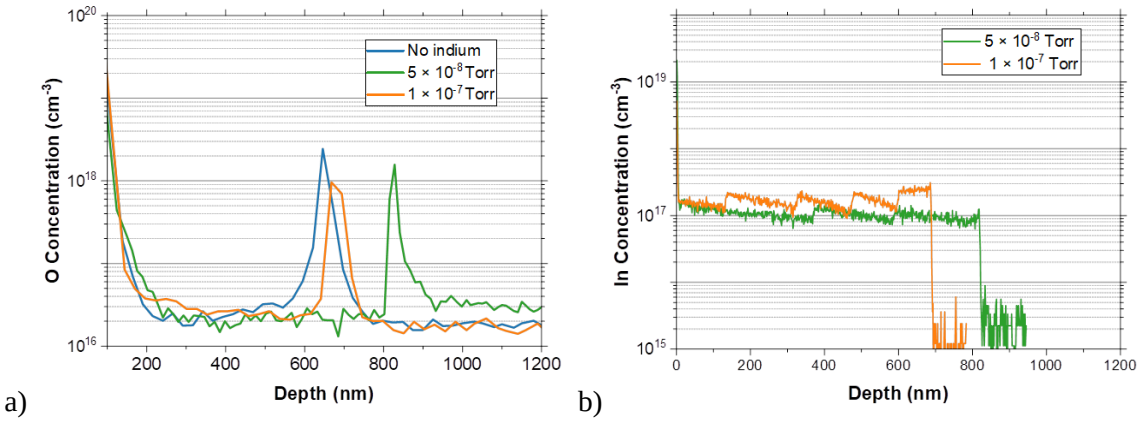

a) b)

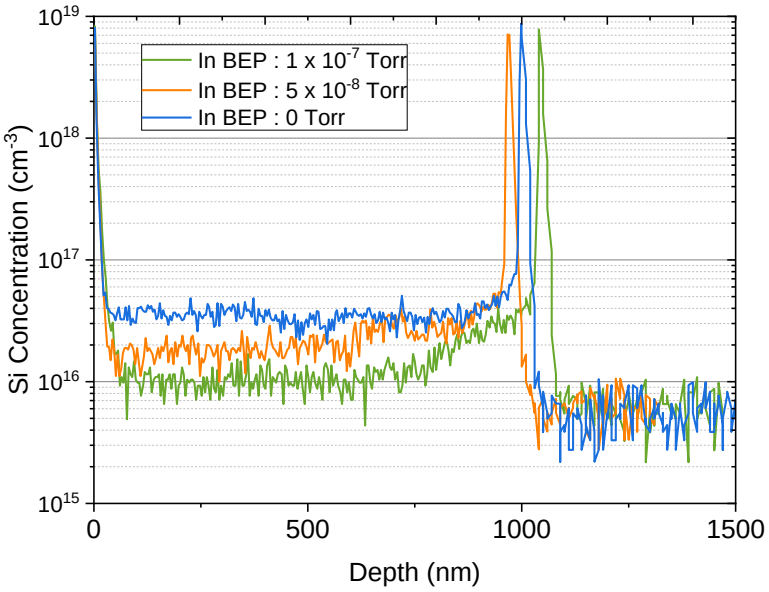

c)

Figure 50: SIMS Impurity profiles for (a) O, (b) In and (c) Si for different indium surfactant flux BEPs of 0, 5×10^{-8} and 1×10^{-7} Torr.

In addition to SIMS measurements, capacitance-voltage (C-V) devices (Sample 4A and 4B) were grown and fabricated. These devices consist of a 3 µm layer of UID-GaN followed by 300 nm of *n*-type GaN, with a silicon concentration of ~5×10^{-19} cm^{-3} on top of a Mitsubishi Chemical Corporation (MCC) free-standing GaN substrate. Finally, 8 nm Schottky nickel contacts were deposited on the top of the mesa and ohmic titanium/gold contacts (30/150 nm) were deposited on the backside. A schematic of the structure is shown on Figure 51(a). C–V measurements were then conducted at 1 MHz frequency on the samples using a Keithley B4200 parameter analyzer to obtain the net doping (N_D^+–N_A^-) in the structure, as plotted on Figure 51(b).

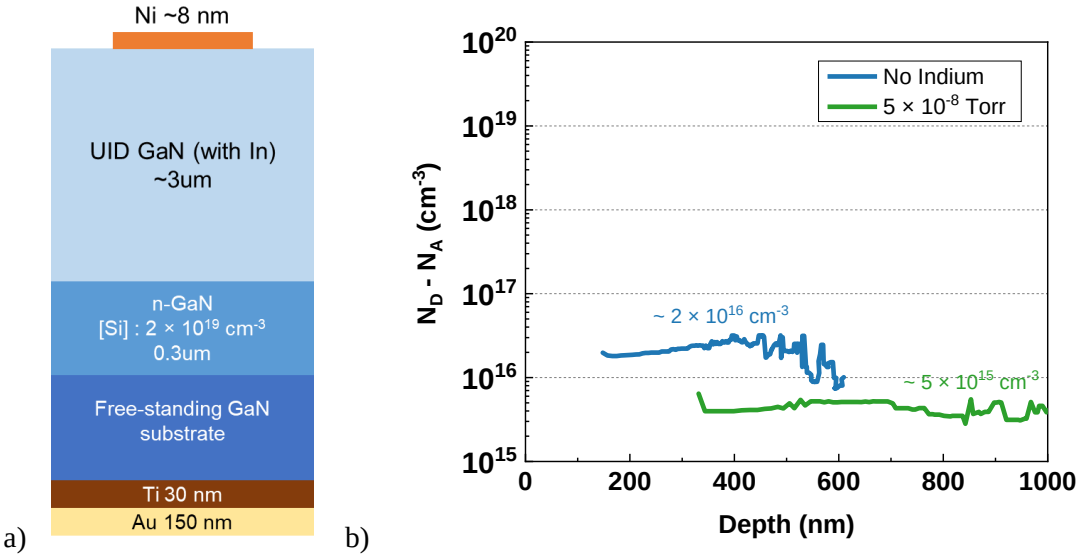

Figure 51: (a) Schematic of the device (Sample 4A and 4B) b) A plot of the net doping vs the depth in the structure for different growth conditions

According to the net doping plots obtained from C-V measurements, it can be clearly seen that having indium as a surfactant during growth lowers the background doping in the film by a factor of four, which is a significant reduction. This reduction in net donor concentration is suspected to be due to the Indium adlayer preventing the incorporation of silicon in the film during growth, which is consistent with reduced silicon incorporation shown in Fig. 5 with increasing indium flux during growth. Apart from that, it could also be the Indium adlayer facilitating the desorption of silicon on the surface. Further research on the mechanism of this behavior will be conducted in future studies.

To test the growth condition, a test structure of *n*+/*n*-/*n*+ (schematically shown in Figure 6(a)) (designed for vertical FinFET processes) was then grown to test the conditions for a thick drift region. The structure consists of a 1 µm-thick Si-doped *n*+ region ([Si]: 5×10^{19} cm^{-3}), followed by a 2 µm-thick UID GaN drift layer and capped by another 300 nm *n*+ layer ([Si]: 5×10^{19} cm^{-3}), grown on a *c*-plane free-standing bulk GaN substrate from the Mitsubishi Chemical Corporation. The test structure uses the conditions from Sample 3C, which is an NH_3 flow of 750 sccm, a substrate temperature of 800 °C and an indium BEP flux of 5×10^{8} Torr. The AFM scans for the structures are shown in Figure 52.

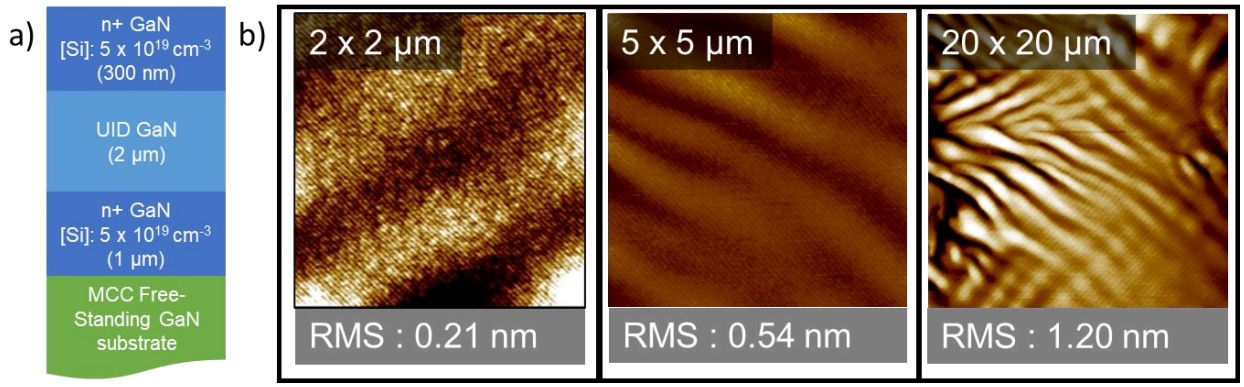

Figure 52: (a) Cross-sectional schematic of the n+/n-/n+ vertical FinFET test structure (Sample 5). (b) AFM scans of the surface of the FinFET test structure for different scan sizes, indicating an atomically flat surface.

The AFM data of Figure 52 shows an atomically-flat surface, with a minimum surface RMS roughness of ~ 0.21 nm for small scan sizes, despite the anti-surfactant properties of silicon during GaN growth[22,23], which normally results in surface deterioration for high silicon doping. In addition, there are no observable hillocks or pits on the sample surface. The absence of pits is also partially attributed to the choice of substrate for this structure, as the free-standing GaN substrates have lower threading dislocations (~10^6 cm^{-2}) as compared to GaN-on-sapphire templates (~10^8 cm^{-2}). It is worth noting here that, the threading dislocations are usually where the V-defects start to nucleate and they usually form along the opening of these dislocations[24].

4.3 Conclusion

In conclusion, we present the surfactant properties of indium during the epitaxial growth of UID GaN by NH_3-MBE under fast growth rates. The introduction of indium surfactant increased the widths of atomic terraces, but excessive indium resulted in a degraded surface. A combination of the optimum indium surfactant BEP flux, growth temperature and V/III ratio resulted in sub-nanometer RMS roughnesses and resulted in atomically flat surfaces for the *n*+/*n*-/*n*+ test structure. The introduction of indium surfactant also resulted in the reduction in the background silicon level, confirmed by both SIMS and C-V measurements, which is also helpful in reducing the background doping levels for high-blocking voltages while keeping the O level unchanged. The combination of fast growth rate, high-quality material enabled by NH_3-MBE growth, possibility of high doping in *n*+ layer maintaining the smooth morphology for the source contact, low background doping levels in the *n*- drift regions, and smooth morphologies are promising for vertical power switches with high blocking voltages and low on-resistance based on vertical FinFET designs and beyond.

4.4 Acknowledgments

The information, data, or work presented herein was funded, in part, by the Advanced Research Projects Agency—Energy (ARPA-E), Collaborative Research in Engineering, Science and Technology (CREST), U.S. Department of Energy (DOE), under the PNDIODES program directed by Dr. Isik Kizilyalli. The work was also partially supported by the Simons Foundation (Grant No. 601952, J.S.S.) and Air Force Office of Scientific Research (Program No. FA9550-19-1-10090). A portion of this work was performed at the UCSB CNSI-Nanofabrication facility.

4.5 References

[1] M. Monavarian, J. Xu, M.N. Fireman, N. Nookala, F. Wu, B. Bonef, K.S. Qwah, E.C. Young, M.A. Belkin, and J.S. Speck, Appl. Phys. Lett. **116**, 201103 (2020).
[2] B.K. SaifAddin, A.S. Almogbel, C.J. Zollner, F. Wu, B. Bonef, M. Iza, S. Nakamura, S.P. DenBaars, and J.S. Speck, ACS Photonics **7**, 554 (2020).
[3] I.C. Kizilyalli, A.P. Edwards, O. Aktas, T. Prunty, and D. Bour, IEEE Transactions on Electron Devices **62**, 414 (2015).
[4] Y.-F. Wu, D. Kapolnek, J.P. Ibbetson, P. Parikh, B.P. Keller, and U.K. Mishra, IEEE Transactions on Electron Devices **48**, 586 (2001).
[5] C.A. Robertson, K.S. Qwah, Y.-R. Wu, and J.S. Speck, Journal of Applied Physics **126**, 245705 (2019).
[6] K.S. Qwah, C.A. Robertson, Y.-R. Wu, and J.S. Speck, Semiconductor Science and Technology **36**, 075001 (2021).
[7] J. Wang, K.F. Jorgensen, E. Farzana, K.S. Qwah, M. Monavarian, Z.J. Biegler, T. Mates, and J.S. Speck, APL Materials **9**, 081118 (2021).
[8] I. Stricklin, M. Monavarian, A. Aragon, G. Pickrell, M. Crawford, A. Allerman, A. Armstrong, and D. Feezell, in *Wide Bandgap Power and Energy Devices and Applications III*, edited by M. Matin, S. Chowdhury, and A.K. Dutta (SPIE, 2018), pp. 1–10.
[9] K. Fu, H. Fu, X. Huang, T.-H. Yang, C.-Y. Cheng, P.R. Peri, H. Chen, J. Montes, C. Yang, J. Zhou, X. Deng, X. Qi, D.J. Smith, S.M. Goodnick, and Y. Zhao, IEEE Journal of the Electron Devices Society **8**, 74 (2020).
[10] L. Lu, Z.Y. Gao, B. Shen, F.J. Xu, S. Huang, Z.L. Miao, Y. Hao, Z.J. Yang, G.Y. Zhang, X.P. Zhang, J. Xu, and D.P. Yu, Journal of Applied Physics **104**, 123525 (2008).
[11] S. Besendörfer, E. Meissner, A. Tajalli, M. Meneghini, J.A. Freitas, J. Derluyn, F. Medjdoub, G. Meneghesso, J. Friedrich, and T. Erlbacher, Journal of Applied Physics **127**, 015701 (2020).
[12] J.E. Northrup and J. Neugebauer, Phys. Rev. B **60**, R8473 (1999).
[13] S. Keller, S. Heikman, I. Ben-Yaacov, L. Shen, S. DenBaars, and U. Mishra, Physica Status Solidi (a) **188**, 775 (2001).
[14] A.S. Almogbel, C.J. Zollner, B.K. Saifaddin, M. Iza, J. Wang, Y. Yao, M. Wang, H. Foronda, I. Prozheev, F. Tuomisto, A. Albadri, S. Nakamura, S.P. DenBaars, and J.S. Speck, AIP Advances **11**, 095119 (2021).
[15] C.J. Zollner, Y. Yao, M. Wang, F. Wu, M. Iza, J.S. Speck, S.P. DenBaars, and S. Nakamura, Crystals **11**, 1006 (2021).
[16] B. Dzuba, A. Senichev, T. Nguyen, Y. Cao, R.E. Diaz, M.J. Manfra, and O. Malis, Journal of Applied Physics **128**, 115701 (2020).
[17] E.C.H. Kyle, S.W. Kaun, E.C. Young, and J.S. Speck, Applied Physics Letters **106**, 222103 (2015).
[18] H. Asahi and Y. Horikoshi, *Molecular Beam Epitaxy: Materials and Applications for Electronics and Optoelectronics* (John Wiley & Sons, 2019).
[19] M. Mesrine, N. Grandjean, and J. Massies, Applied Physics Letters **72**, 350 (1998).
[20] J. Neugebauer, T.K. Zywietz, M. Scheffler, J.E. Northrup, H. Chen, and R.M. Feenstra, Phys. Rev. Lett. **90**, 056101 (2003).
[21] A. Fan, X. Zhang, Z. Wu, J. Zhao, S. Chen, H. Chen, A. Nasir, and Y. Cui, Superlattices and Microstructures **130**, 396 (2019).
[22] A.L. Rosa, J. Neugebauer, J.E. Northrup, C.-D. Lee, and R.M. Feenstra, Applied Physics Letters **80**, 2008 (2002).
[23] J. Neugebauer, Physica Status Solidi (c) **n/a**, 1651 (2003).
[24] M. Shiojiri, C.C. Chuo, J.T. Hsu, J.R. Yang, and H. Saijo, Journal of Applied Physics **99**, 073505 (2006).

Appendix

Investigation of GaN-based tunnel junctions with low voltage drops: Impacts of doping levels, ambient exposure, and treatments

I. Introduction

Inter-band tunneling phenomenon in degenerately doped *p*-*n* junctions has been employed in a large number of III-nitride devices, including light-emitting diodes (LEDs), lasers, tunnel field-effect transistors, and multi-junction solar cells[1–5]. The degenerately doped *p*-*n* junctions, also called tunnel junctions (TJs), were first reported by Esaki[6] in Ge systems. Later on, the development of buried TJs were initiated to serve as contact layers in InGaAs and InP material systems to improve the electrical performance of vertical-cavity surface-emitting lasers (VCSELs)[7,8]. More recently for GaN-based LEDs and lasers, TJs have been mainly used to improve the current spreading and to develop low-resistance ohmic contacts to the *p*-type material[1]. In addition to device applications, TJs can also be used in structure designs for fundamental physical investigations[9–11]. For example, fundamental hole transport studies for various electronic and optoelectronic applications require unipolar transport designs to avoid the complexities associated with the recombination process[9]. To avoid the issues with current spreading and possible etch-induced damage to the *p*-layer (which will affect *p*-contacts as well) in the transport structures, TJs with low voltage penalties are required[9]. However, due to the wide bandgap and limited solubility of dopants in GaN, III-nitride material system still lacks reasonably low-loss TJs.

Various research groups have investigated GaN-based TJs for device applications. Jeon *et al.*[12] demonstrated that a buried TJ on top of an InGaN/GaN multiple quantum well (MQW) blue LED[12] , although adding a voltage penalty, which is the added voltage, could enhance the output power of the LEDs by nearly factor two compared to a reference LED with standard *p*-contact. Yonkee *et al.* [13] also reported TJ contacts on LEDs using a hybrid growth approach, where the *p*-

side was grown by metal-organic chemical vapor deposition (MOCVD) and the *n*-side was grown by ammonia molecular-beam epitaxy (NH_3-MBE)[13]. Compared to reference LEDs, the reported LEDs with TJs contact and current spreading layer operate at a forward voltage, ie. 4.5 V versus 5 V at 20 A/cm^2 for the TJ LEDs and reference LEDs respectively. It was also shown that the tunnel junction LEDs had higher peak quantum efficiency at lower current densities, J , with the peak EQE at 38% versus 30% for the reference LED [13]. Akyol *et al.*[14] also investigated the effects of doping on the voltage penalty induced by the TJs using N_2 plasma-assisted molecular beam epitaxy (PAMBE)[14]. Despite the numerous studies reported for GaN TJs thus far, the voltage penalty still needs to be improved for improved device performance. Further improvements of GaN-based TJs for low voltage drops would require a systematic optimization and an in-depth understanding of the space charge region. For instance, understanding the impact of unintentional impurities and native defects at the TJ interface on the drop voltages may shed light on the limitations of the inter-band tunneling rates in such structures. In our case, we are interested in using these tunnel junctions as a current spreading layer to enable our studies on *p*-type heterostructures. Our structures, which consist of a heterostructure region sandwiched between *p*-type GaN, will need a tunnel junction layer below it to facilitate current spreading to ensure that the current flow through the alloy region. Otherwise, the current might flow up the sidewall and not through the heterostructure.

In this work, we investigate the impact of doping levels and a range of surface treatment of the TJ interface as well as unintentional impurities at the TJ interface grown by NH_3-MBE on its current density-voltage (*J-V*) characteristics. Three series of experiments were performed; (i) doping series, (ii) *ex-situ* treatment series and (iii) *in-situ* treatment series. The results from the doping series indicate a reduction in the drop voltage with increase in doping levels of either *n*- or

p- side of the junction. For extremely high doping levels ([Si] = 7.0×10^{20} cm^{-3}, [Mg] = 5.3×10^{20} cm^{-3}), the drop voltage on the junction increases due to self-compensation and increased surface roughness (> 8 nm RMS). In addition, the exposure of the junction to ambient and *ex-situ*/*in-situ* treatments strongly affect the TJ characteristics. For instance, the TJs with HF treatment at the junction shows significantly reduced drop voltages compared to reference continuously grown TJs in the forward direction. To further understand the observed results, the *J-V* results of the TJs with different treatments are correlated with the impurity profiles at the junction and compared with the results from calculations based on polarization and Wentzel-Kramers-Brillouin (WKB) approximations. The findings are beneficial in the development of low voltage TJs to improve the performance of III-nitride based optoelectronic and power electronic devices.

II. Experimental Procedure

All the TJ samples were grown by a Veeco Gen 930 NH_3- MBE system on 1 cm^2 MOCVD-grown GaN/Sapphire templates from Lumilog Saint-Gobain. High-purity elemental Ga was supplied by dual filament effusion cells whilst elemental nitrogen was provided in the form of NH_3 via a showerhead injector. The growths were performed at a reactor pressure of 1×10^{-5} Torr under an NH_3 flow rate of 200 sccm. To process the TJs, first, a ~ 200 nm-thick *n*+ GaN contact layer ([Si]: 5×10^{19} cm^{-3}) was grown sandwiched between two layers of 150 nm *n*-GaN ([Si]: 5×10^{18} cm^{-3}) at a substrate temperature of ~ 820 ºC. Then, the *n*-to-*p* TJ structures, consisting of highly doped *p*++-*n*++ junction (10 nm/10 nm) of various doping levels were grown. The TJ structure was then followed by a 50 nm-thick *p*-GaN growth ([Mg]: 5×10^{19} cm^{-3}) at a substrate temperature of 750 ºC. All the samples were then capped with a 50 nm *p*-GaN ([Mg]: 5×10^{19} cm^{-3}) and a 10 nm-thick *p*++ ([Mg]: 3×10^{20} cm^{-3}) contact layer. The thicknesses and doping levels for each of the layers were calibrated on separate calibration structures using high-resolution X-ray diffraction (HRXRD) and secondary-ions mass spectroscopy (SIMS), respectively. The surface morphology of some of the TJs (particularly for the doping series) were evaluated using atomic force microscopy (AFM) on separate TJ samples.

All the samples were then processed using a standard mesa-isolated device structure design with circular patterns. First, a blanket SiO_2 layer (~300 nm) was deposited using a plasma-enhanced chemical vapor deposition (PECVD). Then, the mesas were defined using a self-aligned wet etching of the SiO_2 using BHF followed by 400 nm of dry etching by a reactive-ion etcher (RIE). Another SiO_2 layer was deposited after the mesa formation to passivate the sidewalls to mitigate leakage issues due to sidewall damage by RIE[15,16]. Pd/Au (30 nm/300 nm) and Ti/Au (30 nm/300 nm) metal stacks were then deposited by electron-beam (E-Beam) deposition to serve as

p- and *n*-contacts, respectively. Figure 1 schematically shows all the TJ structures (the three series) grown and processed in this study.

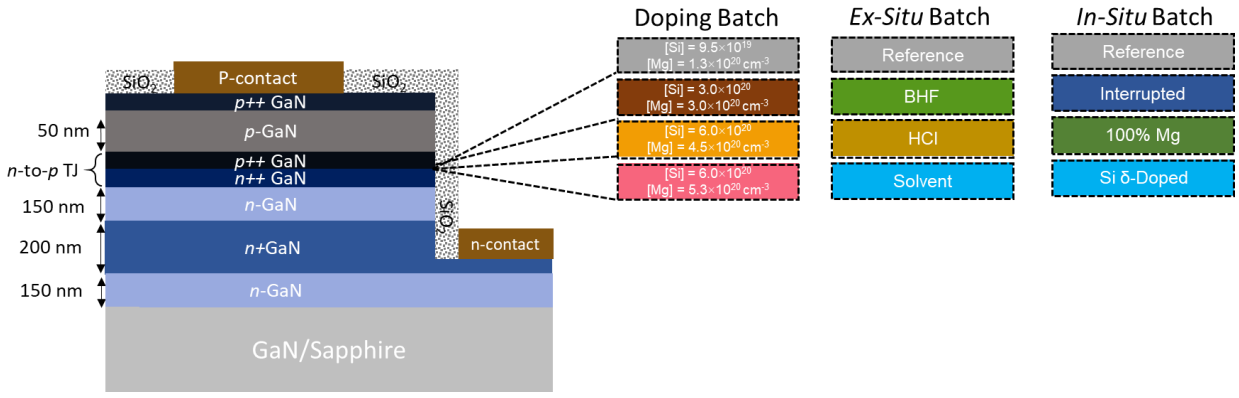

Figure 1. Cross-sectional schematics of the processed *n*-to-*p* TJ structures, including the doping series, *ex-situ* and *in-situ* treatment series. The treatments are performed right at the *n*++/*p*++ junction.

Devices with 7 different circular contact diameters ranging from 50 to 200 μm were processed. The devices were then probed and tested using an electrical probe station. Electrical measurements were conducted using a probe station with tungsten probes connected to a Keithley 4200A-SCS Parameter Analyzer. A fully vertical hole transport is expected in such structures, since the vertical distance in the *p*-region (~ 100 nm) is much smaller than lateral dimension (~ 10 μm) from the edge of the contact to the edge of the mesa. Hence, *J* is calculated by dividing the injected current to the area under the Pd/Au *p*-contact.

III. Results and Discussions

Figure 2 indicates a size-dependency of the *J-V* characteristics of a representative continuously grown TJ sample ([Si] = 9.5×10^{19} cm^{-3}, [Mg] = 1.3×10^{20} cm^{-3}) for circular devices with different diameters from 50 to 200 µm. Except for the end points, which are different due to the limited current compliance being the same independent of the device size (0.1 A), no marked difference is observed between the *J-V* characteristics of different device sizes. The lack of size-dependency in the devices indicates the main contribution from the bulk current and negligible contribution from any sidewall current, which is potentially due to the large separation between the edge of the metal to the edge of the mesa (10 µm) with respect to vertical distance (mesa depth, being ~ 500 nm) in the TJ structures. The sidewall passivation by SiO_2 may also be partially responsible for the lack sidewall current. Also, separate TLM investigations were performed, which showed that the first dielectric protection layer deposition significantly improves the contact resistance and resulted in more ohmic *I-V* characteristics for the *p*-TLMs (not shown).

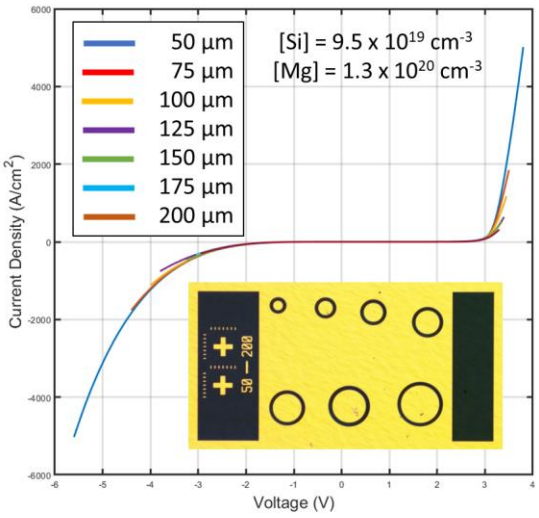

Figure 2. *J-V* characteristics of a selected TJ sample ([Si] = 9.5×10^{19} cm^{-3}, [Mg] = 1.3×10^{20} cm^{-3}) for different devices sizes. Inset shows an optical microscope image of the circular devices with different diameters (from 50 to 200 µm).

Figure 3 compares surface morphologies of the continuously grown TJs with different *n*- and *p*-side doping levels measured by AFM for 5 × 5 µm (Figures 3 (a-d)) and 20 × 20 µm (Figures 3 (e,h)) scans. A relatively smooth morphology with 1.43 nm RMS roughness for a 5 × 5 µm was observed for a TJ sample with [Si] = 9.5×10^{19} cm^{-3}, [Mg] = 1.3×10^{20} cm^{-3}. Increasing the doping levels results in increase in the surface RMS roughness values from 1.43 nm (for [Si] = 9.5×10^{19} cm^{-3}, [Mg] = 1.3×10^{20} cm^{-3}) to 8.15 nm (for [Si] = 7.0×10^{20} cm^{-3}, [Mg] = 5.3×10^{20} cm^{-3}) for 5 × 5 µm scans. Hence, there is a compromise between the doping levels and the RMS roughness. The optimal doping levels seems to be [Si] = 6.0×10^{20} cm^{-3}, [Mg] = 5.3×10^{20} cm^{-3} with a RMS roughness of 2.6 nm.

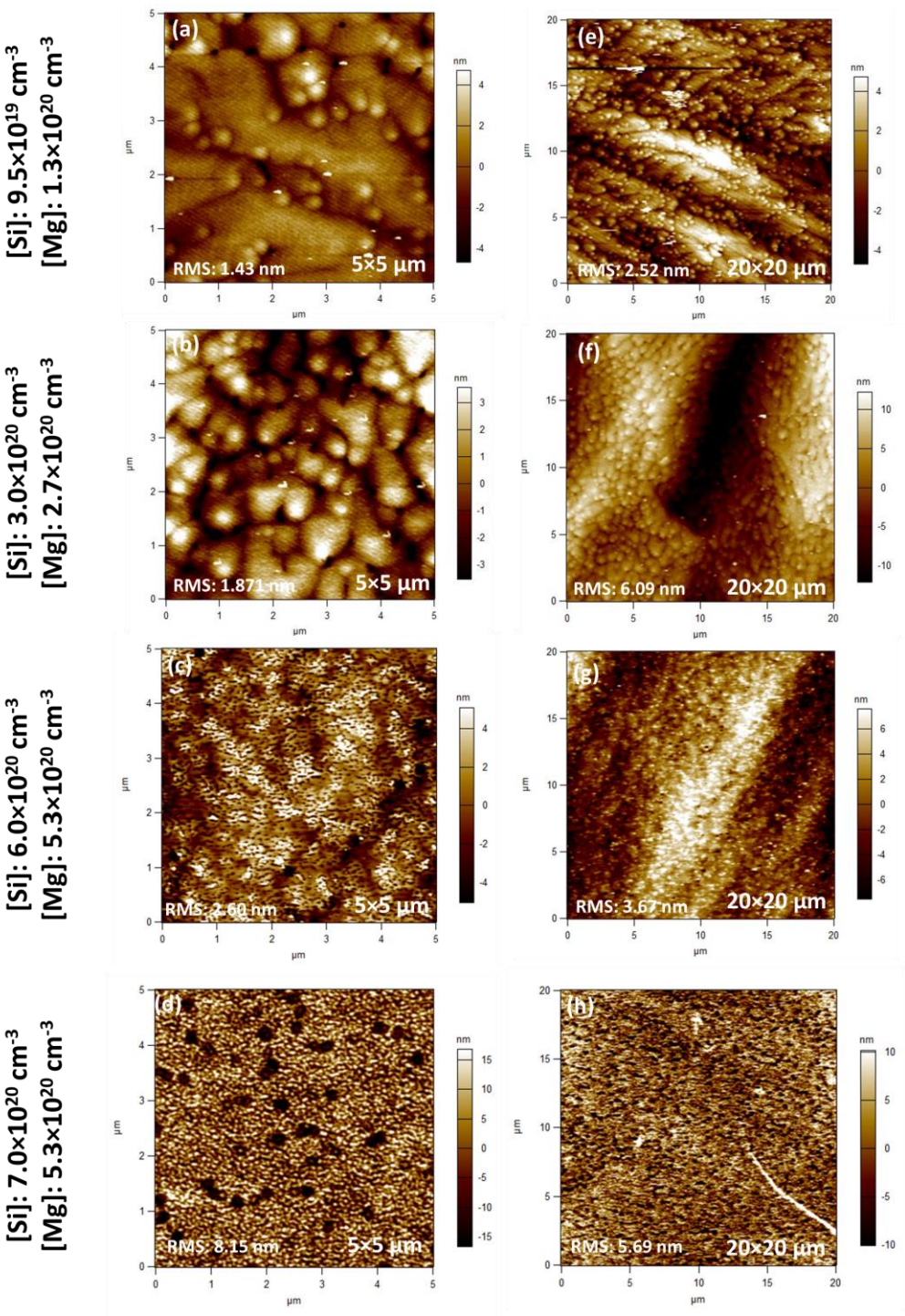

Figure 3. AFM surface morphology analysis of TJs with different doping levels in *n*-and *p*-sides. (a-d) 5 × 5 um, and (e-h) 20 × 20 um scans for (a,e) [Si] = 9.5 × 10^{19} cm^{-3}, [Mg] = 1.3 × 10^{20} cm^{-3}, (b,f) [Si] = 3.0 × 10^{20} cm^{-3}, [Mg] = 2.7 × 10^{20} cm^{-3}, (c,g) [Si] = 6.0 × 10^{20} cm^{-3}, [Mg] = 5.3 × 10^{20} cm^{-3}, and (d,h) [Si] = 7.0 × 10^{20} cm^{-3}, [Mg] = 5.3 × 10^{20} cm^{-3}. The RMS roughness values for each scan is indicated at the bottom of the scan.

Table I summarizes the description of the TJ samples used in this investigation, consisting of three main series; a doping series, an *ex-situ* treatment series, and an *in-situ* treatment series. The doping series compares the TJs with different *n*- and *p*-doping levels, while the other two series compares the effects of different treatments at the TJ interface for a fixed doping level. The samples for the doping series were grown based on AFM analysis results that was separate from those reported in Figure 3. For the continuous TJs, the growth was performed without any interruption. For the *ex-situ* treated TJs, the samples were taken out of the reactor, treated in a cleanroom environment, vacuum sealed, transferred back and loaded into the chamber for regrowth. For the interrupted sample, after the *n*-side of the TJ was grown the sample was kept in the chamber for 10 min during the interruption followed by a temperature ramp up and growth of the *p*-side.

Figure 4 schematically compares the conduction and valence band diagrams for a GaN TJ in forward (Figure 4(a)) and reverse (Figure 4(b)) biases. As will be discuss later, the schematics of Figure 4 indicates that, the tunneling mechanisms is different in the forward (Figure 4(a)) and in the reverse (Figure 4(b)) bias conditions. The former is dependent on the Mg impurity band and defect-assisted tunneling, while for the latter, the main tunneling is inter-band tunneling which is only dependent on the band bending. Figure 5 compares the *J-V* characteristics of the continuously grown TJs with different $n++/p++$ doping levels (doping series). According to the plots of Figure 5, a clear increase in the forward *J* by increasing the $n++/p++$ doping levels. In the reverse direction, the trend is less clear; the voltage drop reduces from 2.25 V to 0.75 V when the doping levels increase from ~ 1×10^{20} cm^{-3} to 3×10^{20} cm^{-3}, while the voltage drop reduction is less pronounced for larger doping levels (~ 5-6×10^{20} cm^{-3}). For very large doping levels (> 7×10^{20} cm^{-3}) a jump in the forward voltage was observed, potentially due to the roughness and/or self-

compensation. The asymmetric nature of this phenomenon is due to the difference in transport mechanism between the two biases (Figure 4). As mentioned, in reverse bias, the dominant mechanism for current flow is the inter-band tunneling, which directly depends on the band-bending (potential tunneling barrier height), which increases with increasing the doping concentrations. However, the reverse *J* remains within the same proximity for higher doping levels (above 3×10^{20} cm^{-3}, as indicated in Figure 5), potentially due to the increased surface roughness (Figure 3) and possibly higher defect densities. On the other hand, the dominant tunneling mechanism in the forward bias could be through evanescent impurity states within the energy gap in the *p*-side of the junction (Figure 4(a)). As the *p*-type doping level increases, the Mg impurity band becomes more dominant, resulting in higher defect-assisted tunneling and larger forward *J*. A negative differential resistance (NDR) in the forward bias were observed, which is more pronounced in some samples (as indicated in the Figure 5 at ~ 1.5 V). Normally, an NDR occurs as the inter-band tunneling reduces by increasing bias, below the onset of diffusion in the forward bias. However, here the NDR was not as pronounced as expected for a TJ, possibly due to the significant effect from defect-assisted tunneling through the Mg impurity band.

Regrown TJs with different *ex-situ* (such as buffered HF or BHF, HCl, and solvent) and *in-situ* (Si delta doping, in-chamber growth interrupt, and full Mg exposure) treatments at the junction interface were also compared. Figure 6 and 7, respectively show the comparison of the J-V characteristics for the e*x-situ* and *in-situ* treatment series. The results of the *ex-situ* treatment series (Figure 6) indicate that a BHF treatment results in a marked drop in the forward voltage (from 1.34 V to 0.92 V at 100 A/cm^2). In fact, some earlier studies have also shown similar effects from HF on the performance of *p*-to-*n* TJs[17]. HCl and solvent treatments, on the other hand, increased the forward voltage (from 1.34 V to ~ 2 V at 100 A/cm^2). Nevertheless, the reverse *J-V*

characteristics are nearly independent of the choice of the *ex-situ* treatment (between 1.8 V to 2.2. V at -100 A/cm^2), indicating different current mechanisms in the forward and reverse directions. The voltage drop in the BHF-treated TJ structure are among the best reported so far for any GaN-based TJs. For the *in-situ* treatment series (Figure 7), the growth interrupt sample showed a larger forward voltage (but similar reverse voltage) compared to reference (from 1.25 V to ~ 2 V at 100 A/cm^2), potentially due to intrinsic defects being generated at the junction during cool down and/or ramp up in the interrupted sample. Both the Si delta doped and the full Mg exposure samples show larger forward voltage but smaller reverse voltage compared to the continuously grown reference junction.

To see whether the effects of treatments on the TJ drop voltage is attributed to the impurities at the junction interface, an impurity profiling is needed. Normally, large Si, O, and C spikes are expected for regrowth structures[18,19]. The presence of large Si spike after sample exposure to ambient (even after different wet treatments such as HF, HCl, *etc.*), has been a major challenge for development of various vertical power electronic architectures[19,20]. For TJs, however, Si spike may result in change in the Fermi level position at or near the junction and enhance the tunneling probability. Hence, the drop voltage reduction may not directly correlate with the impurity spikes. A more systematic correlation of the impurity profiles from SIMS and the TJ electrical characteristics and comparison with the predicted results based on polarization and WKB approximation is also performed. This, in addition, allow for a better understanding the inter-band tunneling mechanisms in GaN-based TJs.

Series	**TJ Sample**	**Continuous/Regrown**	**[Si] (× 10^{20} cm^{-3})**	**[Mg] (× 10^{20} cm^{-3})**	**TJ Treatment**
Doping Series	A	Continuous	0.95	1.3	N/A

	B	Continuous	3.0	3.0	N/A
	C	Continuous	6.0	4.5	N/A
	D	Continuous	6.0	5.3	N/A
ex-situ Series	E	Continuous	6.0	5.3	N/A
	F	Regrown	6.0	5.3	BHF
	G	Regrown	6.0	5.3	HCl
	H	Regrown	6.0	5.3	Solvent
in-situ Series	I	Continuous	6.0	5.3	N/A
	J	Regrown	6.0	5.3	*In-situ* Interrupt
	K	Regrown	6.0	5.3	100% Mg
	L	Regrown	6.0	5.3	Si δ-doping

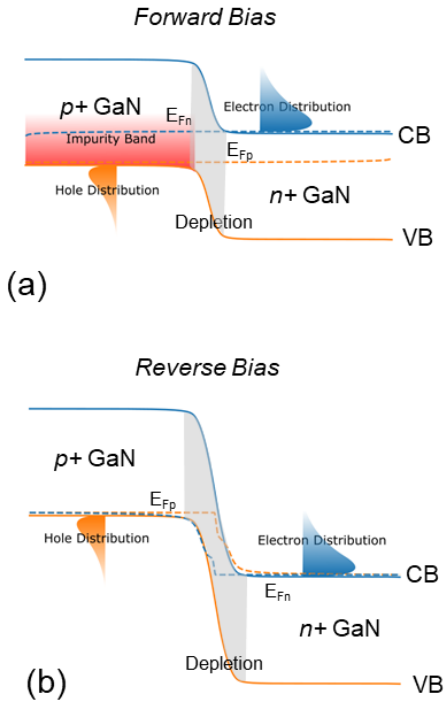

Figure 4. Schematic conduction band (CB) and valence band (VB) diagrams of a GaN TJ in (a) forward and (b) reverse bias. Forward bias case in (a) captures the band diagram below the onset of diffusion and indicates the Mg impurity band.

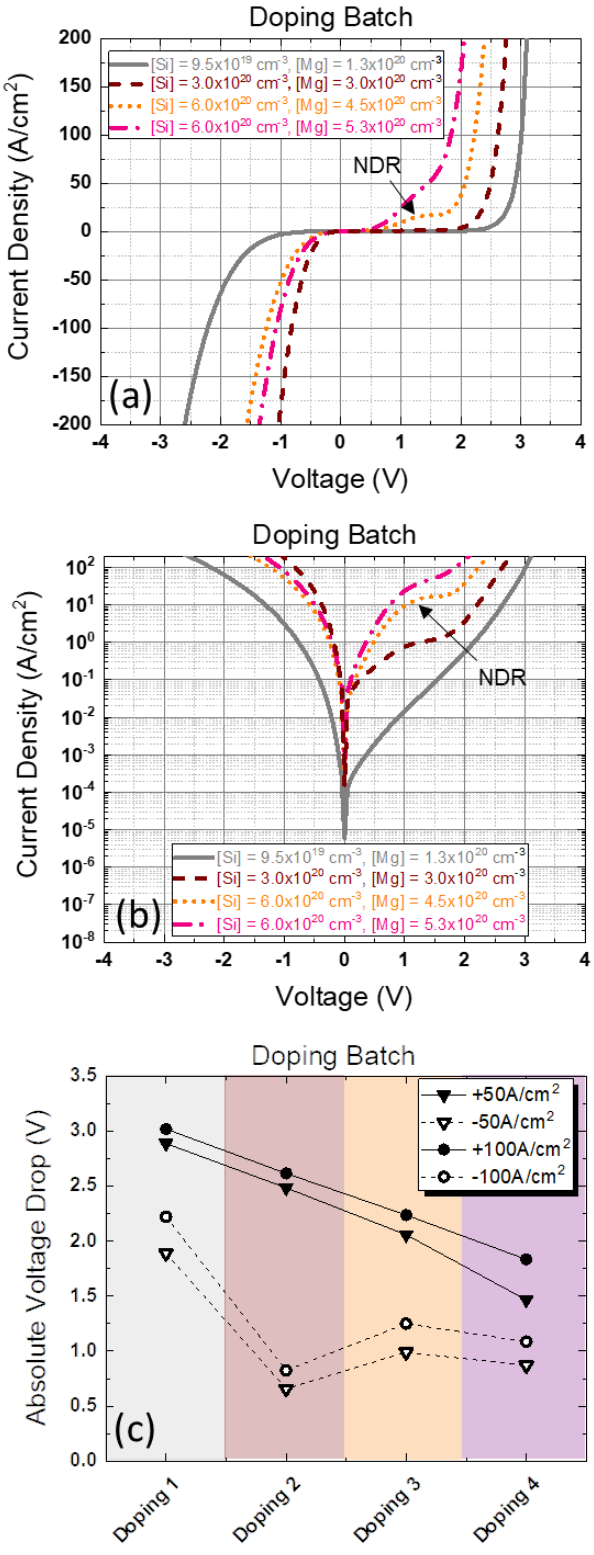

Figure 5. Comparison of J-V characteristics of continuously grown TJs in the doping series in (a) linear and (b) semi-log scales for doping 1 (n = 9.5×10^{19}, p = 1.3×10^{20}cm^{-3}), doping 2 ([Si] = 3.0×10^{20}, [Mg] = 3.0×10^{20} cm^{-3}), doping 3 ([Si] = 6.0×10^{20}, [Mg] = 4.5×10^{20} cm^{-3}), and doping 4 ([Si] = 6.0×10^{20}, [Mg] = 5.3×10^{20} cm^{-3}). (c) Comparison of voltage drops at ±50 and ±100 A/cm^2 for doping1-4 structures.

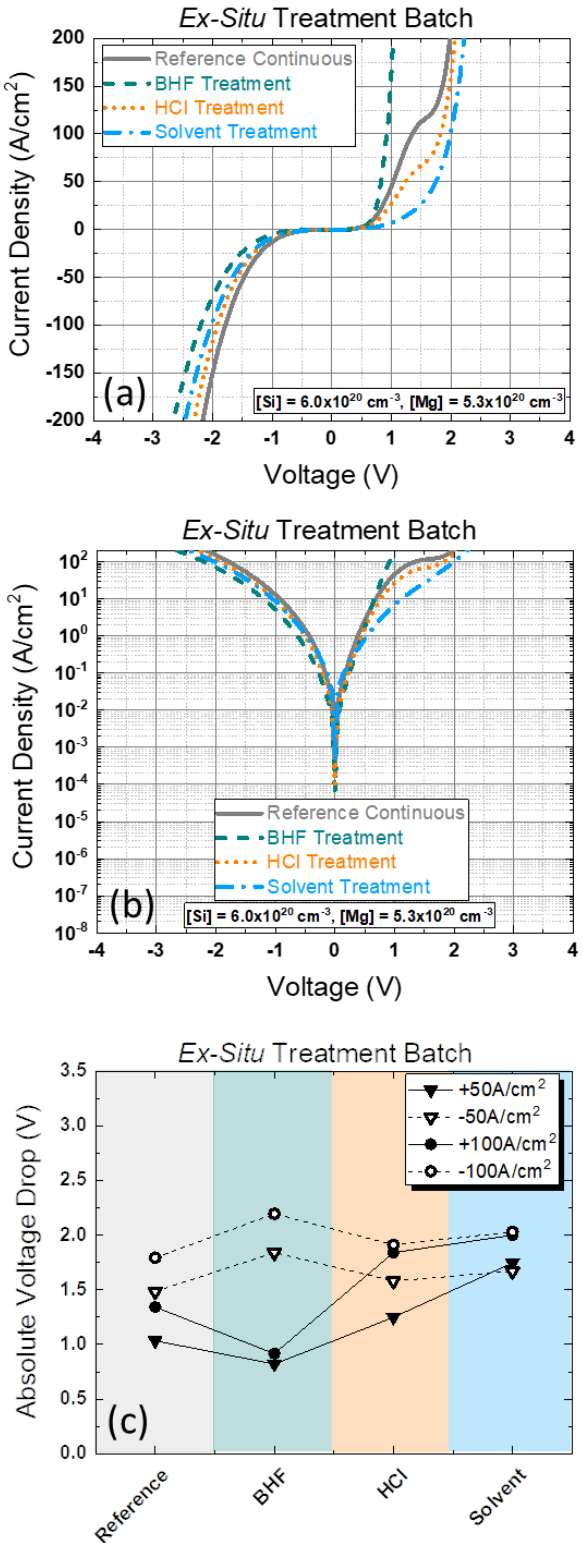

Figure 6. Comparison of J-V characteristics of TJs in the ex-situ treatment series in (a) linear and (b) semi-log scales. All the structures have doping levels of [Si] = 6.0×10^{20}, and [Mg] = 5.3×10^{20} cm^{-3}. (c) Comparison of voltage drops at ±50 and ±100 A/cm^2 for all the samples in this series.

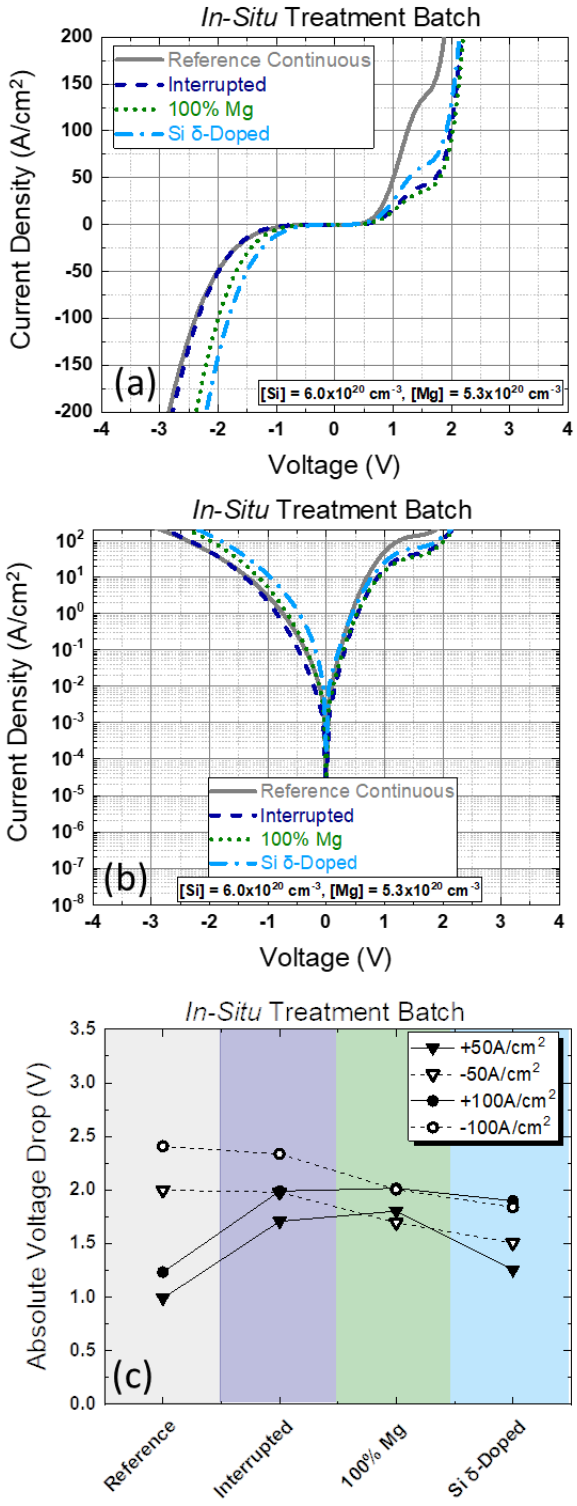

Figure 7. Comparison of J-V characteristics of TJs in the ex-situ treatment series in (a) linear and (b) semi-log scales. All the structures have doping levels of [Si] = 6.0×10^{20}, and [Mg] = 5.3×10^{20} cm^{-3}. (c) Comparison of voltage drops at ±50 and ±100 A/cm^2 for all the samples in this series.

IV. Conclusion

In summary, a set of different *n*-to-*p* GaN TJs were investigated. The results of doping series suggest that high doping levels up to a certain level in both *n*- and the *p*-side of the junction, enhances the current from *J-V* analysis. For the doping levels above a certain threshold (at [Si] = 7.0×10^{20} cm^{-3}, [Mg] = 5.3×10^{20} cm^{-3}), the drop voltage results are compromised, possibly due to the roughness and/or self-compensation effects. In addition, our results indicate a strong impact of ambient exposure as well as *in-situ*, *ex-situ* surface treatments at the junction of the TJs on its forward and reverse *J-V* characteristics. For instance, BHF treatment results in a drastic drop in the forward voltage (from 1.34 V to 0.92 V at 100 A/cm^2). A correlation of the *J-V* results with the impurity profiles from SIMS evaluations compared with the predicted results based on polarization and WKB approximation shed light on the origin of the observed behaviors. The results are beneficial in the development of TJs to improve the performance of III-nitride based optoelectronic and power electronic devices.

V. Acknowledgements

This work was supported by CREST, the Simons Foundation (Grant No. 601952, JS), Air Force Office of Scientific Research (Program No. FA9550-19-1-10090), and the National Science Foundation (NSF) RAISE program (Grant No. A007231601). A portion of this work was performed at the UCSB nanofabrication facility.

VI. References

Automatic citation updates are disabled. To see the bibliography, click Refresh in the Zotero tab.